UNIVERSITY OF SOUTHAMPTON

FACULTY OF ENGINEERING, SCIENCE AND MATHEMATICS

School of Engineering Sciences

Study Into the Use of the Global Navigation Satellite System for Maritime Structure Analysis

by

Joseph François Maurice Bélanger, B.A.Sc.

Ph.D. thesis in partial fulfilment of the requirements
for the degree of Doctor of Philosophy

13th January 2009

To Mom and Luc, and in loving
memory of Dad and Vincent

UNIVERSITY OF SOUTHAMPTON

ABSTRACT

FACULTY OF ENGINEERING, SCIENCE AND MATHEMATICS
SCHOOL OF ENGINEERING SCIENCES

Doctor of Philosophy

STUDEY INTO THE USE OF THE GLOBAL NAVIGATION SATELLITE SYSTEM FOR MARITIME STRUCTURE ANALYSIS

Joseph François Maurice Bélanger, B.A.Sc.

Certain civilian uses of the Global Positioning System (GPS) now demand levels of precision exceeding the original military specifications for the system. For example, at present, GPS is used in surveying, navigation and monitoring applications. Although GPS has been used previously to monitor the structural integrity of civilian structures such as bridges and towers, the experimental conditions have one significant difference: These structures are all immobile allowing for fixed references to be used.

This research's ultimate aim was to conduct a feasibility study into the use of GPS, and of the soon to be deployed Galileo constellation, in structural monitoring of maritime vessels. Under these conditions, a fixed base station as was used in previous structural monitoring is not a valid approach. New techniques, or variations on the current ones, were examined to deal with this lack of a fixed reference.

This thesis considers the simulator that was developped in the early phases of the project and the results that were generated. An expanded version of the simulator is then explained, alongside the processes used to model structural deformation experienced by a ship at sea. Frequency analysis of the simulator results is also performed and the results detailed. It is found that frequency-domain analysis allows for the identification of different movements seen on the structure. In addition, an analysis of the impact the deployment of the Galileo constellation is conducted using simulation. This simulation found a drop of about 20% in Dilution of Precision (DOP) over several areas.

This thesis then examines some of the field work, that aimed to measure rigid-body motion, that was conducted onboard *Red Jet 4*, a catamaran-type vessel. The experimental setup is described, and the results are briefly considered.

A method for determining the optimal configuration of the receiver network is also proposed alongside an algorithm to detect plastic deformation of a vessel structure. Finally, this report considers the original project objectives and how these were or were not met. Should sufficient accuracy be achieved by a GPS receiver network, it is possible to use the system to monitor ship structures.

Table of Contents

Table of Figures

Table of Tables

Declaration of Authorship

I, Joseph François Maurice Bélanger, declare that this thesis entitled:

Study Into the Use of the Global Navigation Satellite System for Maritime Structure Analysis

and the work presented within it are my own. I confirm that:

- This work was done wholly or mainly while in candidature for a research degree at this University;
- Where any part of this thesis has previously been submitted for a degree or any other qualification at this University or any other institution, this has been clearly stated;
- Where I have consulted the published work of others, this is always clearly attributed;
- Where I have quoted from the work of others, the source is always given. With the exception of such quotations, this thesis is entirely my own work;
- I have acknowledged all main sources of help;
- Where the thesis is based on work done by myself jointly with others, I have made clear exactly what was done by others and what I have contributed myself;
- None of this work has been published before submission.

Southampton, 13th January 2009

Acknowledgements

I'd like to thank all those who have helped me over the past four years as I struggled to get through this project, all the more so after my return to the UK in April 08. The past four years have been a long, winding road and I have finally reached the end of it.

First and foremost, many thanks to my supervisor, Dr. Adrian Tatnall, for all his advice over the past few years. All of it has been appreciated, and I now (reluctantly and with a grin on my face) admit that I was far too ambitious at first.

To family and friends back in Canada, thanks for all the moral support and laughs along the way. I needed it on some days... Glad you were around then. Special thanks to my family in Canada, my old U of O classmates and lecturers, and my old schoolmates. There are too many to name here, but you know who you are. And thanks Paul for the help with the early versions of the serial IO code.

To all my labmates, past and present, thanks for the laughs and/or suggestions along the way. It has been an honour to work with all of you. Special thanks to Frank who introduced me to LaTeX before I got too far ahead writing this document in Word. You saved me a *LOT* of trouble.

To Steve Gillett and all the staff at Red Funnel for putting up with my (sometimes) disruptive equipment. I wouldn't have been able to finish up the project without a place to put the theory to the test. I learned much from your crews, and have picked up a number of very good stories along the way. And yes, I've been repeating many of them.

To my all my flatmates and housemates, many thanks for all the help and laughs over the past few years. Special thanks to Nery, Adi, Naji and Ilja who were my flatmates back in my first year. I really owe you four one! I likely would have ended up suffering in a little corner of a hospital in March 2005 had it not been for you taking good care of me.

To everyone else I have yet to mention, and by that I mean, the fencing squads, ice hockey enthusiasts and friends, both new and old, many thanks for everything.

And finally many thanks to all those who reviewed the final draft of this document.

List of Abbreviations and Definitions

ACS	Attitude Control Systems
AIS	Automatic Identification System
CDMA	Code Division Multiple Access
CPGPS	Carrier-Phase Global Positioning System
CS	Commercial Service
DCPGPS	Differential Carrier-Phase Global Positioning System
DFT	Discrete Fourier Transform
DGPS	Differential Global Positioning System
DOD	United States of America Department of Defense
DOP	Dilution of Precision
ECEF	Earth Centered Earth Fixed
EGNOS	European Geostationary Navigation Overlay System
EIRP	Equivalent Isotropically Radiated Power
ESA	European Space Agency
FAA	United States Federal Aviation Administration
FE	Finite Element
FFT	Fast Fourier Transform
FIR	Finite Impulse Response
GDOP	Geometric Dilution of Precision
GIOVE	Galileo In-Orbit Validation Element
GLONASS	Global Navigation Satellite System
GNSS	Global Navigation Satellite System
GPS	Global Positioning System
GRACE	Gravity Recovery and Climate Experiment
HDOP	Horizontal Dilution of Precision
HNoMS	His Norwegian Majesty's Ship
HTL	Hardware-in-the-Loop
IP	Immersion Protocol
ITWF	International Transport Workers' Federation

ISS	International Space Station
JPALS	Joint Precision Approach and Landing System
LEO	Low Earth Orbit
LORAN	Long Range Navigation
LOS	Line Of Sight
OBO	Oil-Bulk-Ore Combination Carrier
OS	Open Service
MCA	Maritime and Coastguard Agency
MEO	Medium Earth Orbit
MV	Motor Vessel
NAVSTAR	Navigation System with Timing And Ranging
NNSS	Navy Navigation Satellite System
NTSB	National Transport and Safety Board
PDOP	Position Dilution of Precision
PRS	Public Regulated Service
PR	Pseudo-Random
QPSK	Quadrature Phase-Shift Keying
RFI	Radio-Frequency Interference
RSA	Russian Space Agency
RTCM	Radio Technical Commission for Maritime Services
SA	Selective Availability
SAR	Search and Rescue
SOL	Safety of Life
SNS	Satellite Navigation System
SS	Steamship
TCAS	Traffic Alert and Collision-Avoidance System
TEC	Total Electron Content
TECU	TEC Unit
TDOP	Time Dilution of Precision
UK	United Kingdom
USA	United States of America
USAF	United States Air Force
USB	Universal Serial Bus
USCG	United States Coast Guard
USN	United States Navy
USS	United States Ship
USSR	Union of Soviet Socialist Republics

VDOP	Vertical Dilution of Precision
VLF	Very Low Frequency
VHF	Very High Frequency
WAAS	Wide Area Augmentation System
WWII	World War II

μ	Earth's Gravitational Constant	$\mu = 3.986\ 005 \times 10^{14}$	$[m^3/s^2]$
$\dot{\omega}_e$	Earth's Angular Velocity	$\dot{\omega}_e = 7.292\ 115\ 146\ 7 \times 10^{-5}$	$[rads/s]$
c_0	Speed of Light in Vacuum	$c_0 = 2.997\ 924\ 58 \times 10^8$	$[m/s]$

a_x	Coefficients used to model ${}^j\delta(t)$	unitless
a_i	Amplitude of mode i in pipe model	$[m]$
c	Speed of Light	$[m/s]$
C_b	Same as $\Delta_i^j\delta(t)$	$[s]$
${}_i^jd(t)$	Distance between receiver i and satellite j	$[m]$
E	Modulus of elasticity	$[Pa]$
f	Frequency	$[Hz]$
f_i	Mode natural frequency	$[Hz]$
f_w	Wide-lane frequency	$[Hz]$
F	Loading force on a beam	$[N]$
I	Moment of intertia	$[kgm^2]$
I_{xx}	Second moment of area	$[m^4]$
${}^jf$	Transmission frequency for satellite j	$[Hz]$
${}_i^jN$	Integer ambiguity between receiver i and satelite j	unitless
ℓ	Point along length L of the pipe model	$[m]$
L	Length of the ship in the pipe model	$[m]$
m	Mass of the ship in the pipe model	$[kg]$
M	Bending moment	$[Nm]$
N_w	Wide-lane integer ambiguity	unitless
$R_x(t_1, t_2)$	Autocorrelation function for $x(t)$	unitless
$R_{xy}(k)$	Crosscorrelation functions for $x(t)$ and $y(t)$	unitless
t_0	Reference time	$[s]$
(x_u, y_u, z_u)	User's position	$[m]$
$({}^jx, {}^j y, {}^j z)$	Satellite j's position	$[m]$
y	Beam deflection	$[m]$
α_i	Weighting coefficient for mode i	unitless
β	TEC value for ionospheric modelling	$[TECU]$

β_i	Normalised signal strenth for mode i at point ℓ	unitless
$\Delta_i^j\delta(t)$	Residual timing bias	$[s]$
${}_i\delta(t)$	Timing bias caused by reciever i's clock at time t	$[s]$
${}^j\delta(t)$	Timing bias caused by satellite j's clock at time t	$[s]$
λ	Wavelength	$[m]$
λ_i	Mode boundary constant	unitless
$\xi(\ell)$	Total deflection at point ℓ	$[m]$
$\xi_i(\ell)$	Mode deflection at point ℓ	$[m]$
${}_i^j\varrho\,(t)$	Carrier-phase observable from satellite j at receiver i	unitless
σ	Stress at a point in a beam	$[Pa]$
σ_i	Mode constant	unitless
$\psi(\ell)$	Value of optimisation function at point ℓ	unitless

Chapter 1

Introduction

The Captain wired in he had water coming in
And the good ship and crew was in peril
And later that night when his lights went out of sight
Came the wreck of the Edmund Fitzgerald.
-Gordon Lightfoot, *The Wreck of the Edmund Fitzgerald*

High-precision Global Positioning System (GPS) based devices have been used in the past to determine movement of the Earth, and of structures, such as bridges and dams, over long periods of time. It is the premise of this project that the same type of technology could be applied to structures under heavy dynamic stress, such as vessels.

Furthermore, this technology could also allow for the obtention of various information for a particular vessel (pitch, roll, heave, etc.) using a network of GPS receivers. The information obtained could then be used to analyse in real-time the ship's structure and detect unsustainable levels of stress, or even serious damage to a structure due to stress.

1.1 Motivation for the Project

This project has numerous motivations. The primary one is obviously the prevention of maritime accidents. The idea is to prevent the consequences of such accidents, in terms of human, ecological and economic costs. In this section, two famous shipwrecks are briefly considered. The first of these, the one of the *SS Edmund Fitzgerald*, occurred in 1975 and is the subject of a famous ballad by Canadian artist Gordon Lightfoot. The second shipwreck considered is that of the oil-bulk-ore combination carrier (OBO) *MV Derbyshire* in 1980, one of the more notorious shipwrecks in United Kingdom (UK) history.

1.1.1 The Sinking of the *SS Edmund Fitzgerald*

Sometime between 1900 and 1930 local time on 10 November 1975, the *SS Edmund Fitzgerald*, loaded with 26,000 tons of ore and crewed by 29 men, sank in the Canadian section of Lake Superior after the strongest storm seen in that area in many years. All hands onboard were lost.

As would still be the case today, an investigation into the disaster was conducted by the National Transport and Safety Board (NTSB), the United States of America's (USA) governmental body responsible for investigating accidents involving transportation as the *SS Edmund Fitzgerald* was registred in the USA. Their report concluded that the cause of the disaster was failure of the cargo hold hatches. This event then allowed the cargo hold to flood, and led to structural failure of the vessel. [56]

This report was controversial as it was not adopted unanimously. In fact, Philip A. Hogue, one of the investigating commission's members, filed a strong dissenting statement in which he listed eight points of contention regarding the report which was adopted by the majority of the commission. One of his main points of contention was that at approximately 1530, or four hours prior to the disaster, the master of the *SS Edmund Fitzgerald*, Captain Ernest McSorley, had radioed that his ship had suffered severe structural damage. This statement is included along side the report available on the official websited of the United States Coast Guard (USCG). [56]

Controversy remains to this day as to the real cause of this disaster. However, as the wreck was found, split in half, at the bottom of Lake Superior, five hundred feet below the surface, it is clear that some form of structural failure did occur. Whether the split occurred on the surface, as a result of the ship striking the bottom of Lake Superior, or while it was sinking is still in contention. This thesis will not attempt to solve this particular question. However, it is a valid question to ask if this disaster could have been prevented by the use of a structural monitoring system.

1.1.2 The Sinking of the *MV Derbyshire*

On 9 September 1980, the OBO *MV Derbyshire*, weighing in at over 90,000 gross tons sank in heavy seas in the Sea of Japan during Typhoon Orchid. No distress call was ever received from the ship, leading to the conclusion that it sank extremely rapidly. To this day, the *MV Derbyshire* remains the largest ship lost at sea by a UK-based corporation. It is also one of the most contentious maritime accidents of the XXth century, and was still headline news twenty years after the incident.

Forty-four people lost their lives in this disaster, forty-two crewmen and two of their wives.

An initial inquiry at the time of the disaster came to a similar conclusion as the NTSB had reached following the wreck of the *SS Edmund Fitzgerald*. This inquiry believed that a main cargo hold hatch had been improperly secured. This resulted in the ship slowly flooding in rough seas, losing buoyancy and eventually sinking as a result. The initial inquiry's report was rejected outright by families of the victims, stating that without analysis of the wreck it was impossible to draw this conclusion. These families campaigned for several years, drawing attention to maritime safety and the case of the *MV Derbyshire*, a campaign for which they were eventually recognised with the Marine Society's Thomas Gray Medal in July 2004.

Finally, in 1994, following persistant refusal from official government bodies to launch a search for the wreck of the *MV Derbyshire*, the International Transport Workers' Federation (ITWF) launched its own investigation. The wreck was located by the ITWF team after eight days of searching in the Sea of Japan, lying more than two miles below the surface. Some of the data from the search efforts was published in 1998, prompting the UK government to order a formal inquiry into the disaster.

This enquiry was led by Mr. Justice Colman, and called upon a number of scientific witnesses to analyse the data recovered from dives to the wreck. A number of articles resulted from this work, but they all have one common trait: They exonorate the crew from any blame for the disaster. [23, 24] In fact, these articles blame structural failure based on either structural weakness or a structural defect. The report from Justice Colman, delivered in November 2000, followed these lines and lay the blame squarely on twelve ventillation ducts which failed and then allowed the ship to flood. The reports continues on to list that due to the partial flooding of the ship, it experienced greater than maximal tolerance hull stresses, which caused the hull to fail and the ship to sink almost instantly. There is also corroborating evidence based on failures found onboard the *MV Derbyshire*'s sister ships that there may have been a design flaw.

Based on Justice Colman's report, the sinking was due to excessive hull stresses. Thus, in this case more so than that of the *SS Edmund Fitzgerald*, it is valid to question whether a hull monitoring system might have prevented this disaster altogether, or, at the very least, possibly saved some of the forty-four lives that were tragically lost.

1.2 Objectives of Research

This project aimed to determine if high-precision GPS systems could be used to obtain structural information about a ship. The original objectives of the research were as follows:

- Determine the accuracy required from a GPS system for structural analysis of a vessel;
- Develop real-time processing algorithms to analyse dynamic loads applied to a ship using the output of the GPS receivers;
- Determine the optimal number of GPS receivers required and the preferred location for such sensors to detect structural motion;
- Devise means of detecting certain types of stress damages such as plastic deformation;
- Develop signal processing algorithms to extract additional information, such as heading, pitch, roll and heave, using the output of the GPS receivers;
- Attempt to implement a monitoring system on a small scale;
- Consider the impact of the upcoming Galileo constellation on these specific applications.

The primary method of investigation was theoretical simulation. When positive simulation results were obtained, the research took a practical turn. In any event, many of the original objectives were met, and some, due to a lack of time for this project, had to be relegated to future work status. Over the course of this document, each of these objectives will be covered and discussed in detail.

At the start of the project, there was very little academic literature available regarding the use of the GPS onboard vessels, and none of it dealt with structural monitoring. There was, however, some literature on the topic of attitude monitoring using GPS. It was decided that the project could possibly be useful in practice onboard real vessels and that the hole in the literature which could be filled by this work.

At the conclusion of this project, the literature regarding this particular application of the GNSS remains sparse. Two of the publications in the field were prepared to present a portion of the simulator work [9] and later of the practical work [10] conducted onboard *Red Jet 4*. The important aspects of both papers are covered in Chapters 3 and 4 respectively. An important paper was published after the start

of this research by Petovello et al. from the University of Calgary [46]. The importance of this latter paper is discussed in Chapter 2.

1.3 Structure of Thesis

This document is divided into five chapters, including this one. The second chapter explains the functioning of the GPS and the techniques that were used to model ship structures. A review of previous work in the field of monitoring using GPS receiver networks is also done in this chapter.

Chapter three deals with the two simulators developed over the course of this project. The first of these is the ship simulator and the second the constellation simulator which was used to attempt in order to determine the impact of the deployment of the Galileo constellation. Simulation results are also presented and discussed in detail.

Chapter four concerns itself with the practical experimentation that was done onboard *Red Jet 4*, a passenger ferry that operates between Southampton, located on the south coast of the UK mainland, and West Cowes, located on the north side of the Isle of Wight.

Chapters five comprises the analysis of the results and the conclusions drawn from the work respectively. Future work will also be considered in this chapter.

Chapter 2

GPS Operation and Literature Survey

2.1 Introduction

This chapter aims to present most of the background information which is necessary to the comprehension of this thesis. The chapter begins with a presentation, in some detail, of the operational principles behind carrier-phase GPS. The method by which position is determined using the above Satellite Navigation Systems (SNS) is developed. This is followed by a description of some of the augmented SNS available today and concludes by a brief description of some of the additional utilisations of Galileo. This is followed by the results of the literature survey conducted in the early stages of the project. This chapter will conclude with a presentation of some of the previous uses of the GPS in structural monitoring and some of the current uses of GPS onboard vessels.

2.2 Operation of the NAVSTAR GPS

In this section, the principles behind the use of carrier-phase data from the NAVSTAR GPS system, or GPS for short, are detailed. An overview of the GPS space segment is first presented. This is followed by some of the mathematical techniques behind signal acquisition and location of the user's position. This section also covers some of the augmented SNS and explains some of the problems that are associated with the use of carrier-phase data.

2.2.1 The GPS Space-Segment

As of 16 October 2007, the GPS system space-segment consisted of 31 satellites [7] orbiting the Earth in six different orbit planes, each containing four satellites. Each

of the orbit planes is at an inclination of 55 degrees ($i = 55°$) and is separated from neighbouring planes by 60 degrees. The ground track repeats every sidereal day [39], which is the time it takes for the Earth to complete one revolution about its axis.

The first GPS satellites, or "Block I" satellites, were launched in 1978. These have since been replaced by "Block II", "Block IIR" and "Block IIR-M" satellites, with the 'R' standing for replacement. "Block II" satellites use more accurate clocks than their "Block I" counterparts. The first "Block II" satellite was launched in 1989 [26]. It was expected that "Block III" satellites, which should have far greater abilities to provide services than the "Block II" variants, will be launched by the end of the decade, however the contract for their construction has yet to be awarded to either Boeing Corporation or Lockheed Martin who as of October 2007 were the sole competitors for the tender from the United States Air Force (USAF).

The current GPS satellites transmit their signals on the $L1$ and $L2$ frequency bands, 1575.42 MHz and 1227.60 MHz. These frequencies correspond to atomic standards and are very well defined. To obtain these frequencies, the GPS uses the fundamental L band frequency of 10.23 MHz and frequency multiplication [26]. However, in order to take into account general relativistic effects due to the high orbital speed of the satellites, the satellites use a base frequency of $10.23 \times 10^6 - 4.567 \times 10^{-3}$ Hz[57]. Note that the new satellites will also use the $L5$ band centered at 1176.45 MHz[38] in addition to the $L1$ and $L2$ bands.

Different signals are differentiated by the use of Code Division Multiple Access (CDMA), a necessity since each satellite transmits on the same frequency. To accomplish this, each satellite is assigned a unique and periodic pseudo-random code, which is used to encode the information it transmits. Receivers know the pseudo-random code of each individual satellite and will attempt to lock-on to individual satellites using this information. This procedure will be detailed in the latter portion of Section A.4.2.

There are two types of pseudo-random codes. The first is known as the *Coarse Acquisition Code*, or C / A code for short. It is transmitted on the $L1$ band exclusively at a frequency of 1.023 MHz and is 1023 chips long, meaning its periodicity is 1 ms. Civilian receivers generally are limited to using the C / A code. The second type of code is the *Precision Code*, or P code for short. The P code is transmitted on both the $L1$ and $L2$ bands at a frequency of 10.23 MHz and is 2.3547×10^{14} chips long, meaning its periodicity is 266.4 days. It is limited to military users. [26]

Based on this information, the chip length can be calculated as being approximately 293.05 m for the C / A code and 29.31 m for the P code. Note that in this

section, the term chip is used instead of the term bit as the pseudo-random codes are only used to encode information and do not contain any information of their own.

2.2.2 Carrier-Phase GPS

Carrier-Phase GPS (CPGPS) represents the next step in terms of accuracy. CPGPS receivers utilise the phase information from the satellite's carrier wave signal in addition to the code information to determine a user's position.

From elementary physics:

$$c = \lambda f \tag{2.1}$$

where c is the speed of propagation of light, λ the wavelength, and f the frequency of the wave.

Thus, in the $L1$ frequency band, a single wavelength measures approximately 19.0 cm. Assuming that a receiver can determine the phase of the carrier wave to within a few degrees, then a precision of the order of a few millimetres becomes possible. This is accomplished by the receiver keeping track of the number of wavefronts that arrive. A variation of the number of wavefronts that arrive at the receiver within a certain period indicates a change of distance between the satellite and the receiver. This is due to the Doppler effect which causes a change in wavelength due to movement.

Up to this point, two simplifications had been made about timing biases. The first of these is that there is a single clock bias, the one between the satellite clocks and the receivers. In practice, this is not the case as there are two clock biases. The first of these is the satellite clock bias caused by clock drift, and the second is the difference between the satellite clocks and the receivers. However, the information about the satellite clocks is encoded in the message transmitted by the satellites and thus receivers are capable of modelling most of the errors caused by drift using a polynomial equation of the form [26]:

$$^{j}\delta(t) = a_0 + a_1(t - t_0) + a_2(t - t_0)^2 \tag{2.2}$$

where $^{j}\delta(t)$ is the bias caused by errors in the j-th satellite's clock, a_x are polynomial coefficients and t_0 a reference time.

As such, assuming that $_{i}\delta(t)$ is the bias of the i-th receiver's clock, that is the difference between the i-th receiver's clock and the satellites, and knowing that

${}^{j}\delta(t)$ can be modelled, the residual bias can be written as:

$$\Delta_i^j\delta(t) = {}^{j}\delta(t) - {}_{i}\delta(t) \approx C_b \tag{2.3}$$

where $\Delta_i^j\delta(t)$ is the total residual clock bias. Of note, the model in Equation (2.2) will not precisely match the satellite clock bias, and thus some residual error remain. However, in practice it can be said that $\Delta_i^j\delta(t)$ is approximately equal to C_b.

The second simplification was that the clock bias between the receiver and the satellite clocks remained the same. In practice, this is true, but only for a single epoch (i.e. a single measurement time). At each time range to the satellites is measured, the clock bias between the satellites and the receiver changes.

Therefore, the carrier-phase observable, or the range based on carrier-phase measurement from the j-th satellite as seen by the the i-th receiver at time t, can be written as:

$$\frac{j}{i}\varrho\,(t) = \frac{1}{\lambda}\,\frac{j}{i}d\,(t) + \frac{j}{i}N + {}^{j}f\Delta_i^j\delta\,(t) \tag{2.4}$$

where $\frac{j}{i}\varrho(t)$ is the carrier-phase observable, $\frac{j}{i}N$ is the integer ambiguity, ${}^{j}f$ is the frequency of the j-th satellite's signal, and $\frac{j}{i}d(t)$ is

$$\frac{j}{i}d(t) = \sqrt{(x_u - {}^{j}x)^2 + (y_u - {}^{j}y)^2 + (z_u - {}^{j}z)^2} \tag{2.5}$$

where $({}^{j}x, {}^{j}y, {}^{j}z)$ is the position of the satellite in 3D space. Substituting Equation (2.3) into Equation (2.4), the following is obtained:

$$\frac{j}{i}\varrho(t) = \frac{1}{\lambda}\,\frac{j}{i}d(t) + \frac{j}{i}N + {}^{j}f\,{}_{i}\delta - {}^{j}f{}^{j}\delta \tag{2.6}$$

From Equation (2.2), one of the unknown values from the above is eliminated, leaving only the integer ambiguity, the receiver clock bias and the position of the user as variables. If the value of the integer ambiguity is known, then it is possible to solve for the user's position using the iterative method shown in Section A.4.3.

2.2.3 GPS Signal Acquisition

In Section 2.2.1, the topic of satellite signal acquisition was briefly mentioned. This section explains the mathematical means by which GPS receivers acquire signals from satellites.

For a given stochastic process, $x(t)$, the autocorrelation function is given by [16]:

$$R_x(t_1, t_2) = \overline{x(t_1)x(t_2)} = \int_{-\infty}^{\infty}\int_{-\infty}^{\infty} x_1 x_2 f_x(x_1, x_2)\,\mathrm{d}x_1\,\mathrm{d}x_2 \tag{2.7}$$

where $x_1 = x(t_1)$ and $x_2 = x(t_2)$, and $f_x(x_1, x_2)$ is the probability density function (pdf) of $x(t)$. The autocorrelation function has a final value in the range $(0, 1)$ inclusively and is a measure of the similitude between a particular process and a time-shifted version of itself. If $R_x(t) = 1$ then the two signals are identical.

For digital communications with zero-centered signals, that is signals where $\{0, 1\}$ are represented by $\{-1, 1\}$, the autocorrelation function can be redefined as follows [49]:

$$R_x(k) = \frac{1}{N}\sum_{n=0}^{N-|k|-1} x(n)x(n + |k|) \tag{2.8}$$

where $x(n)$ is the signal whose autocorrelation is to be calculated, k is the time-shift to apply to the signal and N the number of bits considered in x. This function will give a value in the range $(0, 1)$ inclusively and the same conclusions as above can be drawn.

In the same manner, cross-correlation between two different signals can be defined as:

$$R_{xy}(k) = \frac{1}{N}\sum_{n=0}^{N-|k|-1} x(n)y(n + |k|) \tag{2.9}$$

where $x(n)$ and $y(n)$ are the two signals, and $y(n + |k|)$ is a shifted version of $y(n)$. The cross-correlation gives the similarity between the two different signals.

As was mentionned in Section 2.2.1, each satellite is assigned a unique and periodic pseudo-random code. Every GPS receiver has knowledge of the pseudo-random codes assigned to each satellite. Receivers acquire a signal by matching a local copy of a particular pseudo-random code to the signals received from the satellites. This is accomplished using cross-correlation as shown below:

$$R_{xy}(k) = \frac{1}{m}\sum_{n=0}^{m-1} x(n)y(n + k) \tag{2.10}$$

where $x(n)$ is the received signal, $y(n+k)$ the local time-shifted copy of a particular pseudo-random code, k the applied shift and m the length of the code. The value of k directly indicates the time of travel of the signal from the satellite to the receiver. Notice that in Equation (2.10) the term k is absent from the summation limits. This is a requirement due to the fact that $k \in \mathbb{R}$.

The use of cross-correlation to acquire satellite signals leads to the following conclusions:

1. When $R_{xy}(k) \approx 1$, the receiver has locked on to the signal from a particular satellite.

2. The cross-correlation between the pseudo-random codes of different satellites must be near zero, i.e. different pseudo-codes must be nearly orthogonal.

3. The clock bias is caused by inaccuracies in the value of k in Equation (2.10).

Once the first condition is satisfied, the receiver can then decode the satellite's signal to extract transmitted information, such as time stamps and ephemeris coordinates, by using the specific pseudo-random code assigned to that particular satellite. Once the receiver has locked on to four individual satellites, it can then estimate the user's position in three dimensions.

The second conclusion is a requirement for such a system to operate properly. If it is not satisfied, then it becomes impossible to distinguish between the signal transmitted by two or more satellites.

2.2.4 The Integer Ambiguity

The carrier-wave has no obvious start or end point due to the fact that it appears to be a periodic signal. Although the receiver is capable of determining the current phase of the carrier-wave to a fraction of a cycle, it is incapable of determining the number of full wavelengths that initially separate it from the satellite. Thus, the integer ambiguity term appears as the receiver arbitrarily estimates that value.

Solving the integer ambiguity is a major research problem and a number of papers dedicated to explaining new algorithms or techniques to solve this ambiguity abound. For example, the recent paper by Yoon et al. [60] describes a real-time algorithm that considerably improves on the efficiency of the search and motion detection methods.

However, in this author's opinion, the simplest solution is to utilise phase information from both the $L1$ and $L2$ carrier wave signals. This allows the receiver to utilise wide-lane frequencies, that is the frequency obtained by subtracting the frequency of $L1$ from that of $L2$. However, not all receivers are capable of making measurements on both frequencies at once. Basics of the wide-lane method are detailed in Reference [26].

For this method, it is necessary to slightly redefine the phase observable as:

$$\varrho = \frac{1}{\lambda}d + f\Delta\delta + N - \frac{1}{\lambda}\Delta_{ionosphere} \tag{2.11}$$

If this is not done, then the ambiguity will be a real number, and not an integer number. Consider that ϱ_{L1} and ϱ_{L2} are the phase observables for the $L1$ and $L2$ frequencies respectively. The wide-lane phase observable can be defined as:

$$\varrho_w = \varrho_{L1} - \varrho_{L2} \tag{2.12}$$

Additionally, it is known that:

$$\Delta_{ionosphere} \propto \frac{40.3}{f^2}\tau \tag{2.13}$$

where τ is the Total Electron Content (TEC) in the ionosphere. From the above it is possible to substitute as follows:

$$\lambda = \frac{c}{f} \qquad\qquad \Delta_{ionosphere} = \frac{\beta}{f^2} \tag{2.14}$$

into the previous equations, ϱ_w can be re-written as:

$$\varrho_w = \frac{f_w}{c}\,d + f_w\Delta\delta + N_w - \frac{\beta}{c}\left(\frac{1}{f_{L1}} - \frac{1}{f_{L2}}\right) \tag{2.15}$$

where f_w is the wide-lane frequency and N_w the wide-lane ambiguity, where:

$$\begin{aligned} f_w &= f_{L1} - f_{L2} \\ N_w &= N_{L1} - N_{L2} \end{aligned} \tag{2.16}$$

Upon having obtained a solution for N_w, a simpler process than solving explicitly for either N_{L1} or N_{L2}, it is now possible to obtain an expression where one of the ambiguities for a single frequency, in this case $L1$, appears as follows:

$$\frac{1}{f_{L1}}\varrho_{L1} - \frac{1}{f_w}\varrho_w = \frac{N_{L1}}{f_{L1}} - \frac{N_w}{f_w} - \frac{\beta}{cf_{L1}^2} + \frac{\beta}{cf_w}\left(\frac{1}{f_{L1}} - \frac{1}{f_{L2}}\right) \tag{2.17}$$

which can be rearranged to the following with simple algebra:

$$N_{L1} = \varrho_{L1} - (\varrho_w - N_w)\frac{f_{L1}}{f_w} + \frac{\beta}{cf_{L1}} - \frac{\beta}{cf_w}\left(1 - \frac{f_{L1}}{f_{L2}}\right) \tag{2.18}$$

Using some of the equivalences mentioned above, this can be reduced to:

$$N_{L1} = \varrho_{L1} - (\varrho_w - N_w)\frac{f_{L1}}{f_w} + \frac{\beta}{c}\frac{f_{L1} + f_{L2}}{f_{L1} f_{L2}} \tag{2.19}$$

To obtain an expression for the $L2$ ambiguity, one would simply need to do the following:

$$\frac{1}{f_{L2}}\varrho_{L2} - \frac{1}{f_w}\varrho_w = \frac{N_{L2}}{f_{L2}} - \frac{N_w}{f_w} - \frac{\beta}{c f_{L2}^2} + \frac{\beta}{c f_w}\left(\frac{1}{f_{L1}} - \frac{1}{f_{L2}}\right) \tag{2.20}$$

which can also be rearranged similarly to above.

In the case of single frequency receivers it may be necessary to take measurements over several epochs before the required number of equations is obtained to solve the system. This causes serious problems in real-time applications.

However, as will be shown in the next few sections, it may not even be necessary to solve for the integer ambiguity. A final note about this topic: The interested reader should refer to Section 9.1.3 of Reference [26]. It details a number of other methods that can be used to solve the integer ambiguity.

2.2.5 Differential Carrier-Phase GPS

Differential Carrier-Phase GPS (DCPGPS) is the surveyor's tool and the navigation instrument *par excellence*. In most cases, DCPGPS is utilised to measure relative positions between two receivers, or the vector between two receivers. This vector is known as a baseline.

To obtain this information, the receivers will usually calculate the differences between simultaneous observables from different receivers. The simplest type of these is the single-difference. In this type of operation, the difference between observables from a single satellite is calculated. For simplicity, the two receivers will be referred to as a and b, the satellite as i, and the same notation introduced earlier will be used. From Section 2.2.2, it is known that:

$$\begin{aligned} {}^{i}_{a}\varrho\,(t) &= \frac{1}{\lambda}\,{}^{i}_{a}d\,(t) + {}^{i}_{a}N + {}^{i}f\Delta^{i}_{a}\delta\,(t) && (2.21)\\ {}^{i}_{b}\varrho\,(t) &= \frac{1}{\lambda}\,{}^{i}_{b}d\,(t) + {}^{i}_{b}N + {}^{i}f\Delta^{i}_{b}\delta\,(t) && (2.22) \end{aligned}$$

A single difference is obtained by:

$${}^{i}_{a}\varrho(t) - {}^{i}_{b}\varrho(t) = \frac{1}{\lambda}\,{}^{i}_{a}d(t) + {}^{i}_{a}N + {}^{i}f\Delta^{i}_{a}\delta(t) - \frac{1}{\lambda}\,{}^{i}_{b}d(t) - {}^{i}_{b}N - {}^{i}f\Delta^{i}_{b}\delta(t) \tag{2.23}$$

From Equation (2.3), the above can be rewritten as:

$$ {}^{i}_{a}\varrho(t) - {}^{i}_{b}\varrho(t) = \frac{1}{\lambda}\,{}^{i}_{a}d(t) + {}^{i}_{a}N + {}^{i}f_{a}\delta(t) - \frac{1}{\lambda}\,{}^{i}_{b}d(t) - {}^{i}_{b}N - {}^{i}f_{b}\delta(t) \tag{2.24} $$

To simplify writing such equations in the future, the following shorthand will now be used:

$$ {}^{i}_{ab}N = {}^{i}_{a}N - {}^{i}_{b}N \tag{2.25} $$

$$ {}_{ab}\delta(t) = {}_{a}\delta(t) - {}_{b}\delta(t) \tag{2.26} $$

$$ {}^{i}_{ab}d(t) = {}^{i}_{a}d(t) - {}^{i}_{b}d(t) \tag{2.27} $$

$$ {}^{i}_{ab}\varrho(t) = {}^{i}_{a}\varrho(t) - {}^{i}_{b}\varrho(t) \tag{2.28} $$

This results in the following equation for a single-difference:

$$ {}^{i}_{ab}\varrho(t) = \frac{1}{\lambda}\,{}^{i}_{ab}d(t) + {}^{i}_{ab}N + {}^{i}f_{ab}\delta(t) \tag{2.29} $$

Single-differences as shown above have the advantage that the dependence on ${}^{i}\delta(t)$ has been removed entirely from the equation. Thus, the i-th satellite's clock bias does not have any impact on the precision of the solution.

Similarly, it is possible to remove the dependence of the solution on the receiver clock bias by taking a double-difference. A double-difference is obtained by taking the difference of two single differences from the same receivers. Consider the following single-differences resulting from measurements taken from satellite i and j:

$$ {}^{i}_{ab}\varrho(t) = \frac{1}{\lambda}\,{}^{i}_{ab}d(t) + {}^{i}_{ab}N + {}^{i}f_{ab}\delta(t) \tag{2.30} $$

$$ {}^{j}_{ab}\varrho(t) = \frac{1}{\lambda}\,{}^{j}_{ab}d(t) + {}^{j}_{ab}N + {}^{j}f_{ab}\delta(t) \tag{2.31} $$

Taking the difference between the two:

$$ {}^{i}_{ab}\varrho(t) - {}^{j}_{ab}\varrho(t) = \frac{1}{\lambda}\,{}^{i}_{ab}d(t) + {}^{i}_{ab}N + {}^{i}f_{ab}\delta(t) - \frac{1}{\lambda}\,{}^{j}_{ab}d(t) - {}^{j}_{ab}N - {}^{j}f_{ab}\delta(t) \tag{2.32} $$

However, as the satellites transmit on the same frequency, the terms with dependence on f can be eliminated, leaving:

$$ {}^{i}_{ab}\varrho(t) - {}^{j}_{ab}\varrho(t) = \frac{1}{\lambda}\,{}^{i}_{ab}d(t) + {}^{i}_{ab}N - \frac{1}{\lambda}\,{}^{j}_{ab}d(t) - {}^{j}_{ab}N \tag{2.33} $$

By introducing the following shorthand:

$$\begin{aligned} {}^{ij}_{ab}\varrho(t) &= {}^{i}_{ab}\varrho(t) - {}^{j}_{ab}\varrho(t) && (2.34)\\ {}^{ij}_{ab}N &= {}^{i}_{ab}N - {}^{j}_{ab}N && (2.35)\\ {}^{ij}_{ab}d(t) &= {}^{i}_{ab}d(t) - {}^{j}_{ab}d(t) && (2.36) \end{aligned}$$

the double-difference equation can be rewritten as:

$${}^{ij}_{ab}\varrho(t) = \frac{1}{\lambda}\,{}^{ij}_{ab}d(t) + {}^{ij}_{ab}N \tag{2.37}$$

As mentioned above, another term has been eliminated. Now, the equation is no longer dependent on the receiver's clock bias, but only on the distance between the satellites and the integer ambiguity.

In Section 2.2.4, it was mentioned that the integer ambiguity could be eliminated from the equation. This is done using a triple-difference. However, unlike the single and double-differences, a triple-difference requires taking the difference between double-differences resulting from two consecutive epochs. Thus, utilising this technique introduces a delay in the processing. Consider the following double differences:

$$\begin{aligned} {}^{ij}_{ab}\varrho(t_1) &= \frac{1}{\lambda}\,{}^{ij}_{ab}d(t_1) + {}^{ij}_{ab}N && (2.38)\\ {}^{ij}_{ab}\varrho(t_2) &= \frac{1}{\lambda}\,{}^{ij}_{ab}d(t_2) + {}^{ij}_{ab}N && (2.39) \end{aligned}$$

To obtain the triple-difference, it is necessary to subtract the two as follows:

$${}^{ij}_{ab}\varrho(t_1) - {}^{ij}_{ab}\varrho(t_2) = \frac{1}{\lambda}\,{}^{ij}_{ab}d(t_1) + {}^{ij}_{ab}N - \frac{1}{\lambda}\,{}^{ij}_{ab}d(t_2) - {}^{ij}_{ab}N \tag{2.40}$$

From the above it is clear that the result will be:

$${}^{ij}_{ab}\varrho(t_1) - {}^{ij}_{ab}\varrho(t_2) = \frac{1}{\lambda}({}^{ij}_{ab}d(t_1) - {}^{ij}_{ab}d(t_2)) \tag{2.41}$$

By introducing the following shorthand:

$$\begin{aligned} {}^{ij}_{ab}\varrho(t_1t_2) &= {}^{ij}_{ab}\varrho(t_1) - {}^{ij}_{ab}\varrho(t_2) && (2.42)\\ {}^{ij}_{ab}d(t_1t_2) &= {}^{ij}_{ab}d(t_1) - {}^{ij}_{ab}d(t_2) && (2.43) \end{aligned}$$

it is possible to rewrite the triple-difference as:

$$\overset{ij}{ab}\varrho(t_1t_2) = \frac{1}{\lambda}\overset{ij}{ab}d(t_1t_2) \tag{2.44}$$

With the elimination of the integer ambiguity, the system is no longer sensitive to cycle slips and it is only necessary to solve for the position of the receivers in almost identical fashion as described in Section A.4.3.

Finally, it is possible to perform the same type of process on the code observable, however the level of accuracy would likely be several orders of magnitude lower due to the longer chip-length. The interested reader should refer to Section 8.2 of Reference [26] where other differential methods are covered for both the carrier-phase observable and code observable.

2.2.6 Cycle Slips

A receiver will count the number of wavefronts that arrive for as long as it maintains a lock on any particular satellite. Should a lock be lost for any reason, the receiver will once again arbitrarily estimate the number of full wavelengths that separate it from the satellite as it would the first time it locks on to a signal. This will likely result in a discontinuity in the phase observable. This phenomenon is known as a cycle slip.

Detection of a cycle slip is by no means obvious, and depending on the type of setup utilised, the detection method may vary. This project will be using multiple receivers and thus it is only necessary to check single, double or triple differences to detect the cycle slip. It may also be possible to detect cycle slips by a single stationary receiver when there is a massive change in position between epochs. The correction of the cycle slip involves determining how large the slip itself was and then applying this correction to the phase observable itself.

Of note, many receivers implement automatic cycle slip detection and correction procedures, thus the user is never aware of such events occuring unless the receiver is programmed to broadcast a warning. Finally, the interested reader should refer to Section 9.1.2 of Reference [26]. This section details the procedure for use in detecting and correcting cycle slips in the case of a dual-frequency receiver.

2.3 Augmented GPS Systems

In this section, augmented versions of GPS are considered. Augmented systems allow for greater accuracy and reliability when using GPS, a key factor in cases

where GPS is used in safety-critical applications. Three systems are considered: Differential GPS (DGPS), Wide Area Augmentation System (WAAS) and the European Geostationary Navigation Overlay Service (EGNOS).

2.3.1 Differential GPS

Although the regular GPS service is capable of accurately locating a user to within 50 metres, Differential GPS (DGPS) offers means by which accuracy can be improved by approximately one order of magnitude, and sometimes more depending on the user's position.

DGPS consists of a series of ground stations with precisely known locations obtained using accurate surveying. These stations then utilise the satellite's signals to calculate their position as described earlier. They then compare the result to their known position and calculate the corrections necessary to reverse the errors introduced by some of the inaccuracies mentioned earlier. The base stations do this for each individual satellite visible above a certain elevation, usually 7.5 degrees, and then broadcast the corrections for users in the surrounding area.

These corrections will have the effect of removing several sources of error including, ionospheric delay, ephemeris errors and satellite clock drift. Additionally, DGPS had the ability to render somewhat useless the effects of Selective Availability (SA), a service degredation method used by the USAF. However, DGPS does not correct in any way the effects of multi-path, and this particular source of error may actually be made more severe by the DGPS corrections.

In general, an Radio Technical Commission for Maritime Services (RTCM) protocol is used for the purpose of broadcasting corrections to the rovers. The rovers in the area then adjust their own position based on the information received from the base station. Of note that there are multiple versions of the RTCM protocol, and the receivers used later in this project were compatible with the deprecated RTCM 2.2 protocol. Reference [22] provides a more detailed insight into the DGPS system operated by the USCG.

Although DGPS is a useful system for many particular applications, including harbour approaches, it is not accurate enough for the purposes of this project and therefore is not considered any further.

2.3.2 WAAS and EGNOS

The Wide Area Augmentation System, or WAAS for short, was designed by the United States Federal Aviation Administration (FAA) for use in precision aviation

navigation. Although GPS provides fairly accurate positions for navigational purposes, the FAA did not believe that unmonitored GPS was sufficient for use in precision approaches, and thus the concept of WAAS was born.

WAAS consists of data gathering stations, data processing stations, ground communication links, as well as geostationary communications satellites and their associated ground stations. The data gathering stations acquire data on the status of the WAAS and GPS satellites and transmit these to the data processing stations. The data processing stations then generate WAAS messages which can contain information on the health of the satellites, the integrity of the data received or corrections to apply. These messages are then broadcast to the entire area of coverage by the geostationary satellites [17].

A major advantage of WAAS is that it also operates on the $L1$ frequency using similar codes to the GPS satellites. Therefore, only minor modifications of current receivers are needed in order for the public to make use of WAAS.

EGNOS, the European Geostationary Navigation Overlay System, is the European equivalent to WAAS. It operates using the same principles as WAAS. Of note, EGNOS will remain operational with the introduction of Galileo [55].

As with DGPS, the accuracy gains provided by the WAAS and EGNOS systems are not sufficient to achieve the project goals, and therefore, both systems are not considered any further.

2.4 Previous Use of GPS in Structure Analysis

In this section, the results of a literature survey are highlighted. It first briefly explains an early use of GPS for this purpose and then shows that the technique has been refined over the past few years. A comparison between the conditions under which the previous surveys were conducted, and the conditions of this project will then be presented. Finally, this section considers another application of GPS where similar conditions are seen.

2.4.1 Historical Overview of GPS in Structural Analysis

The idea of using GPS for the purpose of structural analysis is not novel by any means. The technique has been around for at least ten years as evidenced by a paper written by Lovsy et al. in 1995 [40]. In this paper, the movement of the Calgary Tower—a 190.8 m high tower located in Calgary, Alberta, Canada—is measured under very windy conditions using a differential carrier-phase approach. Lovse

et al. utilised a double-difference approach, allowing them to eliminate clock bias errors as shown in Section 2.2.5. Additionally, a short baseline was utlised, thus removing further error sources.

The results described in Lovsy et al. show that the tower swayed by about 30 mm in the North-South direction and by about 10 mm in the East-West direction. The frequency of oscillation of the tower was also obtained and found to be approximately 0.3 Hz. Of note, this was one of the first papers where GPS was used to obtain such information and it has been cited by a number of scholars since its publication.

Prior to the emergence of GPS technology that could be used for structural analysis, such analysis was conducted via visual inspection, laser or electronic ranging, or with the aid of accelerometers and inertial techniques. The latter was usually the preferred method at the time due to its fairly low cost. However, there are major problems with inertial techniques. Inertial techniques involve measuring the acceleration of the body with the help of accelerometers, and then integrating the result to obtain velocity. To obtain displacement, integration is performed on velocity. The output of accelerometers is known to drift with time, and thus a reliable result cannot always be obtained.

A solution to this problem involves combining an inertial system with GPS. Such a system is detailed by Farrell et al. in their 2000 paper [20]. Although Farrell et al. were working on autonomous vehicle control, the results they obtained are still relevant to this particular project. Furthermore, they claim to be the first to have developed a real-time DCPGPS-aided inertial system.

In their experiment, Farrell et al. combined an inertial navigation system (INS) and a DCPGPS setup. Using this enhanced INS, they were able to achieve positioning accuracies of 2 cm for table top movement, and 6cm for movement in an amusement park ride. However, their paper concludes that better accuracies are possible for such systems as they had not properly calibrated the INS to standards that could be achieved in a mass-production environment.

The experiments described by Farrell et al. are all conducted along a single path over relatively short distances and times, an important difference to the experimental setup that is proposed for this project. In this project, it is clear that ships are not limited to operating for times ranging between 120 and 150 seconds. Rather, ships may travel for days and weeks on end and cover distances of several thousand kilometres in one leg. This could pose a serious problem, especially if the drift of accelerometres is statistically important. However, modern improvements to integrated circuits seems to have reduced the importance of this fact as explained in

Section 2.6.

Also in 2000, Nakamura [44] published a paper in which is described a technique to measure wind-caused displacement of bridges using DCPGPS. CPGPS receivers were placed on the girders of a 720m long suspension bridge and used to measure the movement of these components. The data obtained is then compared to that obtained using inertial techniques and is found to be strikingly similar. Thus, Nakamura concludes that GPS can be used to obtain results similar to that which can be obtained using inertial techniques alone. However, unlike accelerometers, GPS is not subject to drift and as such, barring any malfunction in the system, provides a long-term accurate solution. Furthermore, Nakamura made use of frequency-domain analysis (i.e. Fourier transforms), a similar technique that was utilised in the development of the simulators presented later in this thesis.

A combination of an inertial system and DCPGPS has been used to measure the displacement of a bridge. In 2004, Roberts et al. [50] published a paper where such a system was used to monitor a footbridge in Nottingham. They concluded that millimetre accuracy was possible with such a system, or with DCPGPS alone, provided that proper precautions and mitigation measures are in place. The paper also presented the algorithms that were utilised by Roberts et al. in their monitoring endeavour.

More recently, the GPS has been used by Guo et al. to measure the structural movement of the Humen Bridge, China [21]. Guo et al. used a similar technique to that used by Lovsy et al., with the difference that instead of using a series of receivers at a single point, Guo et al. used twelve receivers located at different areas on the bridge. DCPGPS was still used, but this network of receivers gave them the ability to make a number of additional measurements such as torsional displacement instead of limiting them to translational movement. Guo et al. were able to determine lateral movement and vertical movement under different wind and temperature conditions respectively.

However, the use of GPS for real-time monitoring introduces a few additional complications with regards to data processing. First, GPS receivers can easily generate megabytes of information per day, and depending on the sampling rate and / or the sheer number of receivers in the system, megabytes of information can be generated in only a few minutes.

Furthermore, should the user wish to process information on every available baseline (i.e. the line between every receiver in the system), the numbers may be staggering. A paper by Duff et al. [19] contains an example where thirteen receivers are setup in a network. There are a total of seventy-eight available base-

lines, a number that is manageable. However, should the number of receivers be increased significantly, this could become unmanageable depending on the setup that is in use. Proper selection of which baselines to use is obviously an issue. Finally, another paper by Duff et al. [18] concludes that time averaging is a necessity to obtain millimetre accuracy. This obviously represents an issue for real-time analysis.

2.4.2 Comparison of the Monitoring Conditions

All the papers mentioned in the previous section, except the one by Farrell et al., have one thing in common: They utilised a differential approach with a fixed reference point. This has the advantage that with time averaging, a very accurate position fix for this base station, as well as the rovers (mobile receivers), can be obtained. This project concerns itself with a fully mobile structure and therefore cannot take advantage of this technique. It is not possible to extrapolate with certainty the accuracy that will be obtained on board a vessel from the results in the above-mentioned papers and this was a potential issue with this project. However, one can draw on the experiences of the space industry where serious efforts are being made at present to vastly improve the accuracy of stand-alone GPS receivers.

2.4.3 The Use of GPS in Spacecraft

Under certain circumstances, there can be a use for GPS receivers onboard spacecraft. Specifically, for any mission in low earth orbit (LEO), it is possible to use GPS in attitude control, navigation and positioning. The need for the mission to be LEO is due to the fact the GPS satellites (located in MEO) have their antennas pointed at the Earth's surface. Thus, any satellite that is to make use of the GPS constellation must generally orbit at a lower altitude. Additionally, for the spacecraft to be able to make use of the GPS satellites, they must be inside the particular satellite's coverage cone.

As early as 1995, the use of GPS receivers onboard the International Space Station (ISS) was considered for attitude control systems (ACS) [30]; this was approximately three years before the construction of the station even begun. Today, GPS is in use in the ISS ACS, but it is complemented by laser gyroscopes.

More recently, GPS-based systems for use in satellite formation flying have been considered, and even prototyped using hardware-in-the-loop (HTL) simulation. In their 2002 paper, Montenbruck et al. [43] describe an HTL simulated system that achieves accuracies of 0.5 m and 1 cm / s respectively for position and velocity. This

type of system has been compared to other models that use Hill or COWPOKE equations by Ahmed et al. [8] in their 2005 paper.

However, of all current missions, it is the Gravity Recovery And Climate Experiment (GRACE) mission which seems to have the most innovative uses for GPS. Launched in 2002, the GRACE mission consists of two twin satellites, on the same orbit, which are separated by a few hundred kilometres. The mission objectives are twofold: The first is to obtain better representations of the gravity fields of the Earth, and a secondary objective is to determine the effects of the atmosphere on GPS signals.

To this end, the GRACE satellites carry high-precision GPS receivers. These are used to determine the precise location of the satellites, thus the exact location of any anomalies, and to sound the effects of the atmosphere on GPS signals. It was shown in a paper published by Kang et al. [33] that using GPS data alone to determine orbit probably led to accuracies of the order of 1.0cm in the radial direction and 2.5cm in along-track and cross-track directions. Additionally, gravity field models resulting from the data acquired by GRACE have already been made public. With the mission's life expectancy of five years due to end at the end of 2007, it is certain that more results will be forthcoming. For further information on the GRACE mission, the interested reader should refer to Reference [53].

2.5 Current use of GPS on Vessels

GPS is not generally utilised onboard vessels for structural analysis. It is used mostly, and in most cases exclusively, for navigation purposes. In fact, DGPS was originally implemented by the USCG in order to augment the accuracy of harbour navigation and harbour approaches [22].

More recent systems have made use of EGNOS to greatly enhance harbour approaches. One such system, MARLET, is described by a European Space Agency (ESA) press release [1]. The MARLET system was implemented in Hamburg, Germany, and achieved accuracies of the order of less than one metre. However, although MARLET is useful for precision navigation, it does not achieve the accuracies required to measure structural deformation. Centimetre-level or better accuracy is required for that purpose.

Furthermore, contrary to popular belief, collision-avoidance onboard vessels is not achieved by the use of GPS alone, but rather by the use of the Automatic Identification System (AIS). AIS transponders broadcast vessel specific information, including position data obtained by the use of the GPS, on a very high frequency

(VHF) link. This information is analysed by each surrounding vessel and a plot of the surrounding areas, including vessel traffic, can be obtained. This system is in many ways very similar to the Traffic alert and Collision-Avoidance System (TCAS), which is currently in use onboard aircraft, however TCAS has additional features such as collision resolution [42].

Recently, there has been evidence that the GPS can be used for attitude determination. In their paper, Hoyle et al. [28] investigate the use of low-cost GPS receivers with a variety of different antennae in different configurations. All their data was sampled at the rate of 1 Hz, and they aimed to measure pitch, roll and heading. They achieved results of varying accuracy depending on the configuration they utilised. Furthermore, the actual datum they were trying to measure seemed to have a major influence on the accuracy. Furthermore, they found that a number of factors affected the accuracy of their receivers. These include, but are not limited to, antenna phase centre stability, receiver noise and dilution of precision. They further revealed that some factors had not been taken into account. They specifically mention, amongst others, the impact of the data rate on their capability to solve the ambiguity and the dynamics of the vehicle in question, therefore their results may still contain large errors.

Additionally, there has been, to this author's knowledge, only one documented case where GPS recievers have been explicitely used onboard ships to monitor ship flexure. This documented case is found in Reference [46]. In this paper, Petovello et al. describe how they used a dual GPS and INS approach to monitor the flexure of the United State's Navy (USN) aircraft carrier *USS Dwight Eisenhower*'s yardarm over nine days in May 2005.

Although the ultimate motivation behind the Petovello et al. paper is the USN's goal to develop the Joint Precision Approach and Landing System (JPALS), it remains nonetheless the most relevant piece of literature that was uncovered. The idea behind JPALS is to provide an aircraft with accurate information the carrier in preparation for a carrier landing, an operation widely recognised by fighter pilots as one of the most hazardous aviation undertakings. However, it is impossible to place an antenna on the flight deck itself for operational reasons, and thus, these are placed on the yardarm.

However, the yardarm itself may flex and deform and as such, it is necessary to measure this motion. In their paper, Petovello et al. found that they obtained estimates of the yardarm's motion which had a standard deviation of 2cm or less. They further found that rough seas caused an increase by a factor of approximately 1.6 on the horizontal axes of the yardarm's motion, but that very little change oc-

cured on the vertical axis. Additionally, they found that the motion of the yardarm along the starboard / port axis was strongly correlated to the lateral acceleration of the ship.

2.6 Current Vessel Structural Monitoring Techniques

In this section, techniques currently used to monitor the integrity of a ship's hull are presented. Structural monitoring systems aim to allow a user to determine the safety of a structure by measuring the force exerted upon it or the distortion it suffers.

There are two classical techniques to make these measurements. The first, referred to as the inertial method, involves the use of accelerometers. In such systems, the acceleration of a specific point on the ship is measured using an accelerometer, and the result integrated twice to obtain position. Regrettably, accelerometers are known to be subject to drift and thus the inaccuracy will likely be quite high.

Modern improvements in integrated circuit technology have reduced the importance of the error associated with accelerometer. For example, Honeywell are now marketing an accelerometre that, according to the datasheet [5], will not have a drift of more than 7000μg. However, such improvements come with a significant price tag. The QA1400 is advertised by Honeywell at a starting price of over $2,000USD per unit. Clearly, this might be an issue if cost of the system is a major factor of a design, although given the high cost of a cargo ship, this may be a small price to pay in the long run.

The second classical technique involves the use of electronic strain gauges. A strain gauge's output is directly related to the deformation to which it is subjected. Thus, when a network of gauges is installed on a ship's hull, it may be possible to measure the deformation of the hull. Although this technique would seem to be the best solution, there are a few drawbacks. The first is that the wiring required to connect the gauges may be extensive. Furthermore, strain gauges must be fairly large in order to measure the deformation over a certain distance. Strain gauges are also quite sensitive to changes in temperature. However, the most important issue related to the use of strain gauges is the large amount of noise in the data that is collected when compared to the data collected with fibre optic sensors [58].

The use of fibre optic sensors is the latest addition to the field of structural monitoring. By embedding fibre optics into a ship's hull, it is possible to measure displacement based on the principle of interferometry [32]. Furthemore, by using

optical sensors, it was possible to detect a break in the structure as some of the light travelling into the optical fibre would be reflected back to the source. However, Kageyama et al. found that such setups are limited in their ability of detecting movement having a frequency below 1 Hz.

Further work in this field was done by Wang et al. [58]. In their experiement, they setup a fibre-optics monitoring system onboard *HNoMS Skjold*, a ship of the Norwegian Navy. Using their setup, they measured strain on the vessel in periods of 120 seconds for several type of motions. They determined that their error was no more then:

$$E \leq 0.16\mu\epsilon \tag{2.45}$$

where μ and ϵ are the magnetic permeability and the permittivity of the fibre respectively, and the units of E are in $\sqrt{\text{Hz}}$.

Wang et al. managed to measure strains compartively to the value of $\mu\epsilon$ and moments of the order of several mega Newtons. Specifically, they used wavelet methods to identify motion and / or strain linked to bending due to sea states (i.e. waves) and whipping vibration. The question of computing-efficiency is resolved as they indicate their system works in real-time. The main question when compared to a GPS-based system would be that of cost-benefit or more accurately of cost versus accuracy of the system.

There is additionally a question as to how flexibly a fibre-optic system can be deployed and how easy it is to modify once installed. The GPS-based system is extrememly easy to redeploy, especially if the installation is done using wireless communications as was done onboard *Red Jet 4* for the practical work.

Theoretical simulation of ship structures, usually done using Finite Element (FE) modelling, is also a common staple of this field. There are numerous examples of papers where FE models are used. A particularly interesting one is that by Hirdaris et al. [25] where the sturcture of the OBO *MV Derbyshire* is considered using such a model. This paper by Hirdaris et al. was used as a benchmark to test the accuracy of some of the simulator results presented later.

2.7 Summary

In this section, a brief history of navigation and satellite navigation was covered. More importantly, the principles of operation of most satellite navigation systems presented. These techniques were used later in practical work. Additionally, the ability of the GPS to serve as more than a simple navigation device was shown. It is this flexibility, particularly the ability to use GPS data for measurement of flexion

and attitude, as well as navigational purposes that will is exploited in this work.

Chapter 3

Theoretical Simulation

3.1 Introduction

In this chapter, the design and results obtained from a ship simulator are considered. As it is well-recognised that large vessels, such as supertankers and supercargos, may suffer deflections of the order of metres under severe conditions [25], it is possible a GPS system might be able to measure these. Theoretical simulation is a key component of this research, and is the primary means of determining whether the project goals are acheivable. This simulator was developed in two stages. The first stage simulator was limited to rigid body motion whereas the second stage simulator also included transversal bending modes.

In this chapter, the rigid-body version of the simulator is presented first, alongside results it generated. This is followed by an explanation of how a ship was modelled for the flexible-body version. The results obtained from this second simulator, and a brief explanation of the theory of frequency-domain analysis follows. The chapter will conclude with an analysis of the impact the deployment of the Galileo Constellation is expected to have on satellite navigation, and more particularly on this project.

3.2 The Rigid-Body Simulator

In order to gauge the accuracy of the results that could potentially be obtained onboard a ship, a MATLAB simulator was developed. It simulates the behaviour of any number of GPS receivers placed onboard a fully rigid structure, assumed to be a ship. This structure can be drifting, rotating and subjected to the movement of waves all at the same time. The ship movement was simulated by matching the pitch and roll of a travelling sine wave having a user-defined direction, speed and

amplitude. However, the simulator has limitations. For example, it assumes the entire area the structure covers during the simulation to be a plane.

The centre of the structure at time zero is considered to be the origin of the coordinates on this plane. The axis system is redefined as follows: The positive direction on the y-axis is due North from the origin, the positive direction on the x-axis is due East from the origin and the positive direction on the z-axis is orientated to zenith. The axis system is shown in Figure 3.1.

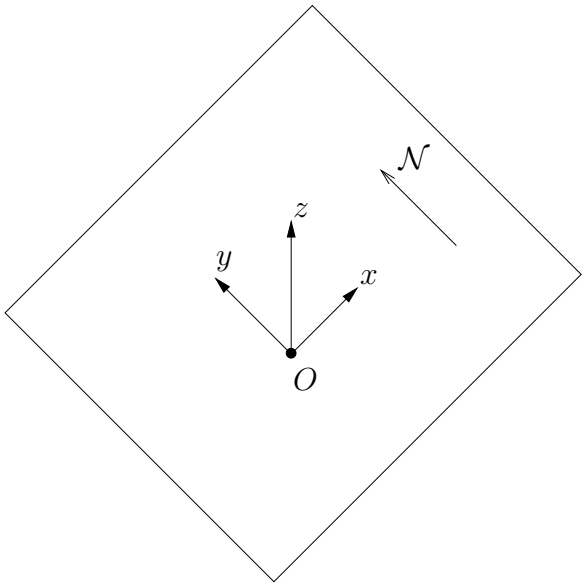

Figure 3.1: The coordinate system used in a plane in the rigid-body MATLAB simulator. O is the position of midships at time zero. Due North is located in the plane in the indicated direction.

Two further limitations of this simulator version are detailed here: The first is it can only calculate pitch and roll between a specified pair of receivers and the second is that all data is considered to be zero at time zero. The former was implemented into the simulator for simplicity at the early stages of development, whereas the latter is a representation of the practical case where no information is available prior to time zero.

3.2.1 Operation of the Simulator

The first step in the operation of the simulator is setting the conditions under which the simulations will be conducted. The user has the ability to set the wave conditions, as well as the drift and rotation of the structure. The user also has the ability to adjust the 95% confidence range of the GPS system itself, both in the horizontal and vertical directions. This allows the user to determine how much a degradation

or improvement in measurement quality might affect readings. The user also has the ability to position the receivers anywhere aboard the structure.

At each simulated timestep, the program first shifts the coordinates of the receivers to the exact position they would be located at if no errors were present. The next step is to introduce the errors on each receiver. Since it is desirable to simulate the worst case scenario, each receiver is treated independently by the simulator. The simulator will display plots of the error on each axis for each receiver.

In practice, many errors that affect GPS accuracy such as ionospheric delay, clock drift and ephemeris errors are highly coupled over a large area, hence treating the error on each individual measurement represents the worst case over a small area such as a ship. However, not all error sources are coupled, specifically multipath and internal receiver noise, as both error sources are independant for each individual receiver.

The error in the GPS system is implemented by randomly generating errors using the 95% confidence interval specified. Table 3.10 presented later in this chapter contains example of the standard deviation and mean position errors that could be expected.

The simulator generates two random normally distributed numbers per receiver, one to represent the magnitude of the horizontal error and the other to represent the magnitude of the vertical error. In addition, it generates for each receiver a single random number with a uniform distribution between 0 and 2π radians to represent the angle at which to apply the horizontal error. Once this is completed, the simulator simply adds the resulting error to the actual coordinates of the receivers.

At this point, since the coordinates of the individual receivers are known, it becomes a matter of simple trigonometry to calculate the angle between pairs, and the distances that separate the members of any given pair. Upon having obtained this information, a comparison between the true values and the simulated values is possible. Such results are shown in the following section.

3.2.2 Results from the Rigid-Body Simulator

In this section, results from a few simulator runs are considered. In all cases four receivers are used, and these were located at the coordinates shown in Table 3.1. In addition, in order to make valid comparisons between the simulations, the conditions shown in Table 3.2 were used during all simulations.

The key point to remember about the conditions presented in Table 3.2 is the fact that the “waves” are intended to provide the simulated vessel with motion

Receiver	**Coordinates** $(\mathbf{X}, \mathbf{Y}, \mathbf{Z})$ **[m]**
1	$(0, -10, 0)$
2	$(-3, 0, 0)$
3	$(3, 0, 0)$
4	$(0, 10, 0)$

Table 3.1: Coordinates of the four receivers used in the rigid-body simulations. The plane $z = 0$ is assumed to be the deck of the ship at time zero.

Condition	**Setting**
Duration of simulation	10 s
Simulation timestep	0.1 s
Drift along x-axis	1 m / s
Drift along y-axis	1 m / s
Rotational speed	5^o per second
Wave amplitude motion	1 m
Period of the pitching motion	10 s
Wave speed	1 m / s
Wave heading	20^o
Wave amplitude tolerance	0

Table 3.2: Conditions used in the rigid-body version simulations.

and were not intended to be a perfect representation of reality at sea. In effect, the motion of the waves is applied to the entire vessel. This may make the values in this table seem arbitrary, however they were chosen with the belief that they would represent conditions at sea with a certain degree of realism. The values shown in Table 3.1 make the ship in the simulator 20m long and 6m wide, basically a very small barge. Those shown in Table 3.2 would not be out of place in the Solent (waves) or in Southampton Water (current speed) where *Red Jet 4*, the ship used as a testbed sails. In fact, 1m waves are the limit under which *Red Jet 4* would sail.

The only variation between the simulations is the 95% confidence range for the GPS. The values used in the simulations are shown in Table 3.3.

Simulation	**Horizontal 95% Confidence Interval**	**Vertical 95% Confidence Interval**
1	1 cm	1 cm
2	2 mm	2 mm
3	25 cm	25 cm
4	1 m	1 m

Table 3.3: GPS confidence intervals used in the rigid-body version simulations.

Rigid-Body Simulation 1

In this simulation, centimetre accuracy was utilised. This is the level of accuracy obtained by Guo et al. in their study of the Humen bridge [21].

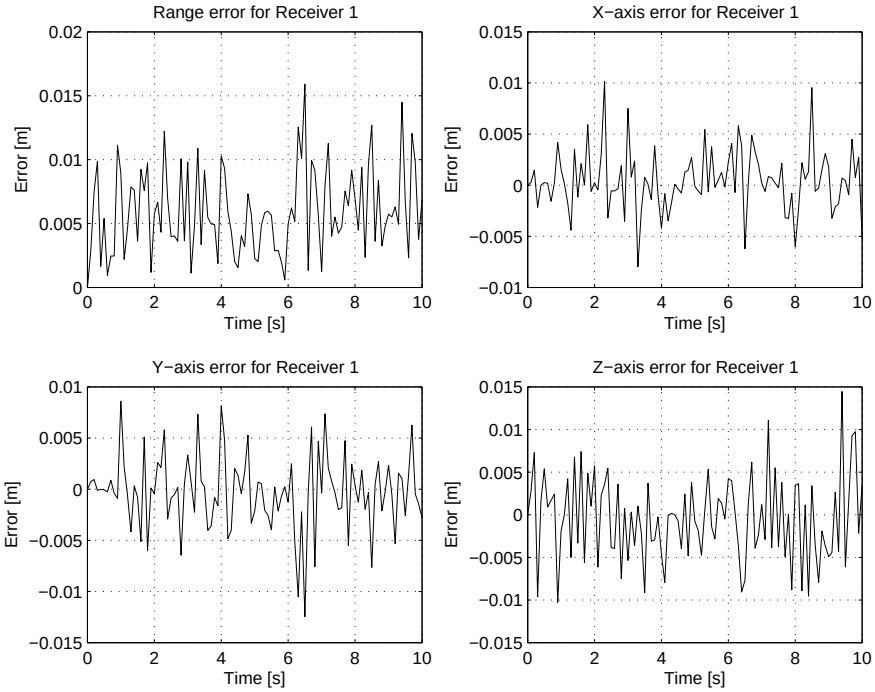

Figure 3.2: Error on each axis for receiver 1 for rigid-body Simulation 1.

The three figures included in this section reflect different information. The first, Figure 3.2, indicates the magnitude of the error due to the confidence interval of the GPS receiver itself. With centimetre level accuracy, it is clear that this error is quite small, as the largest range error obtained in simulation is approximately 2 cm. However, in the particular conditions associated with this project, that affirmation may not be accurate depending on the magnitude of the movement that is to be measured. Note that although only the information for receiver 1 is shown here, the simulator generates figures for all four receivers.

The second graph, Figure 3.3, shows some of the relationships that can be calculated between pairs of receivers. For the purpose of this simulator, the pitch of the structure is calculated by taking the angle between the plane and the vector linking receivers 4 and 1. In a similar fashion, the roll of the structure is calculate by taking the angle between the plane and the vector linking receivers 2 and 3. In this case, looking at the roll results, it is clear that the motion experienced by the vessel is strange as the ship seems to roll slowly and remain rolled. This is due to the way the waves are modelled to to interact with the ship. It is assumed the ship's pitch

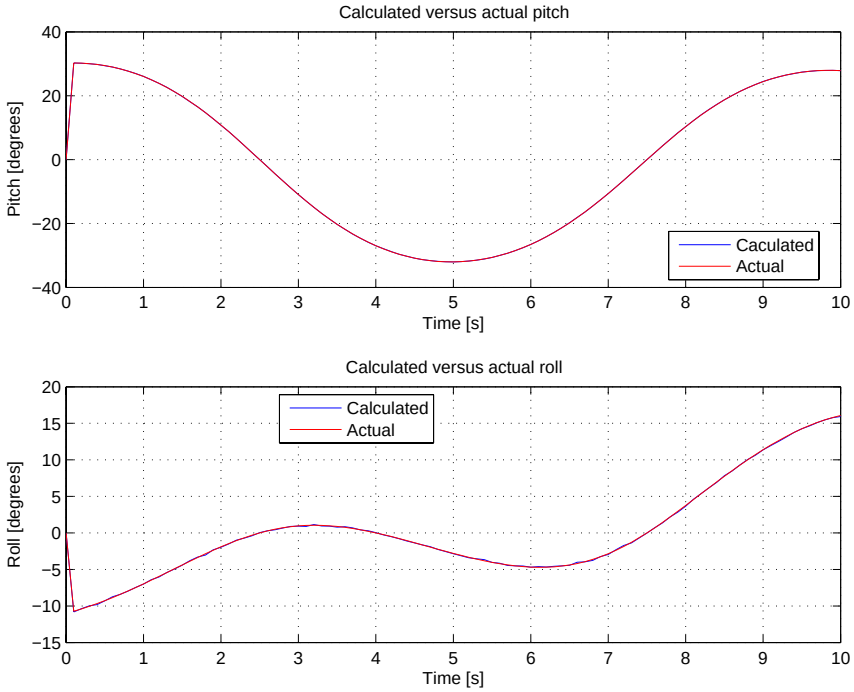

Figure 3.3: Calculated and actual values of pitch and roll plotted on the same graphs for rigid-body Simulation 1.

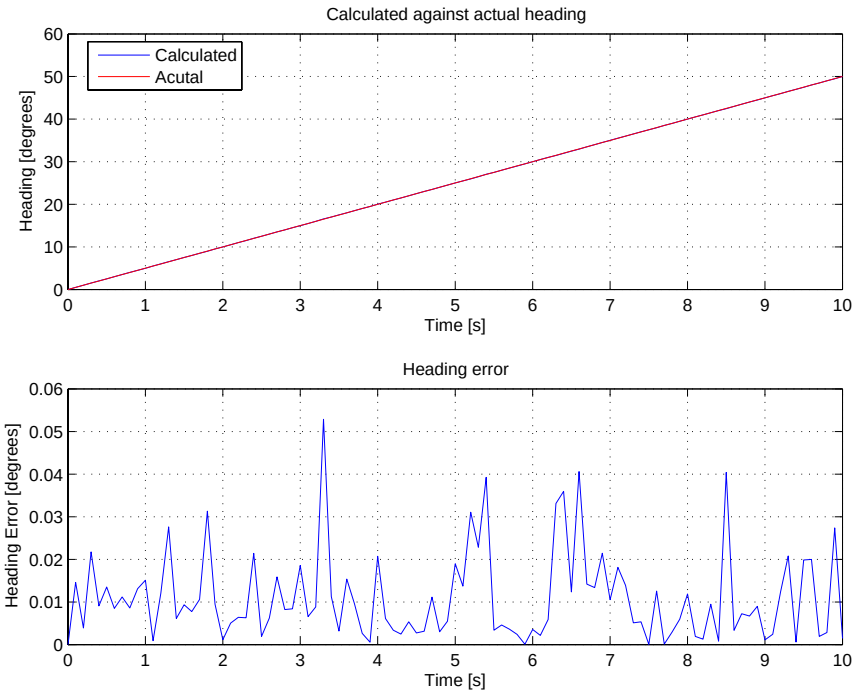

Figure 3.4: Calculated heading plotted and actual heading for rigid-body Simulation 1 on the same graph. The magnitude of the heading error is also shown.

and roll are functions of the gradiant of the wave at midships, a somewhat unrealistic assumption, which was done to the simplify the simulator. The fact that the ship drifts along the wave and rotates around midships compounds the effect by adding a trend to the roll motion itself. Should the rotation of the ship be removed, or the simulator run for a longer period of time, this trend would disappear and the roll effect would become a near-periodic function as expected. This is shown in Figure 3.5 where the duration of the simulator is increased to 72s, the time it takes the ship to complete a rotation about its axis.

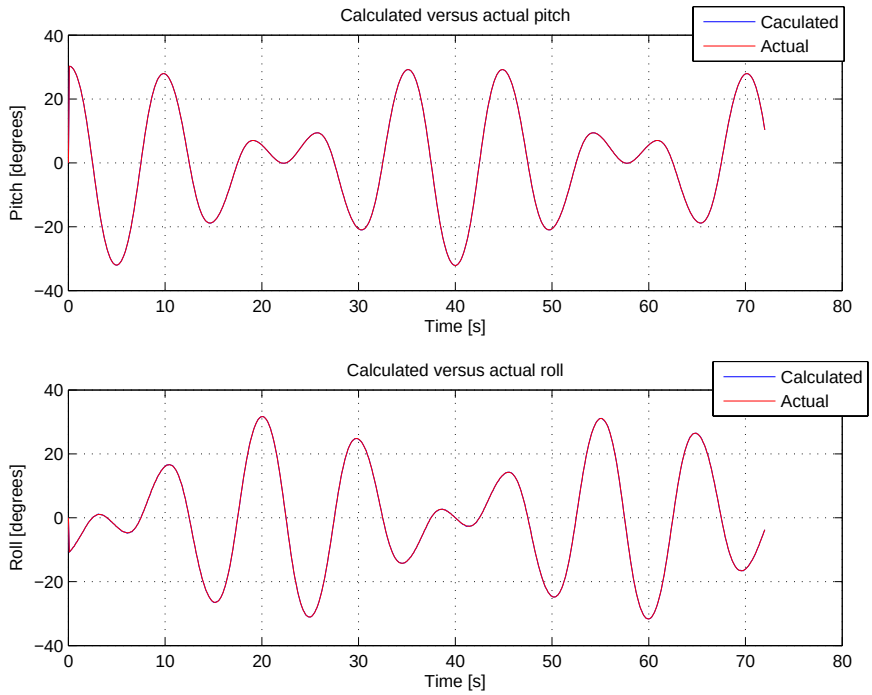

Figure 3.5: Pitch and roll graph for an extended duration simulation having the same characteristics as that shown in Figure 3.3.

Finally, the third graph, Figure 3.4, shows the calculated navigational heading of the structure against the actual heading. The magnitude of the error is explicitly plotted here as well.

The question that remains is as to whether or not this accuracy level is acheivable on a ship. Petovello et al. [46] managed to acheive a standard deviation of between 1cm and 2cm in their studies, but that this level of accuracy is highly dependant on the sea state. Their achieved accuracy level is therefore only slightly lower than the one used for this simulation. It is therefore not unreasonable to suggest that this level of accuracy may be achievable.

Rigid-Body Simulation 2

In this simulation, millimetre accuracy is utilised and the equivalent graphs (see Figure 3.6, Figure 3.7 and Figure 3.8) are shown for the sake of comparison with the first simulation. The accuracy selected here represents approximately 1% error on the carrier-phase data only and neglects other error sources. This level of accuracy is theoretically achievable, but in practice, there are as of yet no known cases where it has been acheived.

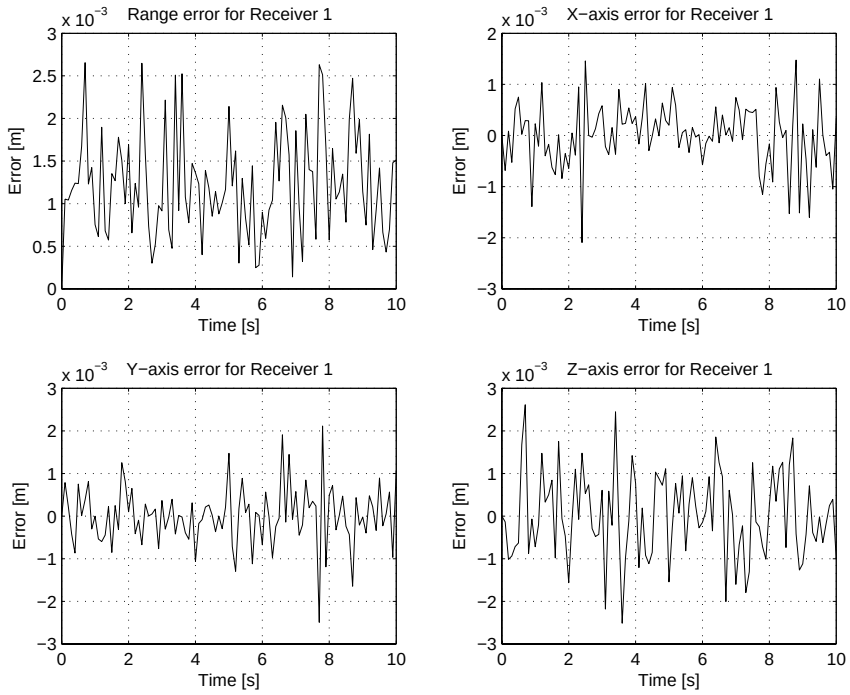

Figure 3.6: Error on each axis for receiver 1 for rigid-body Simulation 2.

Rigid-Body Simulation 3

In Simulation 3, the accuracy of the GPS receivers was degraded quite significantly from that of the previous two simulations (95% confidence interval of 25 cm in both directions). Once again, the equivalent three graphs are repeated for the sake of comparison (see Figure 3.9, Figure 3.10 and Figure 3.11).

In Figure 3.10, there is a substantial difference between the magnitude of the error on the calculated pitch and that of the calculated roll. This is due to the fact that the baseline between the receivers used to calculate pitch is longer than the one between those used to calculate roll. In Figure 3.7 and Figure 3.3, the same applies,

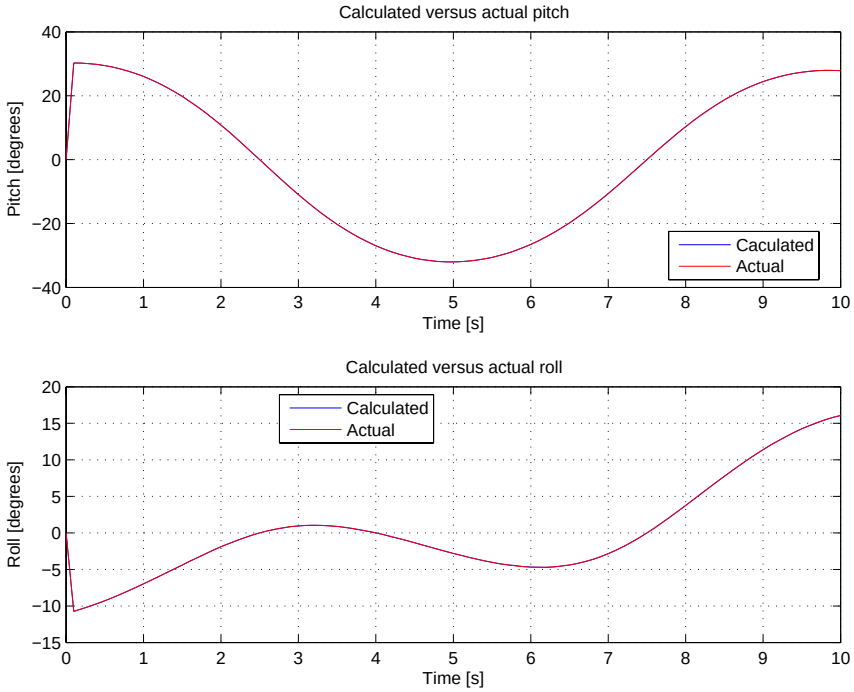

Figure 3.7: Calculated and actual values of pitch and roll plotted on the same graphs for rigid-body Simulation 2.

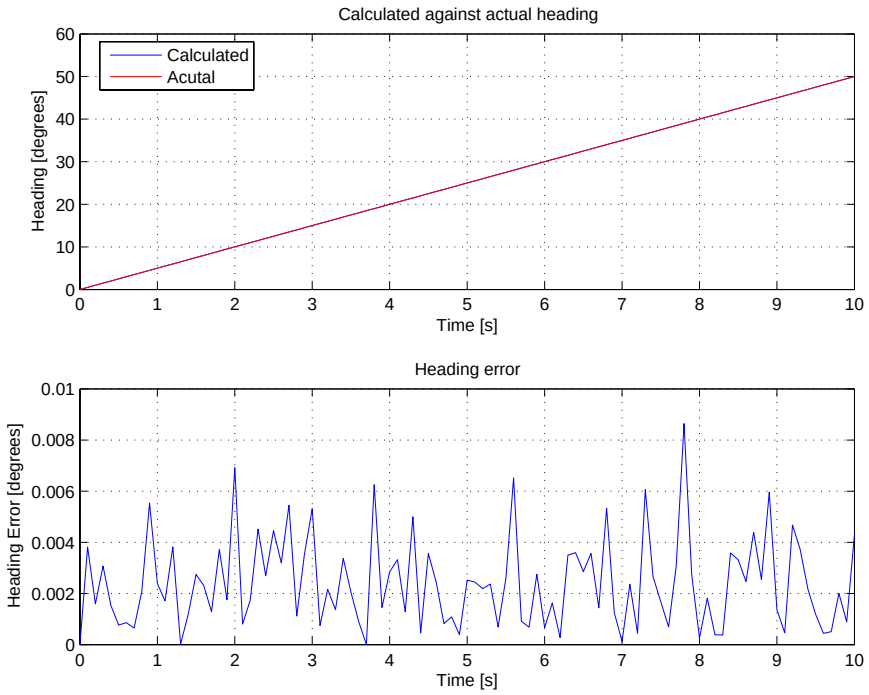

Figure 3.8: Calculated heading and actual heading plotted on the same graph for rigid-body Simulation 2. The magnitude of the heading error is also shown.

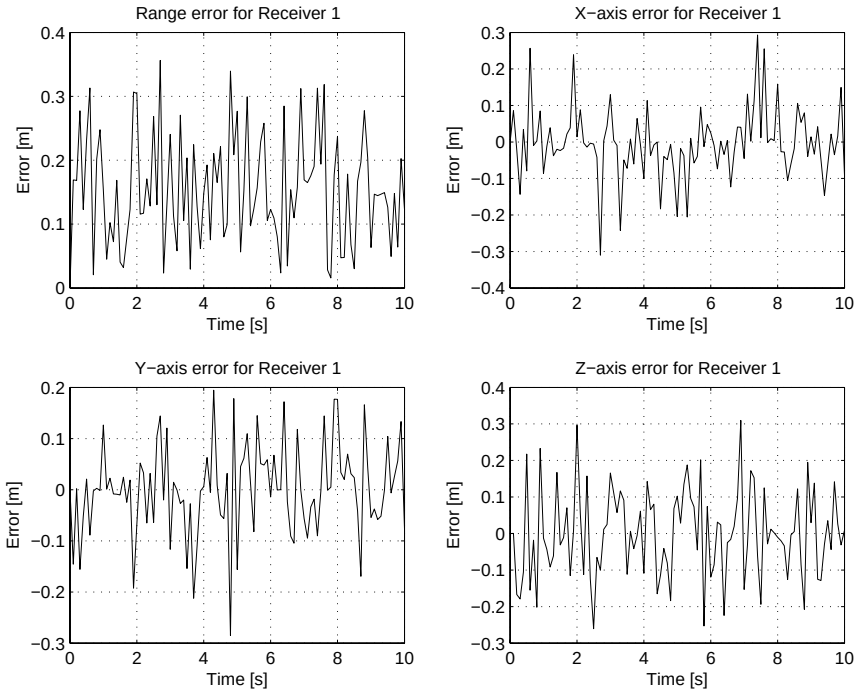

Figure 3.9: Error on each axis for receiver 1 for rigid-body Simulation 3.

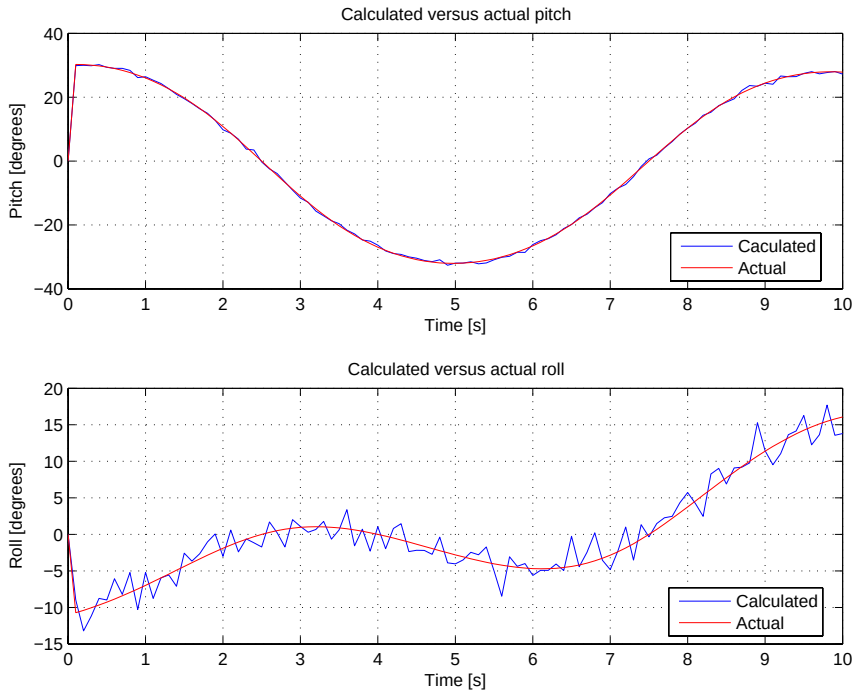

Figure 3.10: Calculated and actual values of pitch and roll plotted on the same graphs for rigid-body Simulation 3.

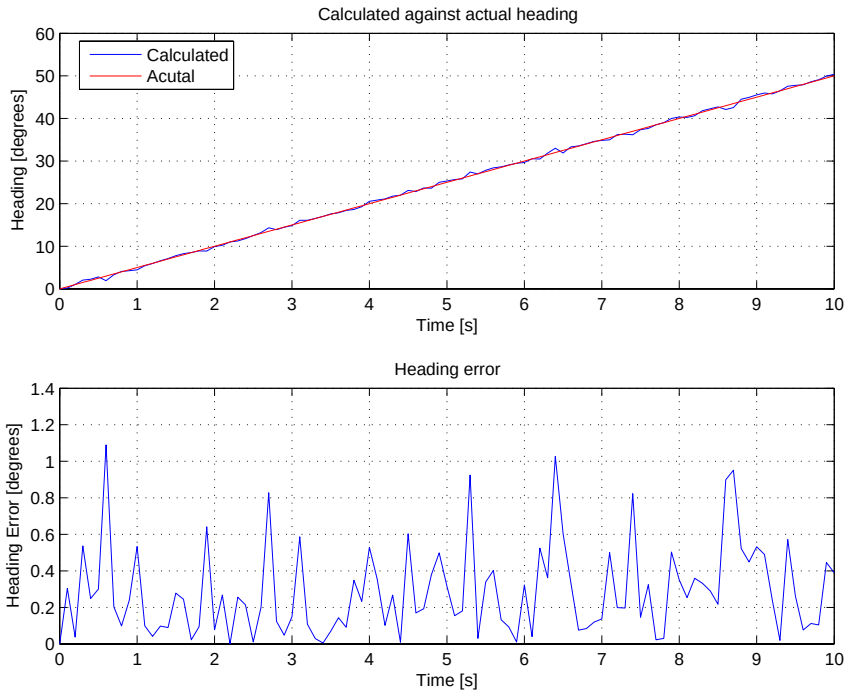

Figure 3.11: Calculated heading and actual heading plotted on the same graphs for rigid-body Simulation 3. The magnitude of the heading error is also shown.

however the magnitude of the error on position fix is so small that the difference is hardly visible.

It is clear that the larger confidence interval would cause serious problems in the determination of small movements. Since under the project conditions the errors may be several orders of magnitude higher than the distortions that are to be measured, the use of other techniques to measure distortion may be more appropriate.

Rigid-Body Simulation 4

In this simulation, the performance of the GPS receivers is seriously degraded (95% confidence intervals of 1 m on each direction). Under similar, or worse, conditions, the objectives of the project are unrealisable as shown by the following figures (see Figure 3.12, Figure 3.13 and Figure 3.14). This error figure is similar to the worse-case error figures of the G12 receiver which was used in practical work.

In Figure 3.14, what appears to be a very large heading error appears in the top portion of the figure. However, this is not the case as the heading error is less than 10 degrees. The spike is due to the fact that the heading is calculated as being approximately 355 degrees instead of approximately 5 degrees. This is confirmed

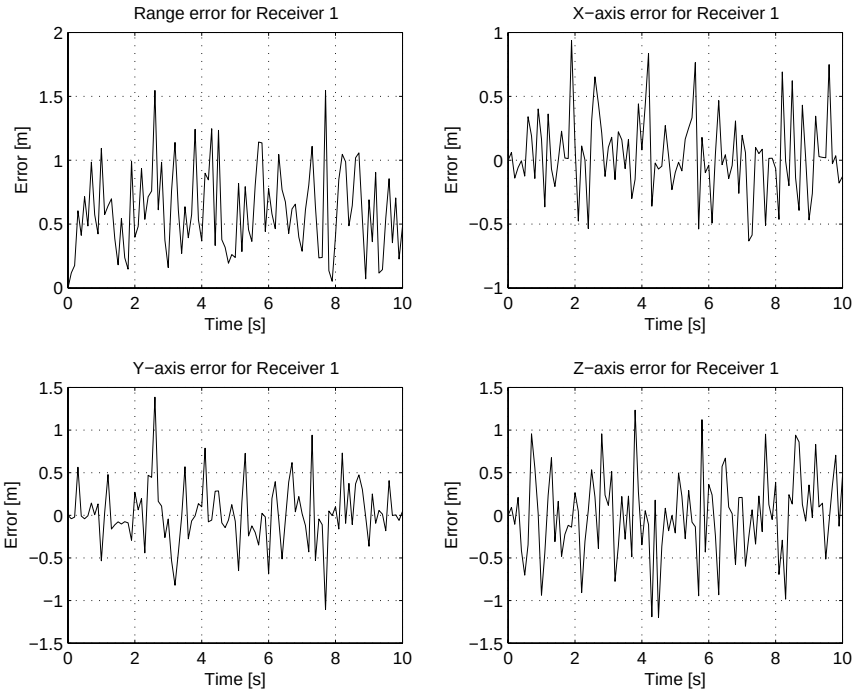

Figure 3.12: Error on each axis for receiver 1 for rigid-body Simulation 4.

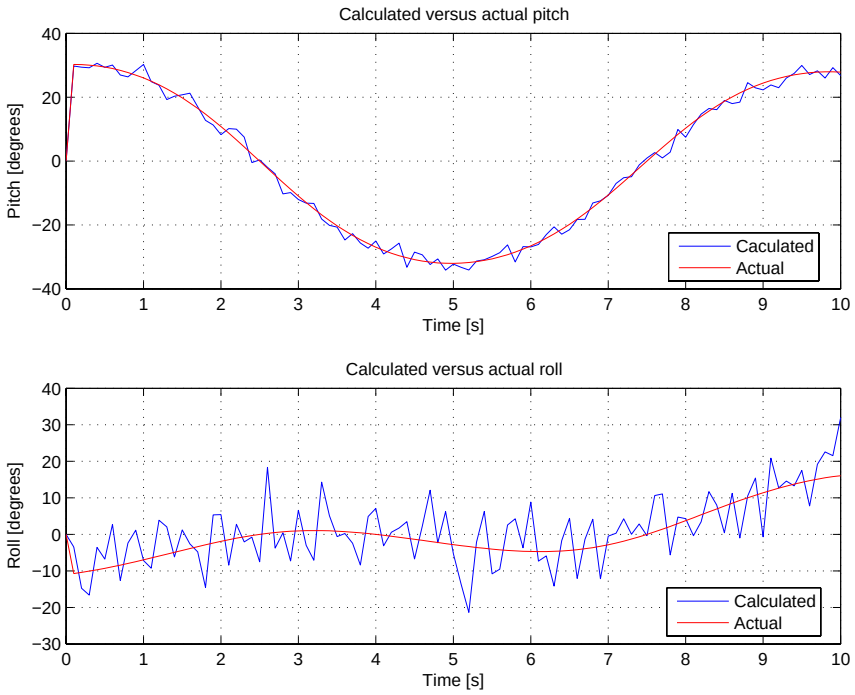

Figure 3.13: Calculated and actual values of pitch and roll plotted against each other for rigid-body Simulation 4.

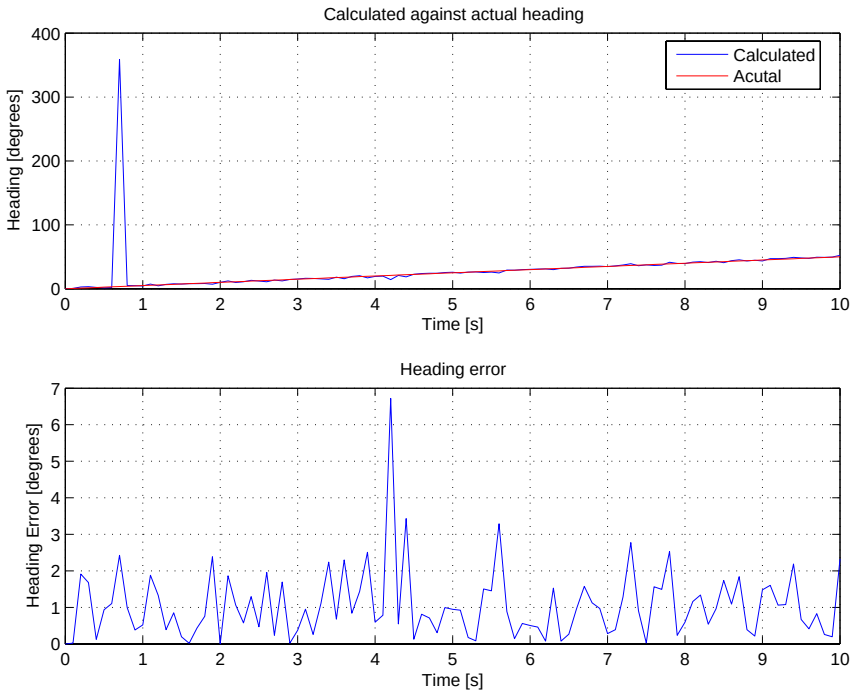

Figure 3.14: Calculated heading plotted against actual heading for rigid-body Simulation 4. The magnitude of the heading error is also shown.

by the magnitude of error in heading graph.

3.2.3 Conclusions from the Rigid-Body MATLAB Simulator

Although the rigid-body MATLAB simulator assumed it was dealing with a fully rigid structure, and thus did not measure structural deformation *per se*, some conclusions can be drawn. The calculation of pitch and roll utilise differential positioning, the same technique that would be used to calculate structural deformation. The difference lies in the magnitude of the movements of the relative positions.

It is clear that a change in the accuracy of the available receivers has a major impact in the accuracy of the calculation of pitch and roll. Thus, at this point in the project, it was determined that a major component of the research was to relate the accuracy required to the accuracy obtained. It was believed that the obtention of this piece of information would be of major importance in validating this project.

3.3 Modelling a Vessel's Flexible-Body Motion

"Any structure with mass and elasticity will possess one or more natural frequencies of vibration." [12] A vessel, clearly fits this definition. Based on Newton's

third law of mechanics, if a structure is excited, it will produce a reaction which is a function of the energy, and frequency, with which it is excited. Other factors, such as load distribution, can influence the response. However, for simplicity of the discussion, it is assumed that the vessel to be modelled is a uniform structure, meaning that the mass of the vessel is uniformely distributed along its length.

In addition, to further simplify the model, it is also assumed that the ship can be modelled as a single-span beam, with both ends of the beam being unconstrained. The latter part is a reasonable assumption as the bow and stern of vessels are not physically constrained. It is also suggested in Hirdaris et al. [25] that beam theory is applicable to vessels.

3.3.1 Bending Mode for a Linear Beam

Given the assumption that a ship can be modelled as a linear beam [25], it is now necessary to determine the natural frequency for each mode, and the shape of each mode. By definition, the n-th bending mode indicates the condition in which the structure is reacting to excitation with n half-waves along its length. Figure 3.15 shows a beam bending in modes 1, 2 and 3 respectively given that each subfigure has 1, 2 and 3 half-waves along the beam's length.

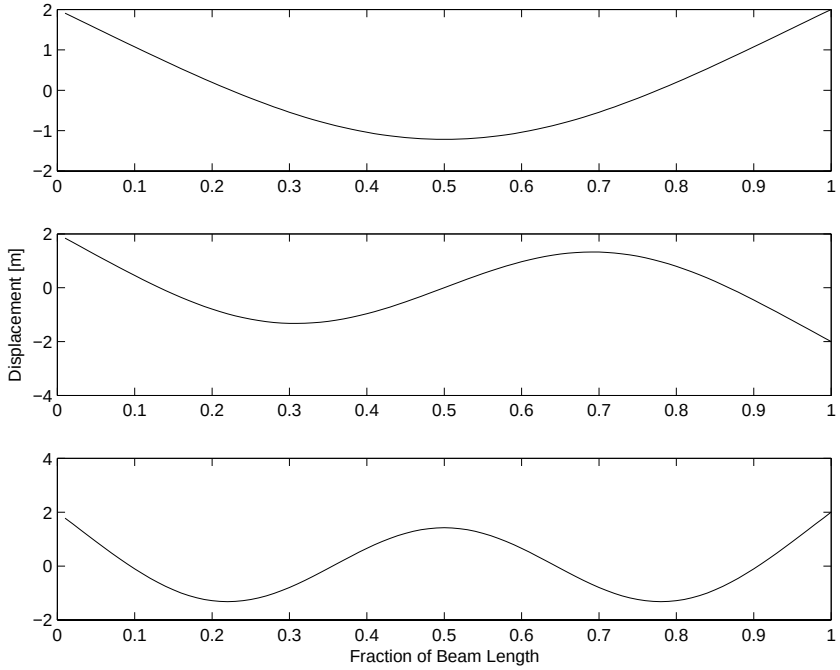

Figure 3.15: A free-free beam bending in modes 1, 2 and 3.

For each mode, it is possible to calculate its natural frequency. Blevins [12]

provides the following formulae and tables to accomplish this:

$$f_i = \frac{\lambda_i^2}{2\pi L^2}\sqrt{\left(\frac{EI}{m}\right)} \tag{3.1}$$

where f_i is the natural frequency for mode i, λ_i the value shown in Table 3.4 for mode i, L the span of the beam, E the modulus of elasticity for the material, I the moment of inertia and m the mass per unit of length.

i	$\lambda_\mathbf{i}$
1	4.73004074
2	7.85320462
3	10.9956078
4	14.1371655
5	17.2787597
$i > 5$	$(2i+1)\frac{\pi}{2}$

Table 3.4: Value for λ_i for Equation (3.1).

In Table 3.4, λ is a dimensionless real parameter which depends on the boundary conditions. The value in the table above, given in Blevins' textbook, are for a beam with no deflections initially.

Knowing the natural frequencies of the beam's modes, it is then possible to determine the normalised deflection of the beam at any point in time for any mode using the following formula [12]:

$$\chi_i(\ell) = \cosh\frac{\lambda_i \ell}{L} + \cos\frac{\lambda_i \ell}{L} - \sigma_i\left(\sinh\frac{\lambda_i \ell}{L} + \sin\frac{\lambda_i \ell}{L}\right) \tag{3.2}$$

where $\chi_i(\ell)$ is the normalised deflection of the beam at point ℓ for mode i (see Figure 3.16 for how ℓ is determined), σ_i the value shown in Table 3.5.

i	$\sigma_\mathbf{i}$
1	0.982502215
2	1.000777312
3	0.999966450
4	1.000001450
5	0.999999937
$i > 5$	≈ 1.0

Table 3.5: Value for σ_i for Equation (3.2).

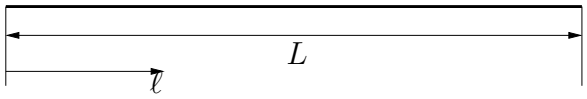

Figure 3.16: Diagram showing beam dimensions and value of ℓ.

A few assumptions were made. First is the shape of the beam used to model the ship. In order to better model a vessel, a pipe with inner-radius a and outer radius b was chosen, as shown in Figure 3.17. The moment of area can easily be calculated

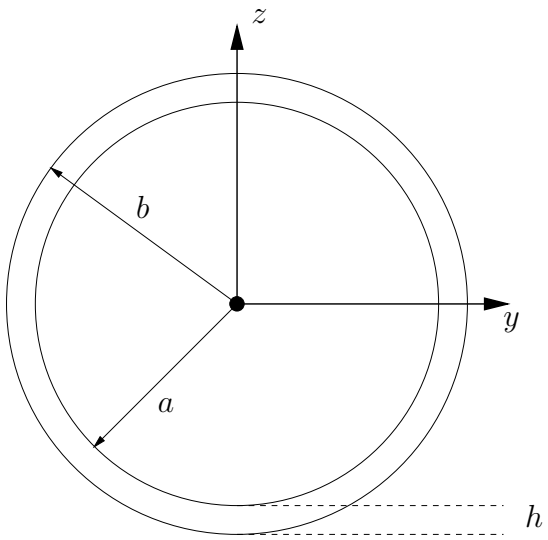

Figure 3.17: Diagram showing a cross-section of the pipe used to calculate I_{xx}.

with the following area integral where A is the area over which the integral is performed:

$$I_{xx} = \int_A \int y^2 \, \mathrm{d}A \tag{3.3}$$

Integrating over the cross-section of the pipe will yield the following result [12]:

$$I_{xx} = \frac{\pi}{4}(b^4 - a^4) \tag{3.4}$$

Second is the material of which the beam consists. Clearly, a ship is not a homogeneous structure as a variety of materials can be found within it. However, for simplicity, it is assumed that the beam is a homogeneous beam of 0.4%C Steel as described in [14]. Thus, we find that for this particular material, the modulus of elasticity is $E = 210 \text{ GN} / \text{m}^2$.

3.3.2 Modelling Multiple Modes Simultaneously

Depending on the excitation provided to the ship, it is possible that more than one mode will be active at any one time. In such cases, the superposition principle can be applied. Thus, deflection for the beam can be calculated as such:

$$\chi(\ell) = \sum_{i=1}^{n} a_i \chi_i(\ell) \tag{3.5}$$

where $\chi(\ell)$ is the actual deflection of the beam at point ℓ, a_i the maximum amplitude of mode i and n the number of the highest mode seen on the beam.

3.3.3 Rigid Body Motion

The simulation of rigid body movement is a straight-forward process. It is only necessary to superimpose it onto the beam deflection. In order to simplify the current model, the only forms of rigid-body motion that were considered were pitch and roll of the ship. Consider the value of pitch, calculated in radians, and represented by α, is modelled using the following equation:

$$\alpha(t) = \frac{\pi \alpha_{max} \sin\left(\frac{2\pi t}{T}\right)}{180} \tag{3.6}$$

where α_{max} is the maximal pitch angle (in degrees) and T the period of the pitching movement.

The presence of pitch requires movement to be considered along two-axes as shown in Figure 3.18 to account for the components of the deflection along different axes. This can be seen in the figure by the two dots on the straight and deflected bar, which are the same point on the bar's length axis.

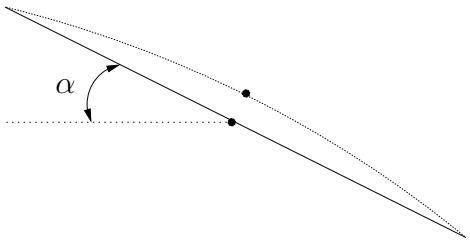

Figure 3.18: A pitched bar with mode 1 distortions.

3.4 Results from the Flexible-Body Simulator

In this section, the results from the flexible-body simulator are presented. The modelling technique utilised is that which was described in Section 3.3. Three simulation runs are presented in detail here. Analysis of the results is presented in a later section.

3.4.1 Simulation Run 1 — Medium Accuracy

In this section, results from a run where the GPS accuracy is slightly better than what can be achieved with a C/A code GPS receiver as these usually are accurate only to a few metres. However, this level of accuracy is lower than what was acheived using networks of carrier-phase receivers as discussed previously. The exact parameters for the simulation run are provided in Table 3.6. In this simulation the accuracy numbers chosen were close to the theoretical performance of the G12 receiver, as evidenced in the datasheet and manual for the board [31]. The receivers are evenly separated along the principle axis of the pipe as shown in Figure 3.19.

Parameter	Value
GPS 95% Vertical Confidence Bound [m]	0.5
GPS 95% Horizontal Confidence Bound [m]	0.3
Length of pipe [m]	200
Inner Radius of pipe [m]	19.99
Outer Radius of pipe [m]	20.00
Maximum Pitch [degrees]	5
Pitch Period [s]	10
Number of Receivers	5

Table 3.6: Parameters for flexible-body simulation run 1.

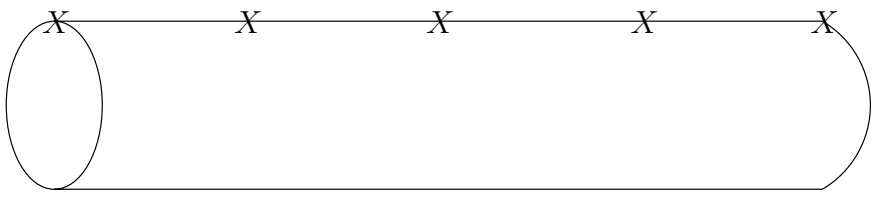

Figure 3.19: Position of the GPS receivers for the flexible-body simulator. Receivers are located at the positions marked by an X.

Figure 3.20 shows the bending ship, in blue, and the calculated position, in red,

of the GPS receivers at four different timesteps, each evenly spaced out over the course of the simulation.

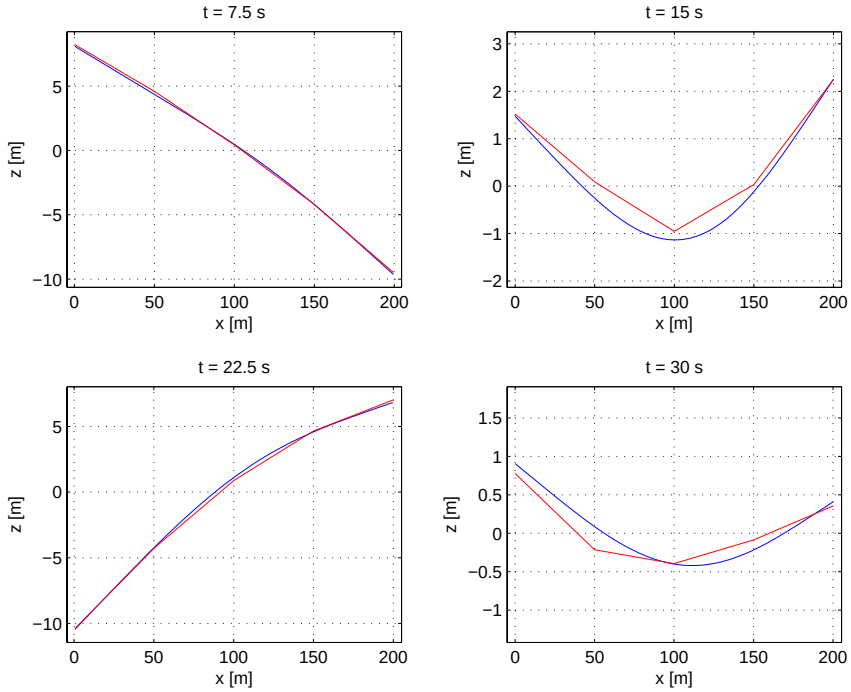

Figure 3.20: Bending ship and calculated position for flexible-body run 1.

As can be seen from Figure 3.20, the bending and pitching movements of the ship are followed by the receivers. However, some errors of up to 0.25m can be observed at some points in this figure. Tracking accuracy of pitch is shown in Figure 3.21.

The simulator was also capable of extracting errors for individual receivers. Figure 3.22 shows such a graph. Although there were five receivers onboard the vessel during the course of the simulation, only the graph for the 3rd receiver, located at mid-ships is shown. The simulator does however extract this graph for all the receivers onboard.

3.4.2 Simulation Run 2 — Degraded Performance

In this run, the simulator was configured to account for an extremely degraded GPS performance, and one under which the project objectives would be completely unrealisable. Most of the parameters from run 1, which were shown in Table 3.6, remain the same. Thus, Table 3.7 only shows the parameters which have been varied.

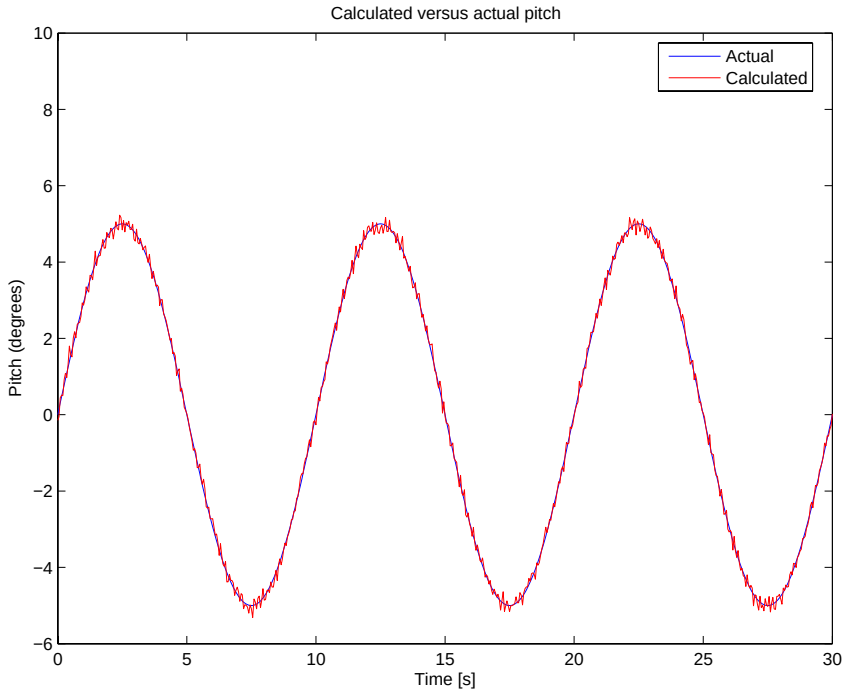

Figure 3.21: Pitch movement tracking for flexible-body run 1.

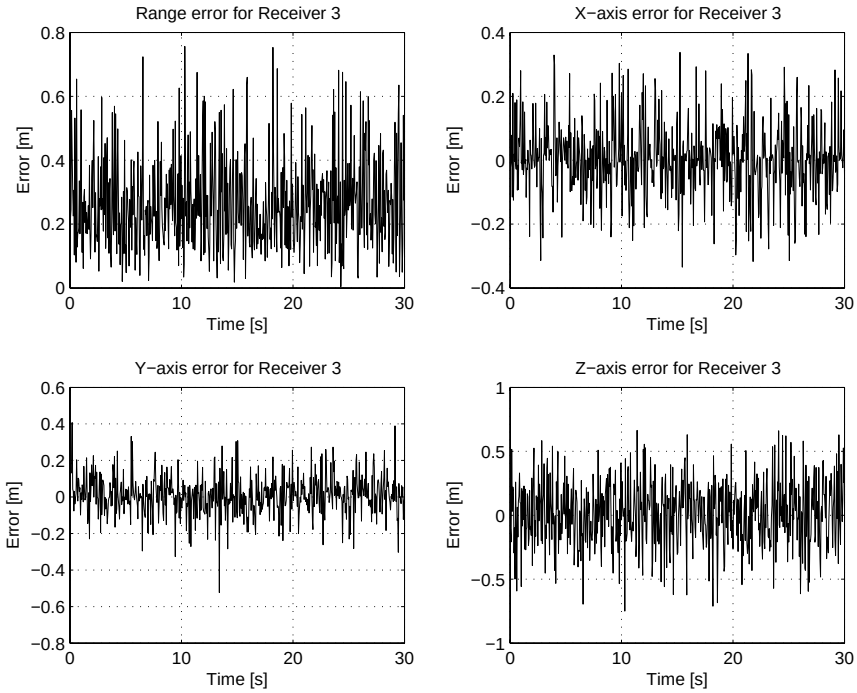

Figure 3.22: Range errors for the mid-ships receiver for flexible-body run 1.

Parameter	Value
GPS 95% Vertical Confidence Bound [m]	2
GPS 95% Horizontal Confidence Bound [m]	1

Table 3.7: Changed parameters for flexible-body simulation run 2.

Considering the graphs in the same order as in the previous section, it is possible to notice a severe degradation in the tracking ability for the bending movement. This is shown in Figure 3.23.

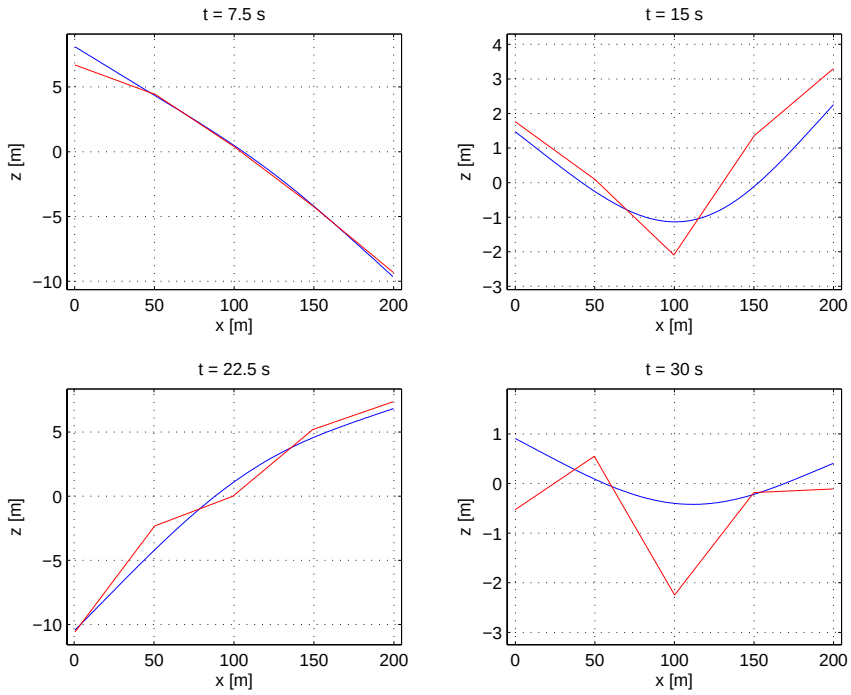

Figure 3.23: Tracking of bending movement during flexible-body simulation run 2.

From this, it would be expected that the results of the pitch tracking would also be degraded. This is indeed the case, however, the degradation is not as serious as could be expected as shown in Figure 3.24.

Finally, Figure 3.25 shows the range errors for the midships receiver.

3.4.3 Simulation Run 3 — High Accuracy

In this section, results are presented from a run in which the accuracy of the GPS reaches the centimetre scale. As with the previous run, the simulator parameters are mostly unchanged. Table 3.8 shows the changed parameters. Here, the accuracy level is only slightly higher than from the Petovello et al. paper [46] so it is

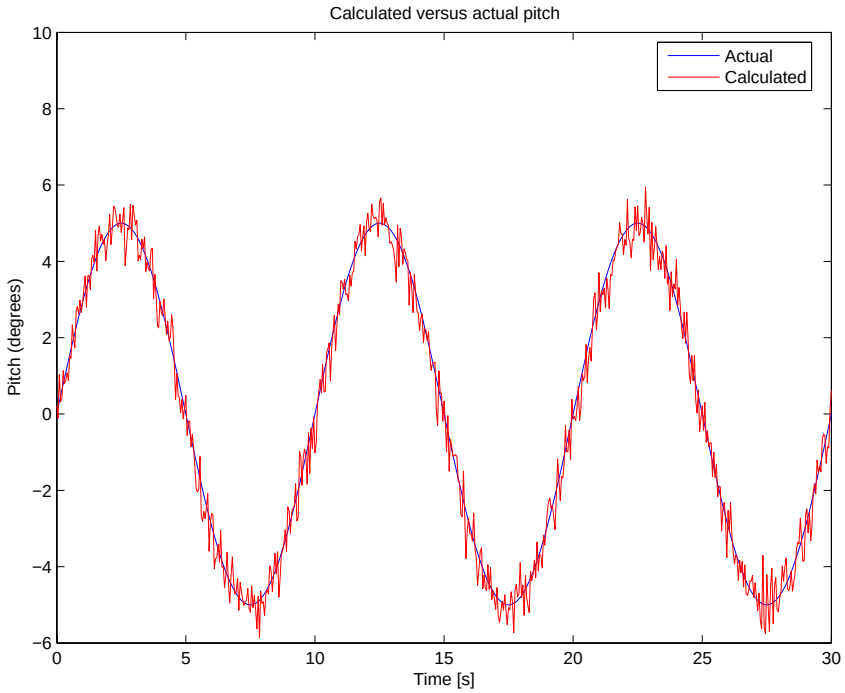

Figure 3.24: Pitch movement tracking for flexible-body simulation run 2.

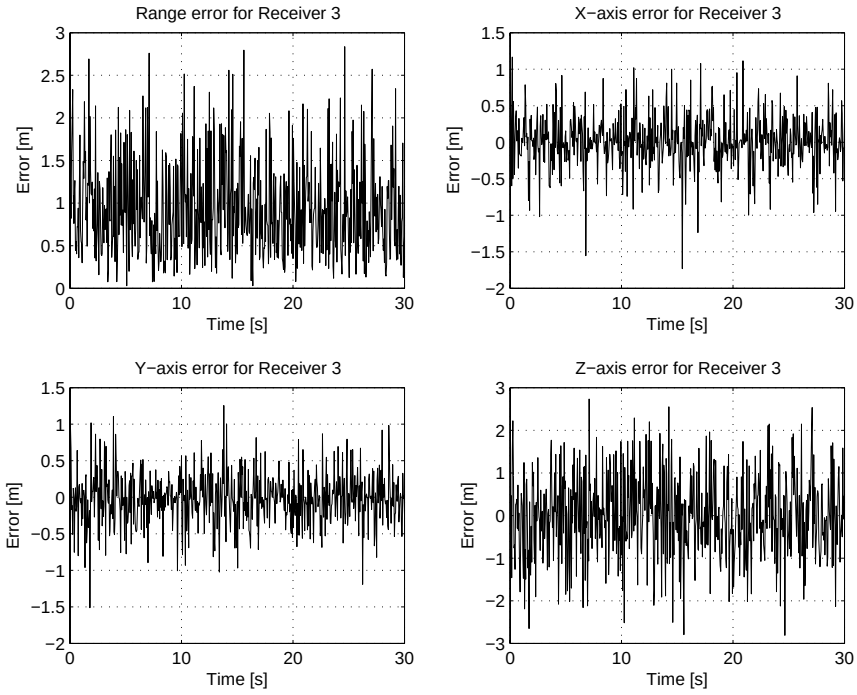

Figure 3.25: Range errors for the mid-ships receiver for flexible-body simulation run 2.

possible that this accuracy could be achieved with proper equipment.

Parameter	Value
GPS 95% Vertical Confidence Bound [m]	0.01
GPS 95% Horizontal Confidence Bound [m]	0.01

Table 3.8: Changed parameters for flexible-body simulation run 3.

Once again, the graphs are considered in the same order as the previous two sections. The first of these, Figure 3.26 shows a marked improvement over the tracking ability of the receivers.

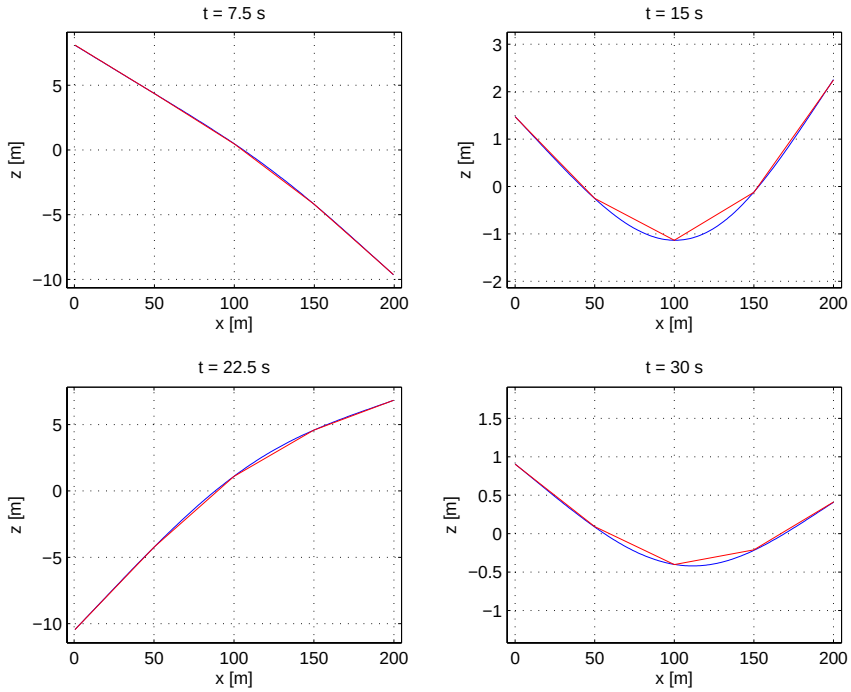

Figure 3.26: Tracking of bending movement during flexible-body simulation run 3.

This is further confirmed by the second of the graphs, Figure 3.27 which illustrates the pitch calculations.

Finally, the range errors are shown in Figure 3.28.

3.5 Analysis of Results

In this section, the results detailed in the previous section are analysed. This analysis will draw attention to the baseline length and the impact of the number of receiver networks. Following the visual analysis, a particular attention is paid to fre-

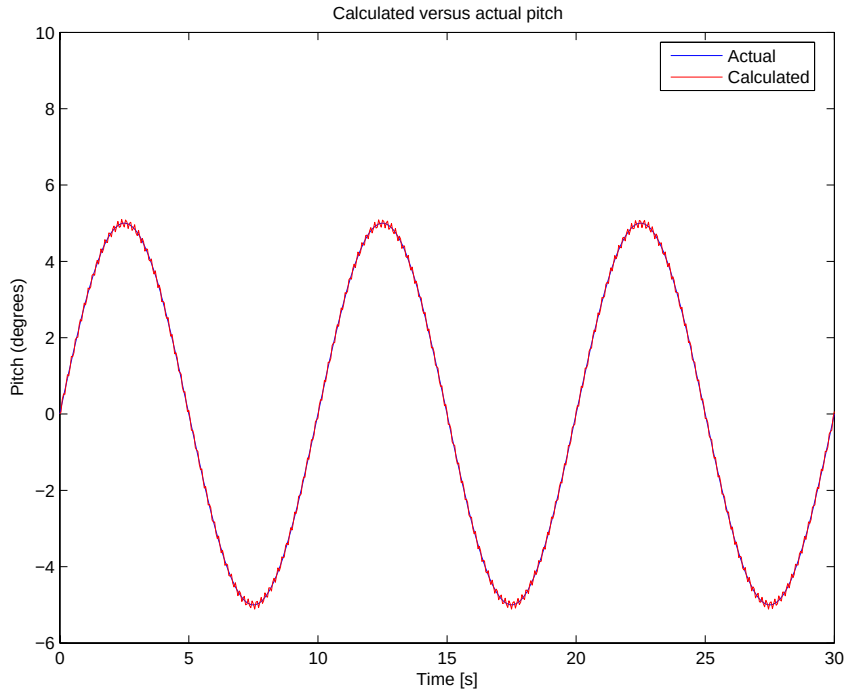

Figure 3.27: Pitch movement tracking for flexible-body simulation run 3.

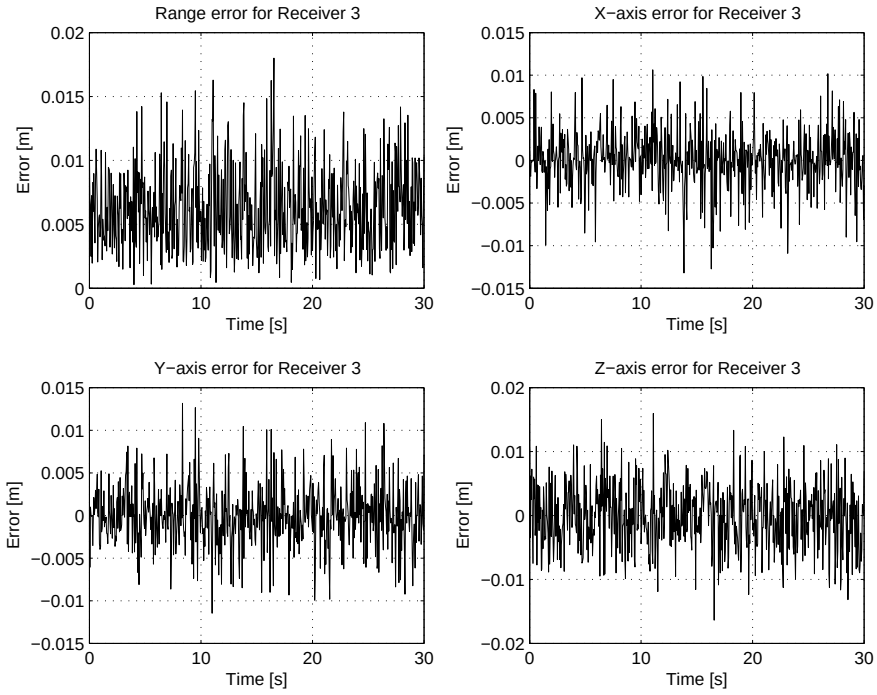

Figure 3.28: Range errors for the mid-ships receiver for flexible-body simulation run 3.

quency analysis of the receiver motions. The use of frequency analysis allows the separation of various motions of the receivers into their indvidual components. It will also allow for further discussion regarding placement of the receiver network.

3.5.1 Visual and Mathematical Analysis

In this section, visual analysis of the graphs from the previous section is made. For each simulation run, three graphs were shown. Each of these graphs is dealt with in the same order here.

The first result that was shown was a sequence of four graphs, each of them representing the state of the simulator at a regular interval during the run. In each of them, the blue line is the actual position of the ship (which accounts for bending mode and pitch), whereas the red line is the position the GPS receivers perceive the ship to be at. Clearly, and as expected, the first and third runs provide the better results as they follow the actual movement of the ship. This is due to the setup of the simulator which provided for better accuracies for those two runs. The second run seems to indicate the impact of severe degradation. During this run, point errors can be in the order of a metre or more.

To determine the range error of each receiver, it is necessary to consider the second range of graphs. In these, the positioning error on each axis, as well as the total positioning error is indicated. A single simulation using each of the three error settings was run and the error data for each one of these simulations are summarised in Table 3.9.

Data	**Simulation 1** Medium Accuracy	**Simulation 2** Low Accuracy	**Simulation 3** High Accuracy
Mean total position error [m]	0.2568	0.9263	0.0064
Standard Deviation [m]	0.1386	0.5479	0.0033
Maximal position error [m]	0.9621	3.1513	0.0223
Minimal position error [m]	0.0122	0.0439	1×10^{-4}

Table 3.9: Summary of range errors on mid-ships receiver for each simulator run

In order to confirm the statistical validity of the simulation runs, data from the error function was generated two hundred thousand times for each of the error settings. The results are shown in Table 3.10 and seem to confirm the validity of the simulator error results as they are similar to that of those shown in Table 3.9.

As expected, the results from the first and third runs are the superior results. However, it is important to point out that these errors are uncorrelated. In practice,

Data	Simulation 1	Simulation 2	Simulation 3
Mean total position error [m]	0.2544	0.9648	0.0063
Standard Deviation [m]	0.1416	0.5614	0.0033
Maximal position error [m]	1.1919	5.0327	0.0264
Minimal position error [m]	4.6×10^{-4}	0.0022	1.0×10^{-5}

Table 3.10: Analysis of the error function using simulator settings

mane elements of GPS positioning errors are highly correlated over a small area (such as that of a ship). These correlated elements include satellite clock biases, ephemeris errors and ionospheric delays. As such, DGPS observables would have cancelled out many of them and, therefore, many of the errors in the table above would be smaller. This simulation uses worst case analysis in order to simplify the analysis.

The third type of graph was the pitch tracking graph. Similarly to the analysis performed on the positioning error, Table 3.11 provides a summary of the errors on pitch. Again, as expected, the results from runs 1 and 3 are superior. However,

Data	Simulation 1	Simulation 2	Simulation 3
Mean pitch error [rads]	0.0019	0.0056	0.0013
Standard Deviation [rads]	0.0013	0.0043	6×10^{-4}
Maximal pitch error [rads]	0.0071	0.0261	0.0021
Minimal pitch error [rads]	1×10^{-5}	6×10^{-7}	1×10^{-6}

Table 3.11: Summary of pitch tracking errors for each simulator run

at first glance, it would seem that pitch is not as heavily affected by a degradation of the GPS performance as positioning error. This is due to the 200m length of the ship that is being simulated. Assuming that both receivers are in error by 1 metre on the vertical axis only, the resulting error is approximately equal to 0.01 rads. For shorter vessels, a small error in receiver positioning would lead to a large error in pitch tracking.

The addition of more receivers would possibly allow the simulator to better approximate the form of the ship, even distorted. A graph with such results is shown in Figure 3.29. The simulator was configured with the same conditions as the first run described above (see Table 3.6), with the difference that for this run, receivers were placed at intervals of 25 metres along the ships principal axis. It would be expected that this would lead to a better following of the ship's shape due to the increased number of receivers, but as can be seen from two of the snapshots, this is not the case due to the fact a "worst-case" analysis is being conducted. Under

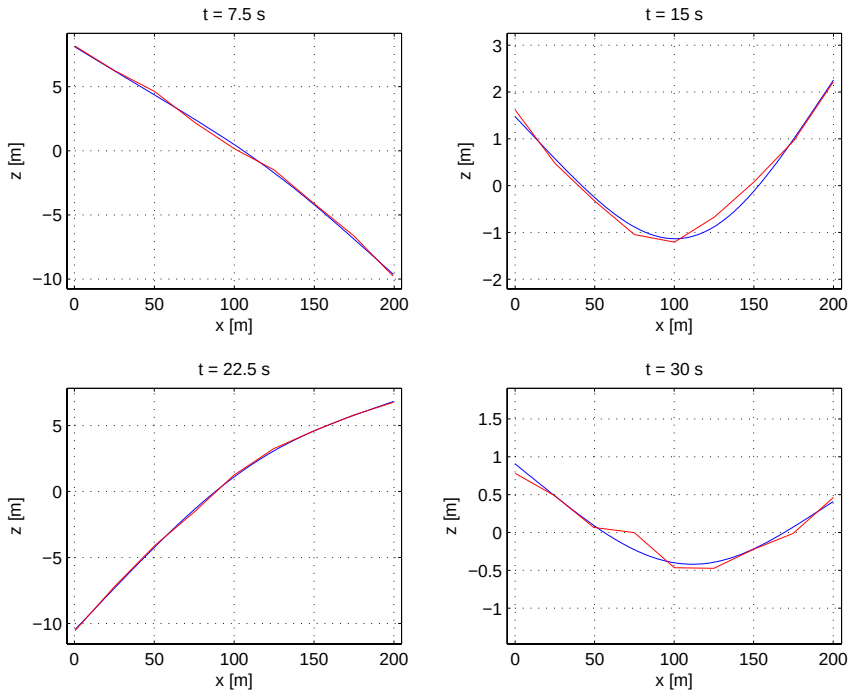

Figure 3.29: Regular interval snapshot of simulator status with extra receivers.

the conditions from the third run, the ship's form would be closely followed and more accurate with additional receivers.

This led to the questions as to whether or not it is possible to identify seperate ship motions (pitch, roll, flexible body, etc.) by using the time-domain results, and, whether or not the position of the receivers has an importance for this analysis. The first question is difficult to answer, but a degraded performance would seem to preclude time-domain analysis. The second question is easily answered using frequency-analysis.

3.5.2 Frequency Analysis

In this section, a brief explanation of the main tool for use in frequency analysis, the Fourier transform, is provided. The information detailed here is mostly a synthesis from [45, 47, 48]. Other references are cited as needed.

Fourier Transform

Just as it is possible to split white light into its individual components by use of a prism, it is possible to isolate the different frequency components of a particular signal (or system) by use of the Fourier transform. There are two possible cases,

for a periodic signal, and for an aperiodic signal. Due to the presence of noise in the receiver position signals, the resulting signal can be considered aperiodic.

A continuous aperiodic signal, $x(t)$, can be looked upon as a periodic signal having an infinite length period. Let $x_p(t)$ be a periodic signal with period T_p. In limit form this equates to:

$$x(t) = \lim_{T_p \to \infty} x_p(t) \tag{3.7}$$

Any periodic function $x_p(t)$ can be written in the form of a Fourier series as such:

$$x_p(t) = \sum_{k=-\infty}^{\infty} c_k e^{j2\pi k F_p t} \tag{3.8}$$

where $F_p = T_p^{-1}$ and:

$$c_k = \frac{1}{T_p} \int_{-T_p/2}^{T_p/2} x_p(t) e^{-j2\pi k F_p t} \mathrm{d}t \tag{3.9}$$

However, for an aperiodic signal, it is a fact that $x_p(t) = x(t)$ from $-\infty$ to ∞ due to the infinite period, and thus, the preceding equation can be rewritten as:

$$c_k = \frac{1}{T_p} \int_{-\infty}^{\infty} x(t) e^{-j2\pi F_p t} \mathrm{d}t \tag{3.10}$$

From this last expression, the Fourier transform, $X(f)$, for an aperiodic signal $x(t)$ is defined as:

$$X(f) = \int_{-\infty}^{\infty} x(t) e^{-j2\pi k F_p t} \mathrm{d}t \tag{3.11}$$

By looking at the two previous equations, it can be seen that:

$$c_k = \frac{1}{T_p} X(kF_p) \tag{3.12}$$

which allows to rewrite $x_p(t)$ as:

$$x_p(t) = \frac{1}{T_p} \sum_{k=-\infty}^{\infty} X\left(\frac{k}{T_p}\right) e^{j2\pi k F_p t} \tag{3.13}$$

By taking the limit with $\Delta f = T_p^{-1}$ and $\Delta f \to 0$, the above equation transforms into:

$$x(t) = \lim_{\Delta f \to 0} \sum_{k=-\infty}^{\infty} X(k\Delta f) e^{-j2\pi k \Delta f t} \Delta f \tag{3.14}$$

which is exactly equal to:

$$x(t) = \int_{-\infty}^{\infty} X(f) e^{j2\pi ft} \mathrm{d}f \tag{3.15}$$

This is the definition of the inverse Fourier transform.

Discrete Fourier Transform and Fast Fourier Transform

For a sampled signal, it is not possible to simply integrate to obtain the Fourier transform. However, an analogous operation known as the Discrete Fourier transform (DFT) has been defined. The development to obtain it is parallel to that shown in the previous section. Therefore, this sections highlights the equations for the discrete transform, as well as the differences between them.

Let $x(n)$ be an aperiodic discrete signal. Its DFT, denoted $X(\omega)$ is defined as:

$$X(\omega) = \sum_{n=-\infty}^{\infty} x(n) e^{-j\omega n} \tag{3.16}$$

It is obvious that this signal is periodic with a period of 2π. This is in sharp contrast to the continuous Fourier transform which is defined over the range of $-\infty$ to ∞. This is a consequence of the frequency of any discrete-time signal being limited to the range of $-\pi$ to π. In practical terms, the frequency identified as π is the maximal frequency that can be extracted from a signal, as explained by Nyquist's sampling theorem, and is equal to half the sampling rate.

It can be observed that the DFT of $x(n)$ is actually of the form of a Fourier series. This eventually allows for the definition of the inverse DFT. First, it is necessary to eliminate the exponential term in the previous equations and integrate this series over the period of the DFT. This is shown below.

$$\int_{-\pi}^{\pi} X(\omega) e^{j\omega m} \mathrm{d}\omega = \int_{-\pi}^{\pi} \left(\sum_{n=-\infty}^{\infty} x(n) e^{-j\omega n} \right) e^{j\omega m} \mathrm{d}\omega \tag{3.17}$$

This expression can be evaluated if and only if the summation uniformely converges as it allows for a reversal of the summation and integration signs. The summation uniformely converges if and only if:

$$\sum_{n=-\infty}^{\infty} |x(n)| < \infty \tag{3.18}$$

Consequently, the value of the integral is:

$$\int_{-\pi}^{\pi} e^{j\omega(m-n)}\mathrm{d}\omega = \begin{cases} 2\pi, & m = n \\ 0, & m \neq n \end{cases} \tag{3.19}$$

Expanding this result into Equation (3.17):

$$\sum_{n=-\infty}^{\infty} x(n) \int_{-\pi}^{\pi} e^{j\omega(m-n)}\mathrm{d}\omega = \begin{cases} 2\pi x(m), & m = n \\ 0, & m \neq n \end{cases} \tag{3.20}$$

It follows from this that the inverse DFT is:

$$x(n) = \frac{1}{2\pi} \int_{-\pi}^{\pi} X(\omega) e^{j\omega n}\mathrm{d}\omega \tag{3.21}$$

However, the calculation of the DFT is computationally expensive. Thus, a class of algorithms known as Fast Fourier Transform (FFT) algorithms have been developed. These are simply more efficient methods of computing the DFT for sampled functions. The simulator uses a radix-2 FFT algorithm for frequency analysis. This class of algorithm is extensively detailled by Proakis in [47].

Frequency analysis of simulator results

In this section, a frequency analysis is performed on the results of the simulator shown in the previous section. Up to this point, all analysis had been conducted in the time-domain. However, unless the actual frequency of some of the movements is known, it is difficult to actually separate components for a complex signal. Thus, some form of frequency analysis is necessary.

In order to assist with comprehension, Table 3.12 provides a listing of the frequencies of the ship's motions. The bending mode natural frequencies were calculated as shown in Equation (3.1) using a ship of 50,000 gross tons with uniform mass distribution along a length of 200m. The relative amplitudes were estimated by using the values shown in Hirdaris et al. [25].

Consider now Figure 3.30, Figure 3.31 and Figure 3.32, which are the Fourier-transforms for the movement along each axis of receivers 3, 4 and 5 of simulator run 2. The graphs for receivers 1 and 2 are not shown as they approximately mirror receivers 4 and 5 as is expected given the symmetry of the receiver distribution at mid-ships. Run 2 was selected for first analysis due to the heavy noise which is

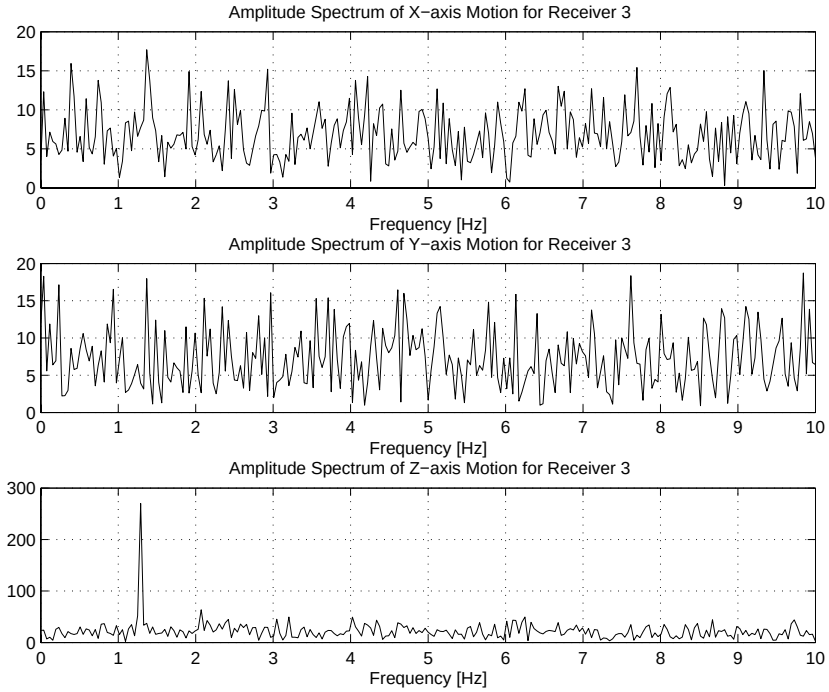

Figure 3.30: Fourier transform of mid-ships receiver movement during flexible-body simulation run 2.

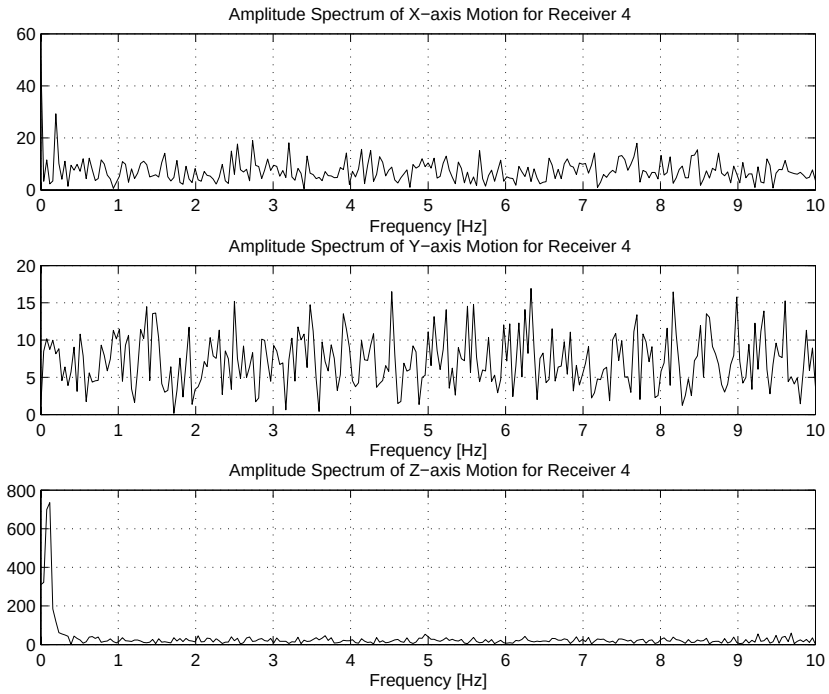

Figure 3.31: Fourier transform of the movement of the receiver located between mid-ships and the stern during flexible-body simulation run 2.

Movement	Natural Frequency [Hz]	Relative Amplitude
Pitching movement	0.1	N / A
Bending mode 1	1.2837	1
Bending mode 2	3.5386	0.1
Bending mode 3	6.9370	0.0001

Table 3.12: List of frequencies that should appear in the Fourier transform graphs.

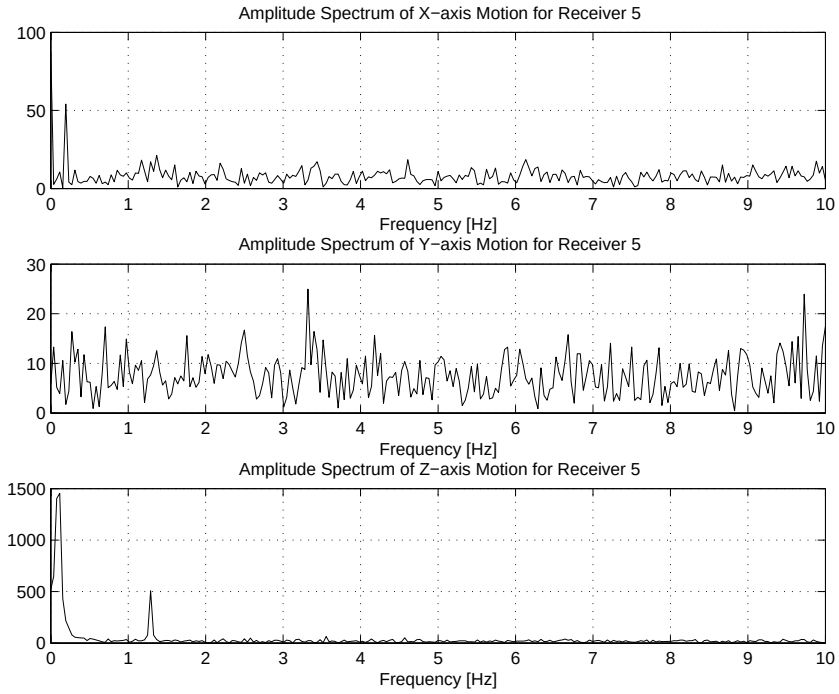

Figure 3.32: Fourier transform of stern receiver movement during flexible-body simulation run 2.

present in that run. This represents one of the worse-case scenarios.

Starting with Figure 3.30, which represents the mid-ships receiver, it is possible to notice a single frequency component spike. It is located at approximately 1.3 Hz on the z-axis movement. A simple look at Table 3.12 indicates that this movement is linked to bending mode 1. The graph of the x-axis and y-axis movement is simply the frequential distribution of white noise as there is no movement along that axis. In this particular simulation run, the magnitude of the noise drowns out any movement along the x-axis that may have been due to pitch.

Considering now Figure 3.31, which represents the frequency breakdown for the receiver located between stern and mid-ships. On this graph, it is possible to notice a pair of spikes. In this graph, there is a spike at 0.1 Hz for the x-axis movement. This is movement related to the pitch of the ship, as due to the fact that this is

not mid-ships, pitching the ship will bring about a change in the x-axis component. The second spike appears at 0.1 Hz on the z-axis movement. Referring to Table 3.12 indicates that this is the pitch frequency. As this receiver is located nearer the end of the ship, it is clear that there will be fairly significant movement due to pitch. Striking is the fact that at this location, the bending mode 1 movement appears to be non-existant. Again this would seem counter-intuative, but is explained by the fact that in an unconstrained beam, there is a node at approximately 78% of the length of the beam. As this receiver is located at 75% of the length of the ship, the small movement caused by bending mode 1 at thit point is dwarfed by the noise.

Considering now Figure 3.32, which is the frequency breakdown for the stern receiver. This graph show a trio of spikes. There is one at 0.1 Hz for the x-axis, and a pair of spikes on the z-axis movement at 0.1 Hz and 1.3 Hz. The former is due once again to the pitching movement, which at the ends of the ship will bring about significant movement. The latter indicates that the z-axis movement at this point is a combination of pitch movement with bending mode 1.

In order to make a proper comparision, the same graphs were generated for the run 3, where the noise is barely present. Figure 3.33, Figure 3.34 and Figure 3.35 are now considered.

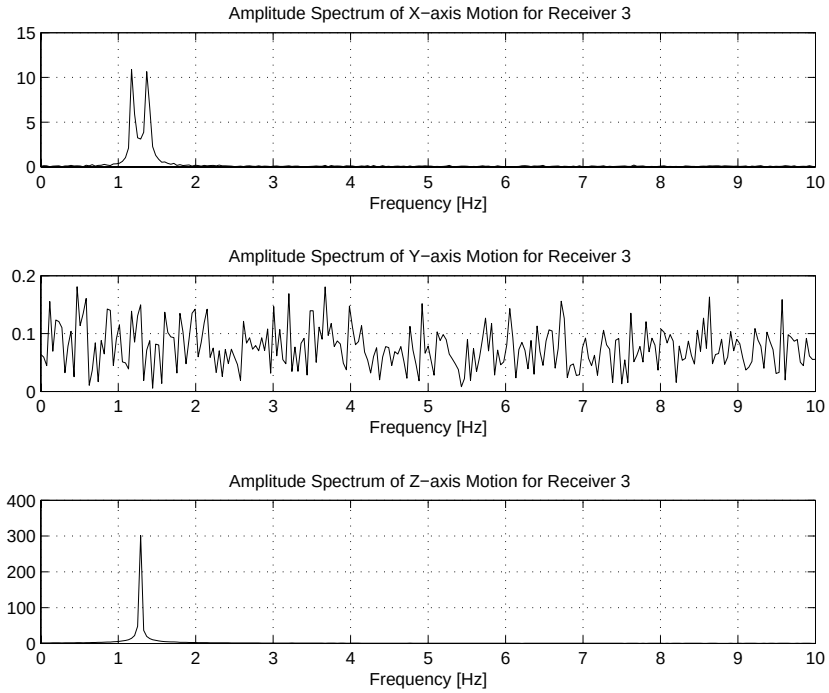

Figure 3.33: Fourier transform of mid-ships receiver movement during run 3.

First consider Figure 3.33, the mid-ships receiver frequency breakdown for run

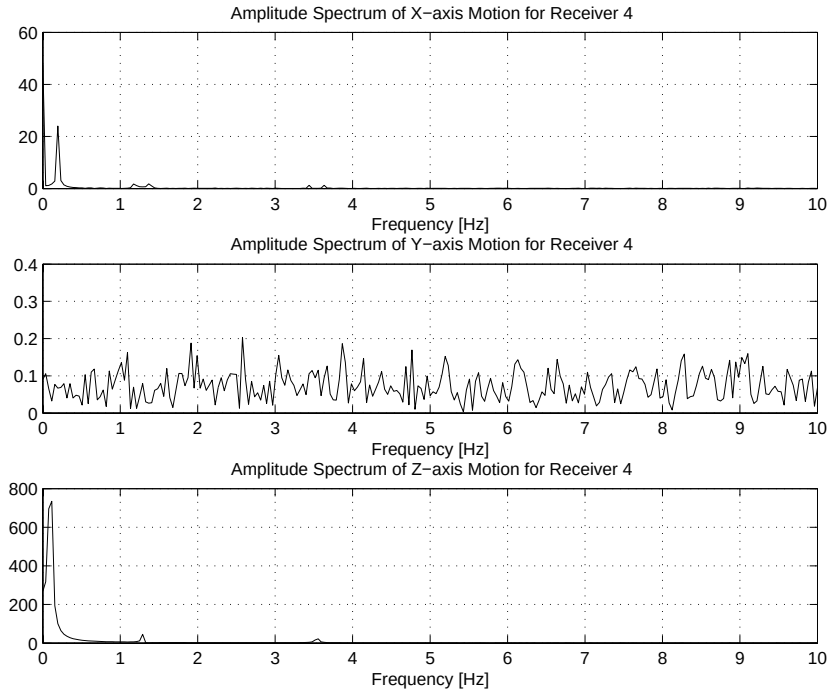

Figure 3.34: Fourier transform of the movement of the receiver located between mid-ships and the stern during run 3.

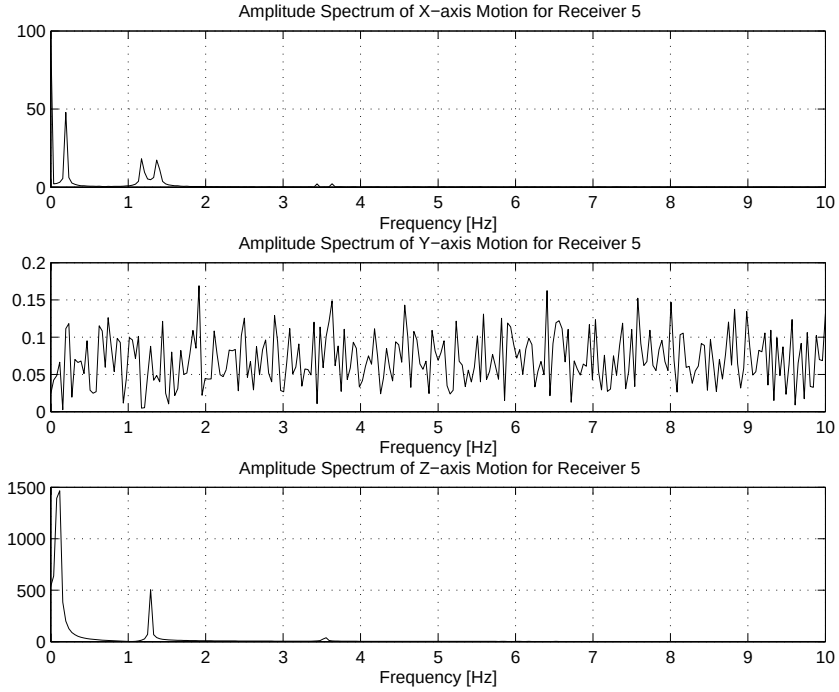

Figure 3.35: Fourier transform of stern receiver movement during run 3.

3. The same pair of spikes appear, but with considerably less noise surrounding them as expected. However, there now appears to be a pair of spikes centered around 1.3 Hz. This is explained by the fact that when the ship is pitched, the bending mode 1 movement has an x-component. The change in pitch angle, and the variation between the pitching and bending mode 1 frequencies causes this pair of spikes. In effect, this is an example of modulation in the frequency domain.

Now consider Figure 3.34. This one shows five frequency spikes. In addition to the spike at 0.1 Hz on z-axis, which is caused by the pitch movement, there are two additional small spikes at 1.3 Hz and 3.5 Hz. The first is caused by bending mode 1, whereas the second is caused by bending mode 2. These spikes are now visible due to the increase in Signal to Noise ratio (SNR).

Consider Figure 3.35. This graph shows six spikes. The first is the pitching frequency spike at 0.1 Hz for the x-axis. There are also spikes at 1.3 Hz and 3.5 Hz caused by bending modes 1 and 2. The remaining trio are at 0.1 Hz, 1.3 Hz and 3.5 Hz on the z-axis movement. They are respectively caused by pitch, bending mode 1 and bending mode 2. It could be surprising that the latter appears due to the fact that there is supposed to be a node for bending mode 2 at the stern. However, as the receiver is not exactly located on the stern, it is normal that it detects motion associated with this mode. The receiver was not placed directly on the node as it would be unrealistic to assume that the receiver could be placed directly on the stern.

Finally, to conclude this section, the relative amplitudes of bending modes 1, 2 and 3 were all set to 1 in an attempt to analyse the effect. When this experiment was run, the graph for the mid-ships receiver included an additional spike at approximately 7 Hz on the z-axis as shown in Figure 3.36. This is refered to as the flexible-body simulator run 4. This was caused by bending mode 3 and was expected. There also appears to be another pair of small spikes at 7 Hz on the x-axis. These are caused by bending mode 3.

Similar results were consistently obtained, and this was confirmed by the analysis of the error function which is shown in Table 3.10.

3.5.3 Summary of Analysis

It is clear from the above results that if centimetre accuracy, or better, be achieved by a network of receivers, it is possible to extract structural motion information. From the results obtained herein, it is clear that there was a basis on which to begin practical work, the results of which are detailed in the following chapter.

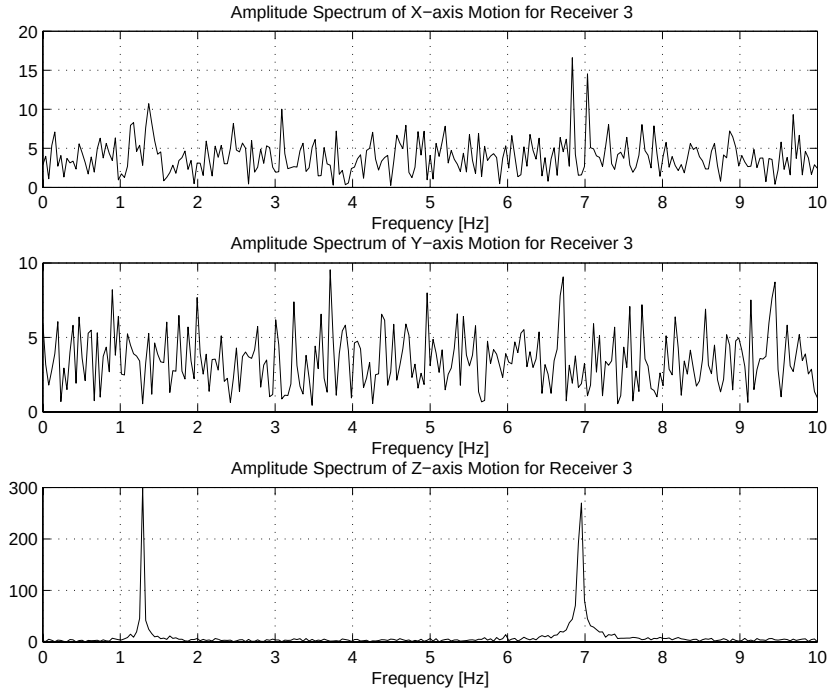

Figure 3.36: Fourier transform of mid-ships receiver movement during simulator run 4.

3.6 Optimal Receiver Placement

Equation (3.2) found earlier in this chapter describes the shape of the modes based on the model of the ship as an unconstrained pipe, that is the pipe's two ends are not fixed or attached to any support structure. This must be taken into account when determining optimal network placement. The first step of the analysis was conducted using MATLAB to determine the position of the nodes and anti-nodes for each individual mode as a function of the length of the ship. Table 3.13 shows the results of the analysis, and Table 3.14 the locations of each of these nodes.

Mode	Number of Nodes	Number of Anti-Nodes
Mode 1	2	1(3)
Mode 2	3	2(4)
Mode 3	4	3(5)
Mode 4	5	4(6)

Table 3.13: Number of nodes and anti-nodes for the first four bending modes along the bow-stern axis of the ship. The number in parentheses include the beam boundaries.

In Table 3.13, there are two numbers that appear in the anti-nodes column. The

Mode	Position of Node(s)	Position of Anti-Node(s)
Mode 1	0.2242 0.7758	0.5000
Mode 2	0.1321 0.5000 0.8679	0.3084 0.6916
Mode 3	0.0944 0.3558 0.6442 0.9056	0.2200 0.5000 0.7800
Mode 4	0.0735 0.2786 0.5000 0.7232 0.9265	0.1711 0.3887 0.6113 0.8289

Table 3.14: The position, as a percentage of length of the beam, of the nodes and anti-nodes for the first four bending modes along the bow-stern axis of the ship. This table excludes beam boundaries.

first number is the number of anti-nodes if the boundaries (i.e. the start and end points of the beam) are ignored. The number in parentheses is the one obtained if one considers the movement of the beam boundaries.

For an unconstrained beam such as that used by the simulator to model the ship, Blevins [12] describes the boundary conditions as:

$$\frac{\partial^2 Y}{\partial x^2} = \frac{\partial^3 Y}{\partial x^3} = 0 \tag{3.22}$$

where $Y(t, x)$ is the transverse deformation at time t for spanwise coordinate x.

Although the motion of the beam boundaries can be larger in amplitude than that of other portions of the ship, further analysis was necessary to see if any useful information could be extracted from the motion of the boundaries. The simulator presented earlier was used for this purpose.

By setting the amplitude of bending Modes 1 through 3 to the same level and placing receivers on the boundaries, it was found that some useful information could be extracted from the boundaries. However, at this time, some reservations remain as to how useful boundary motion information would be in practice, specifically on the grounds that the simulator assumes uniform construction.

In practice, this is not the case as, for example, most ship bows have sturdier constructions to survive any potential collisions with other vessels and slamming that may occur in rough seas. The accuracy of the simulator on the boundaries

would need to be confirmed by additional work, and as such, beam boundary information was not considered any further.

3.6.1 Receivers on anti-nodes

The first approach that was considered was that the receivers should be placed on, or as close as possible, to the anti-nodes of the ship (excluding the boundaries). As these points are those having the highest motion for any given mode, it is clear that they should present the highest signal to noise ratio. Although the work presented in Chapter 3 used evenly spaced receivers for simplicity, it was expected that the results with specific placement would be superior.

This type placement also has the advantage that some modes share anti-nodes. As an example, Modes 1 and 3 both have anti-nodes at the ship's mid-point and placing a receiver there does present a "two-for-one" situation. However, using this type of placement also presents the "disadvantage" that one of the anti-nodes in Mode 1 is also a node in Modes 2 and 4. In addition, such a placement could make for an unnecessarily large network of receivers, raising cost and complexity of the monitoring system.

The simulator was once again used to obtain the graphs showing the frequency domain for a receiver placed on the first anti-node for Mode 2, and this is shown in Figure 3.37. The relative amplitudes that were used for the different modes are shown in Table 3.15 and are based upon the results found in the Hirdaris et al. paper [25]. All other conditions are identical to that used in this chapter, except for the pitching motion which was removed.

Movement	Natural Frequency [Hz]	Relative Amplitude
Bending mode 1	1.2837	2
Bending mode 2	3.5386	1
Bending mode 3	6.9370	0.3
Bending mode 4	11.4672	0.05

Table 3.15: List of natural frequencies and relative amplitudes used to generate Figure 3.37.

Although in Figure 3.37, all four modes of bending can be seen, the amplitude of Mode 1 (the spike at 1.2 Hz) in particular is deceiving. Although in reality, Mode 1's amplitude is double that of Mode 2's, the receiver data would seem to indicate that Mode 2 is of higher amplitude than Mode 1, but this is because of the location of the receiver at an anti-node for Mode 2. Thus, such placement of

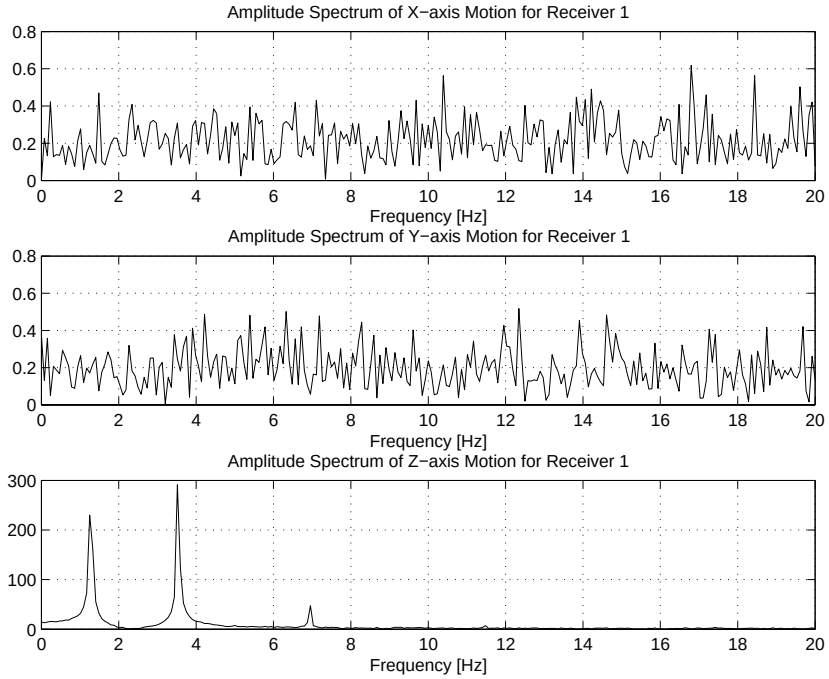

Figure 3.37: Frequency domain graph for the receiver located at the first anti-node of Mode 2.

the receivers could make results difficult to interpret. Thus, consideration of the impact of moving the receivers on the relative detected amplitude for each mode was necessary.

3.6.2 The Impact of Moving the Receivers

In this section, the impact of moving the receivers away from the mode anti-nodes is considered in terms of the strength of each mode in the frequency domain. The results in this section will be utilised in determining an optimal network placement in the following section.

Once again, a slightly modified version of the simulator was utilised for this analysis. This version moved a receiver along the length of the ship and calculated the signal strength in the frequency domain for each mode. The amplitudes used for each of the modes were normalised and the results shown in Figure 3.38.

What is clear is that there are several sections of the graph where the anti-nodes are nearly super-imposed. Thus, the consideration of how best to optimise the network configuration is also necessary.

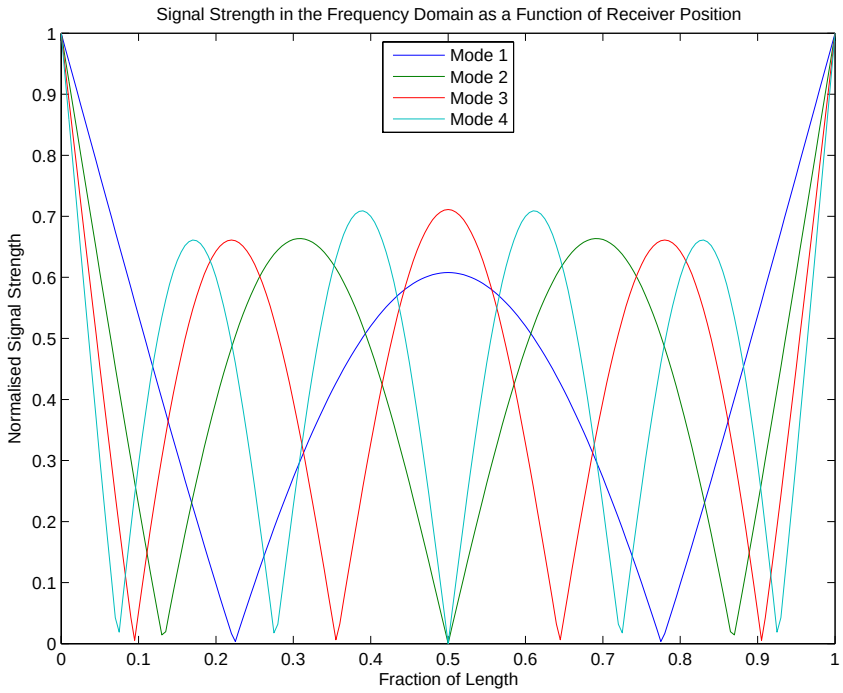

Figure 3.38: Signal strength at different locations along the ship's length for four modes.

3.6.3 Optimal Receiver Positions

Using the results obtained in the previous section, it is possible to consider a few scenarios for optimal receiver placement. Clearly, if one had an unlimited number of resources, the simplest solution is to place the receivers at all the anti-nodes. However, this is somewhat unpractical and unnecessarily complex. In this section, several possible receiver configurations and the manner in which they are obtained are considered. Whilst this discussion may be useful in order to determine optimal placement of the receivers, in practice, a ship is a far more complex structure than what is shown in this thesis. It may only be possible to use an estimate of the location of the nodes or anti-nodes in practice.

Mode 1 Measurements Only

Mode 1 motion is the one which has the highest amplitude, and is the easiest one to measure. As there is only one anti-node in this mode, it is clear that a receiver should be placed at that point. However, a single receiver is not sufficient to be able to positively identify a specific motion as being present. Ignoring error, there are three other motions which could cause spikes to appear in a frequency domain graph for the mid-ships receiver: Pitch, Roll and Heave.

This being the case, a minimum of one additional receiver is required, and this receiver would be placed at one of the nodes. Doing so would allow for the identification of the heave motion as the frequency component for heave should appear at both receivers, whereas pitch would only appear at the node, and Mode 1 bending at the anti-node only. The roll motion does not cause any significant motion along the bow-stern axis and is thus ignored.

Parameter	Value
Mode 1 Amplitude	2 [m]
Maximal Pitch	15 [degrees]
Pitch Period	8 [s]
Maximal Heave	2 [m]
Heave Period	4 [s]
GPS Vertical Error	0.03 [m]
GPS Horizontal Error	0.01 [m]

Table 3.16: Simulation settings for the Mode 1 only configuration.

To confirm the hypothesis about placement, a simulation which incorporates pitch, heave, GPS error and Mode 1 only was conducted. The settings utilised are shown in Table 3.16. Two receivers were placed onboard the ship at the first node and the mid-ships anti-node. Figure 3.39 and Figure 3.40 show the results obtained.

The behaviour seen at the second receiver (Figure 3.40) is as expected, and the spikes for the bending mode and the heave are as expected. The figure for the 1st receiver is not as expected however, but this is due to the fact that the pitching motion spike drowns out the heave spike at this location. If the pitching motion in Figure 3.39 is removed, Figure 3.41 is obtained. In practice, this may be a difficult operation.

The combination of these figures would lead to the conclusion that the original hypothesis is correct and that this is the best location if only Mode 1 movement observation is desired. This type of configuration is however extremely limited.

Single Mode Measurements

For any of the other higher modes, this thesis proposes that a minimum of three receivers is required. These should be placed preferably at the anti-nodes of the mode, with placements at nodes or anti-nodes of other modes possibly being required to rule out the spikes caused by other modes or motions.

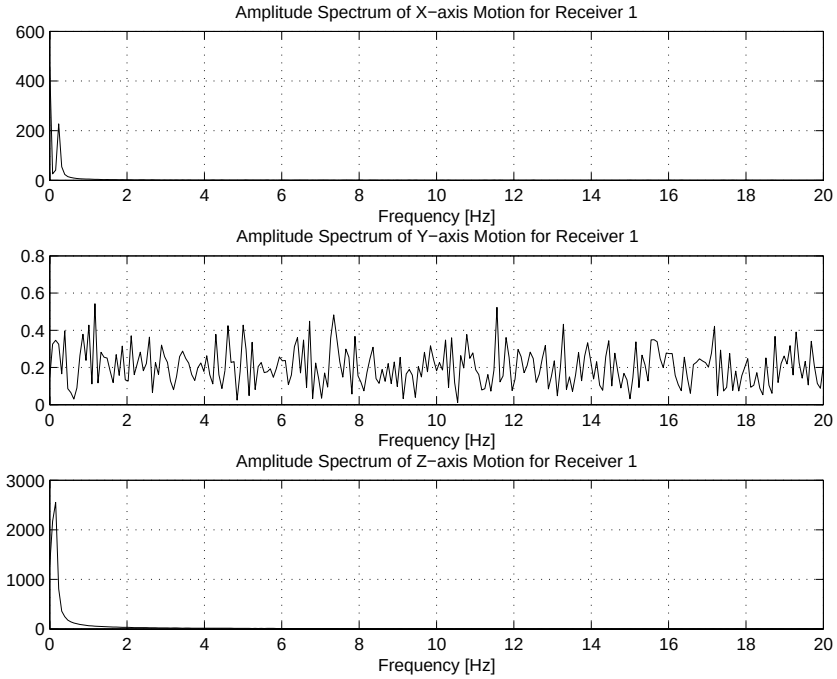

Figure 3.39: Frequency domain break-down for the receiver located on the 1st node of Mode 1.

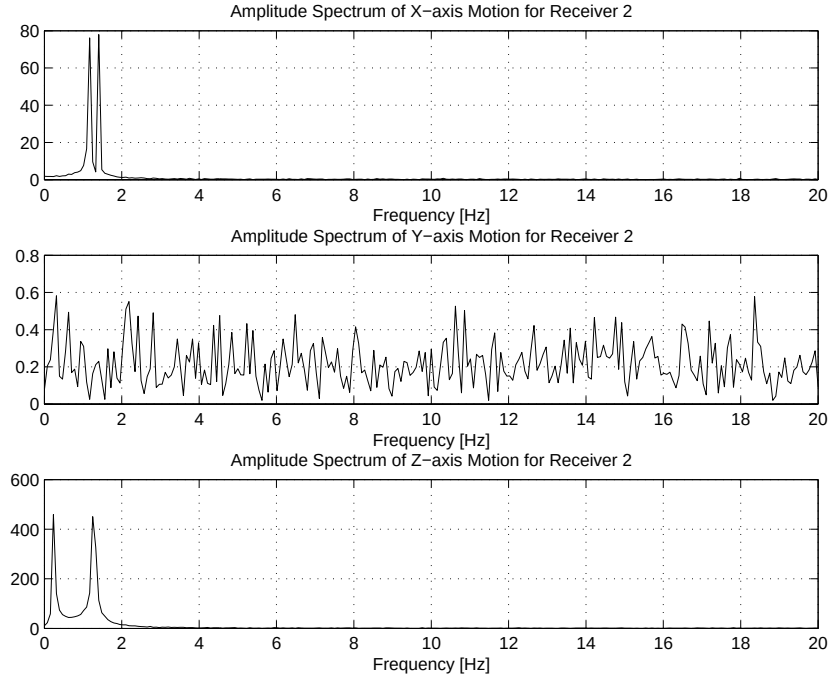

Figure 3.40: Frequency domain break-down for the receiver located on the anti-node of Mode 1.

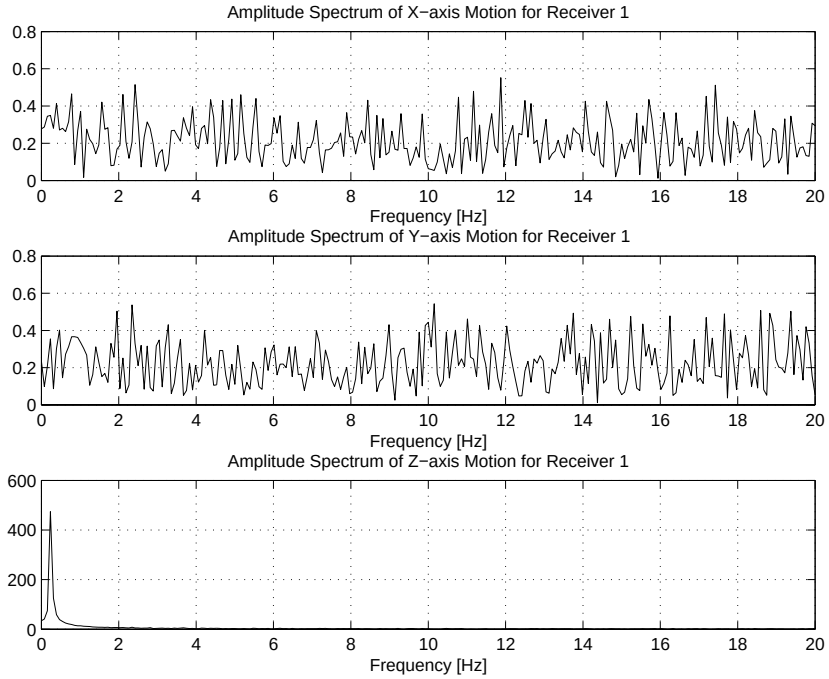

Figure 3.41: Frequency domain break-down for the receiver located on the node of Mode 1 when the pitching motion is removed.

3.6.4 Optimisation Function

Although Mode 1 is by far the easiest one to measure, it is clear that should the system be limited to this, it loses a great deal in terms of effectivness and purpose. Some type of optimisation method to attempt to find the best locations for receiver placement had to be developed. In effect, this is a variant of the problem of mode shape determination, a classic problem in the structures engineering community [37]. Although there were are a wide-variety of methods that exist to determine optimal sensor placement, it was found that for this particular application the development of a variant method was a simpler alternative.

The initial idea was to use a normalised weighted optimisation function to determine optimal locations based on the importance associated by the user to each mode. Returning to the graph of Figure 3.38, the weighted function is written in the form:

$$\psi(\ell) = \sum_{i=1}^{\mathrm{n}} \alpha_i \beta_i(\ell) \tag{3.23}$$

where α_i is the weight applied to $\beta_i(\ell)$ which is the normalised signal strength at location ℓ along the ship's main axis.

The next factor is determining the values of α_i that needs to be used in this

fuction. Should the user be more interested in specific modes the value of α for those particular modes would be raised accordingly.

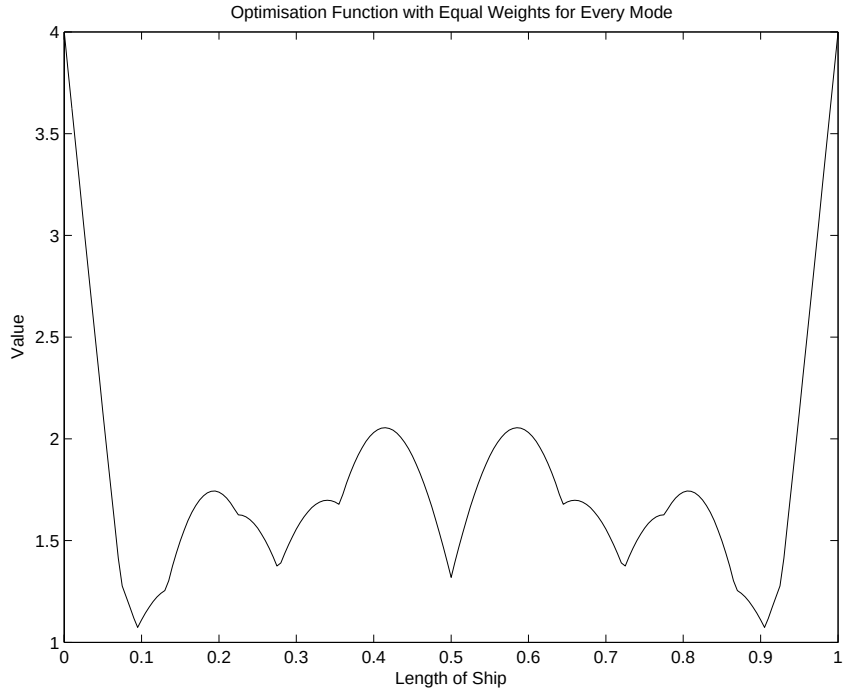

Figure 3.42: The optimisation function with equal weight assigned to the first four modes.

In Figure 3.42, $\alpha = 1$ for every mode, that is an equal importance is associated to every mode. There are 4 easily distinguished local maxima at 19.5%, 41.5%, 58.5% and 80.5% of the length. Receivers were placed at these locations and a simulation was run. Mode amplitude used the values shown in Table 3.15. The results of this simulation are shown in Figure 3.43 through to Figure 3.46. For this simulation, it was necessary to double the sampling rate to 40Hz due to the presence of Mode 4, which has a natural frequency of over 11Hz. This explains the frequency range of 0Hz to 20Hz which appears in these figures. The same is true later in this section when the optimisation function is put to use to obtain better information on the higher modes.

In these simulation results, in all four receivers, the motion of all four modes is visible, albeit that of Mode 4 is barely above the error level. Assuming that extracting information from Modes 3 and 4 is of the utmost importance whereas the information of Modes 1 and 2 can be ignored, then the ratios between the values of $\alpha_{3,4}$ and those of $\alpha_{1,2}$ must be increased. Figure 3.47 shows the optimisation function when different values are taken for α in order to meet this scenario. An ambiguity could remain on pitch and heave motion so it may potentially be necessary to add

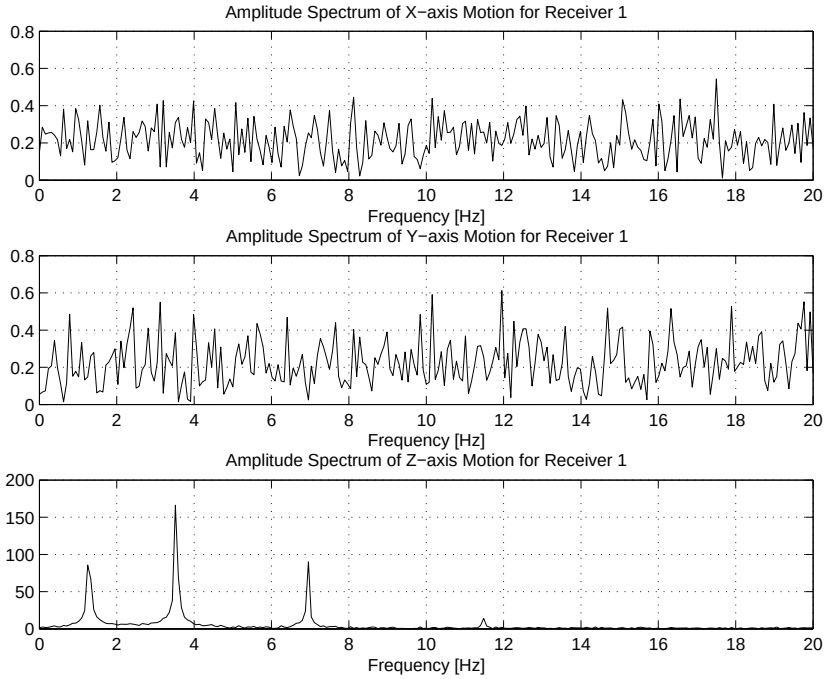

Figure 3.43: Frequency breakdown for the motion on the receiver at 19.5% of the length

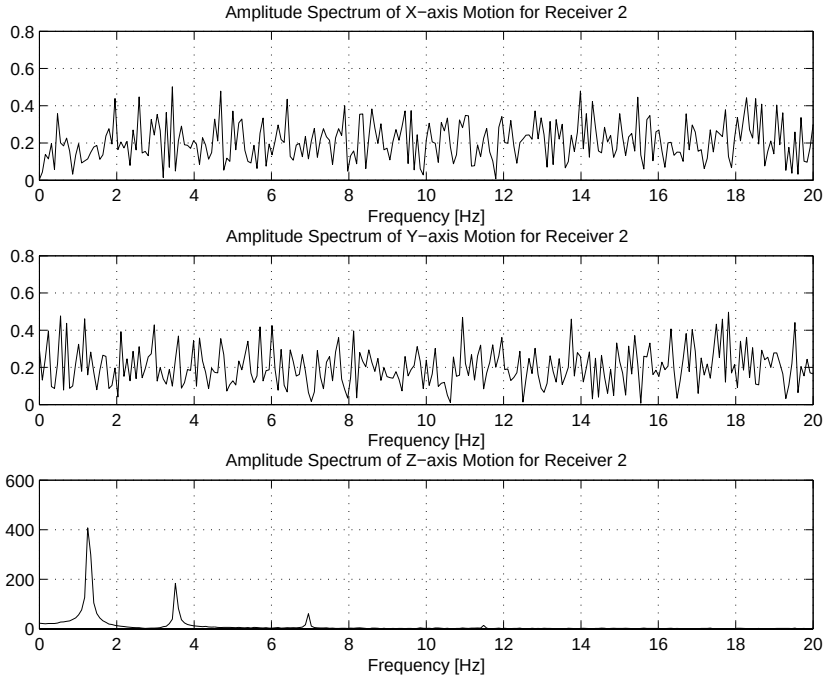

Figure 3.44: Frequency breakdown for the motion on the receiver at 41.5% of the length

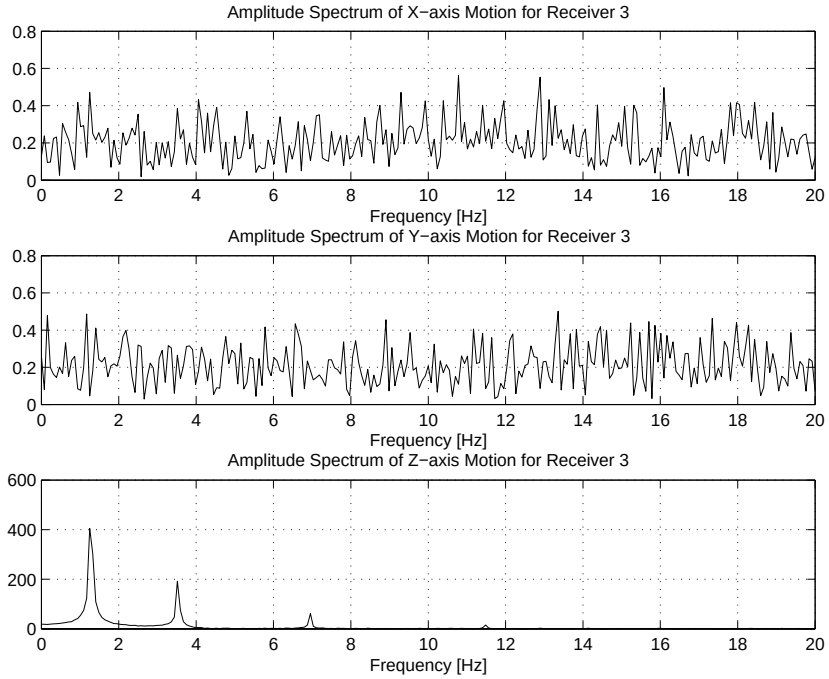

Figure 3.45: Frequency breakdown for the motion on the receiver at 58.5% of the length

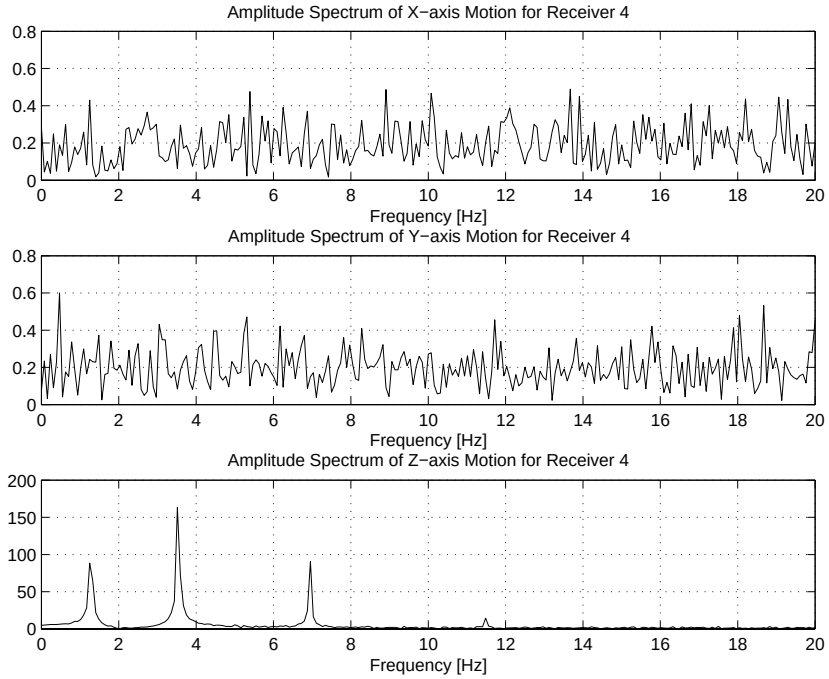

Figure 3.46: Frequency breakdown for the motion on the receiver at 80.5% of the length

a fifth receiver at mid-ships to eliminate it.

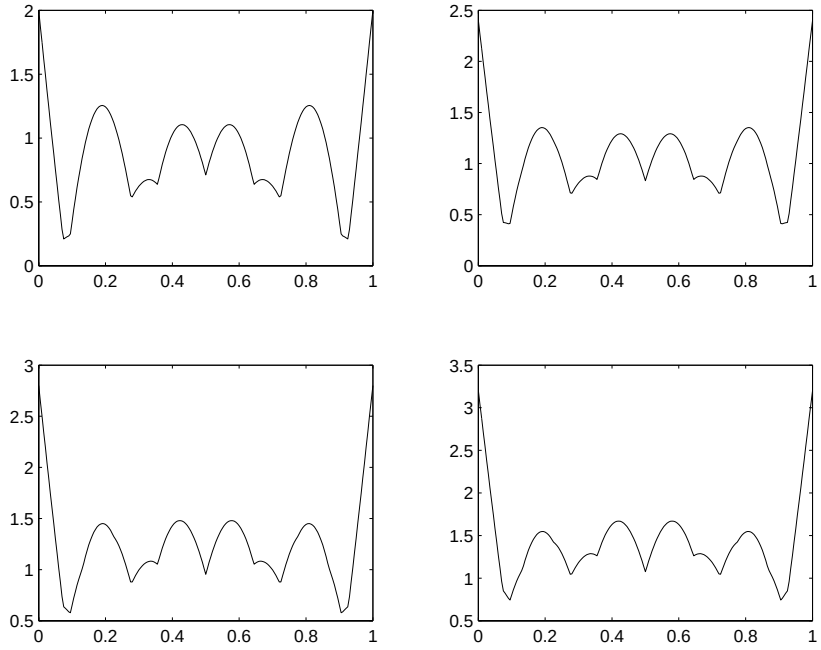

Figure 3.47: Optimisation function where the values of $\alpha_{1,2}$ are changed to import more weight to Modes 3 and 4. Clockwise from the top-left, the values of $\alpha_{1,2}$ are taken to be 0, 0.2, 0.4 and 0.6, whereas the values of $\alpha_{3,4}$ are left at 1.

However, it was found that under this scenario, the values of the function varied very little when compared to the one shown in Figure 3.42 where all weights had equal importance. The same figure as that shown in Figure 3.47 was generated for the scenario where Modes 1 and 2 are those the user wishes to measure and is shown in Figure 3.48.

There is an obvious difference in the form of the graphs show in Figure 3.48 and the one from Figure 3.42 and as such in most of the graphs there are but two obvious local maxima. However, as discussed previously, two receivers are not sufficient to allow for differentiation of flexible body motion over rigid body motion. Thus additional receivers placements must be selected.

The next local maxima in terms of importance were selected for placement of an additional receiver. In order to ensure that near identical readings are not taken, it was necessary to ensure a certain level of separation between receivers. In all cases, the receivers were never closer to each other than 5% of the length of the ship, or 10m in this case as the simulated vessel is 200m long.

A simulation was run for the first case where the values of $\alpha_{1,2}$ are set to zero. Receivers were placed at 22%, 36%, 64% and 78% of the ship's length. The results are shown in Figure 3.49 to Figure 3.52.

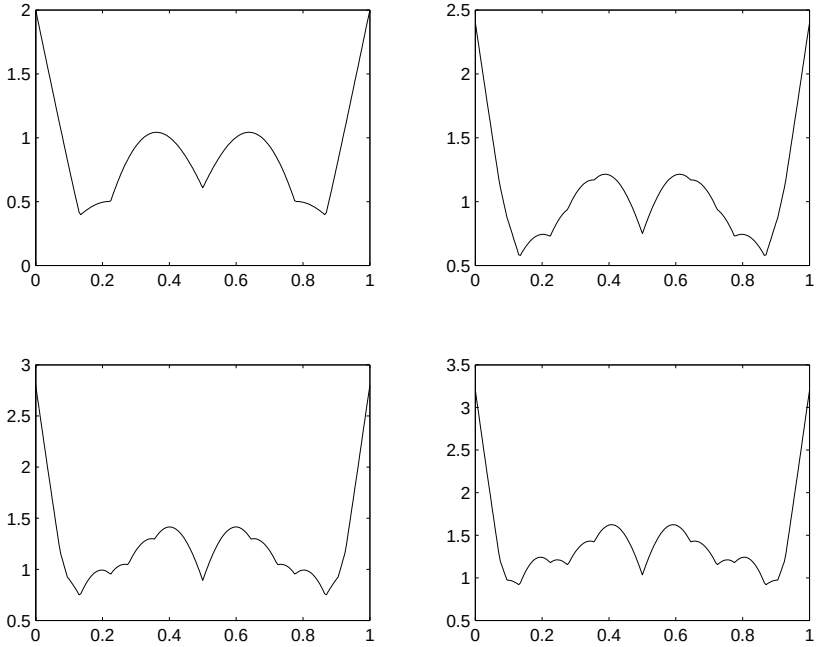

Figure 3.48: Optimisation function where the values of $\alpha_{3,4}$ are changed to import more weight to Modes 1 and 2. Clockwise from the top-left, the values of $\alpha_{3,4}$ are taken to be 0, 0.2, 0.4 and 0.6, whereas the values of $\alpha_{1,2}$ are left at 1.

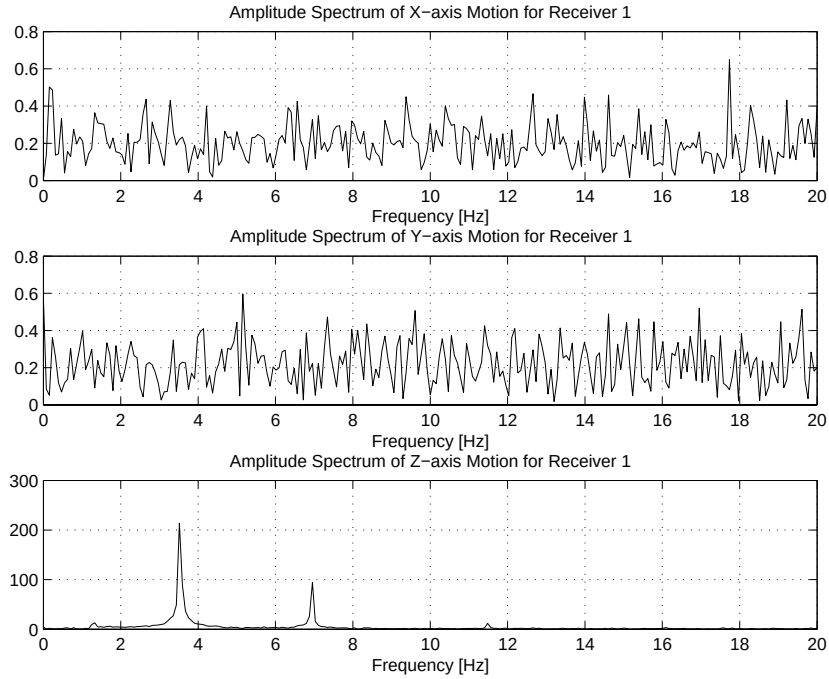

Figure 3.49: Frequency breakdown for the motion on the receiver at 22% of the length.

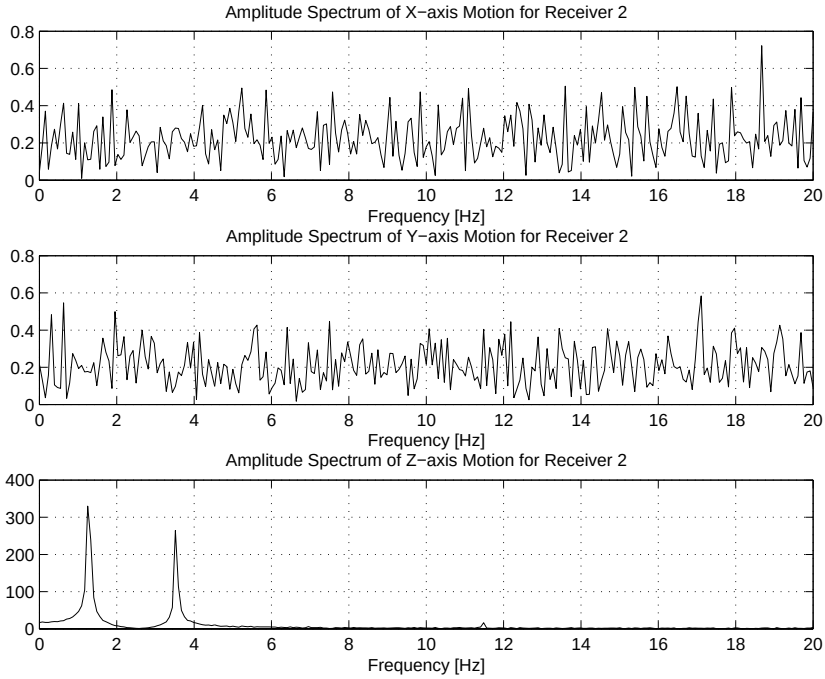

Figure 3.50: Frequency breakdown for the motion on the receiver at 36% of the length.

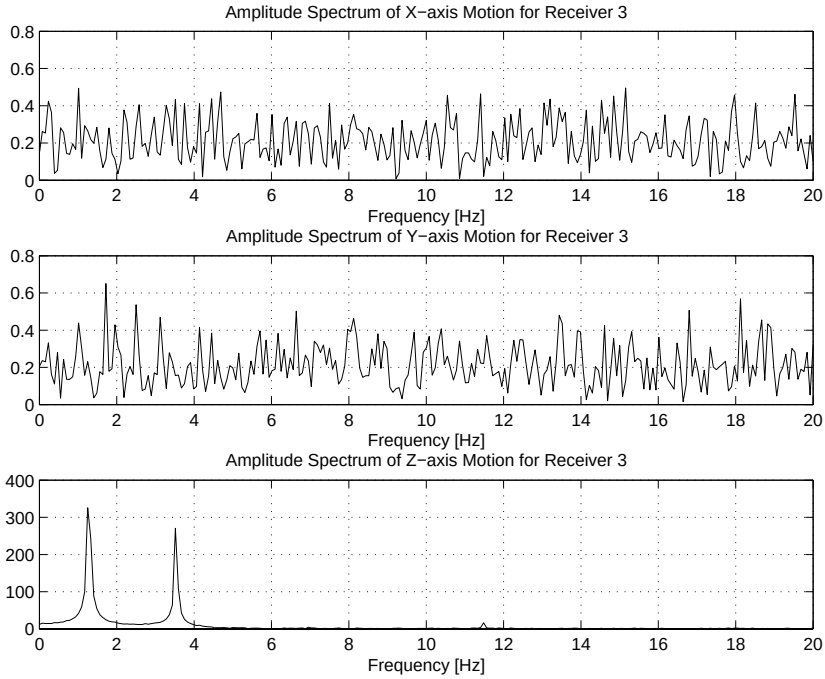

Figure 3.51: Frequency breakdown for the motion on the receiver at 64% of the length.

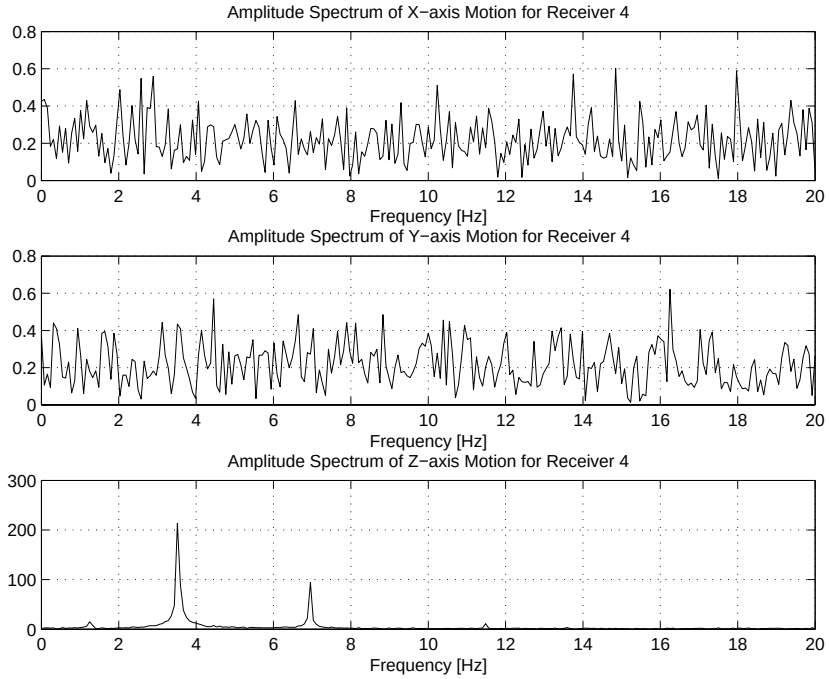

Figure 3.52: Frequency breakdown for the motion on the receiver at 78% of the length.

In this particular case, due to the fact that Mode 3 is clearly visible on several of the figures, it is necessary to add a fifth receiver at midships which permits differentiation between the different modes. This removes the ambiguity as to which motion is visible at what time. The results at this receiver are shown in Figure 3.53.

Closing Remarks Regarding Receiver Positioning

Although it is possible to position the receivers in such a manner that optimises the obtention of data from specific multiple modes, should this be desired, the simpler tactic is to place the receivers in order to optimise collection of data from all the modes. Then, using the data set, to simplify eliminate the data from modes using logical analysis or use a simple filter to achieve the same result, the latter seemingly being a simpler option provided some information about the vessel is known.

In the case of the scenario shown in Figure 3.49 to Figure 3.53, the user is interested in the the lower modes, so the best type of pass-band filter is a low-pass filter. A simple sixth-order Butterworth Finite Impulse Response (FIR) low-pass filter was quickly implemented in MATLAB. The cutoff frequency was selected as 5Hz, meaning that the movement of Modes 3 and 4 should be nearly or completely eliminated. The amplitude and phase response of the filter is shown in Figure 3.54.

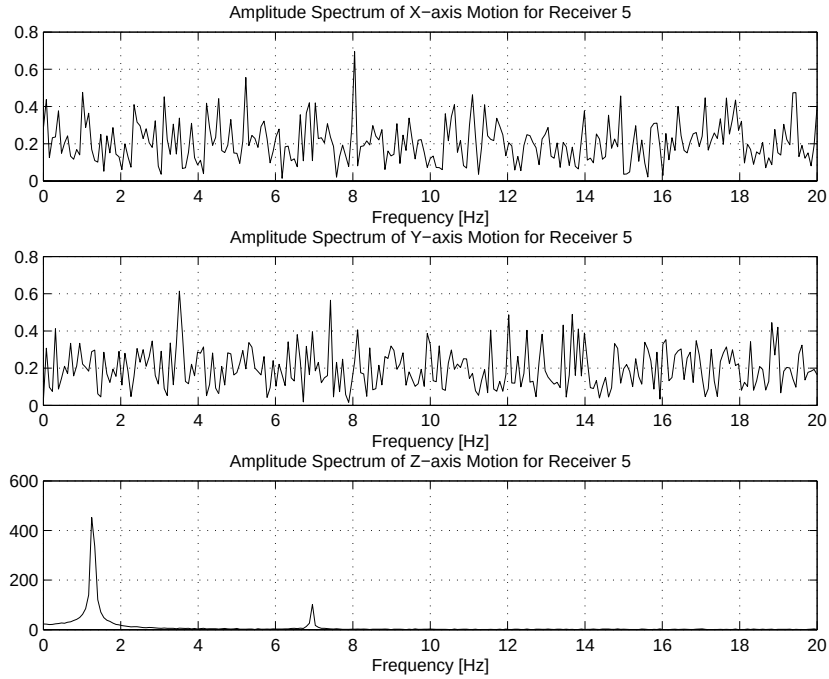

Figure 3.53: Frequency breakdown for the motion on the receiver at mid-ships.

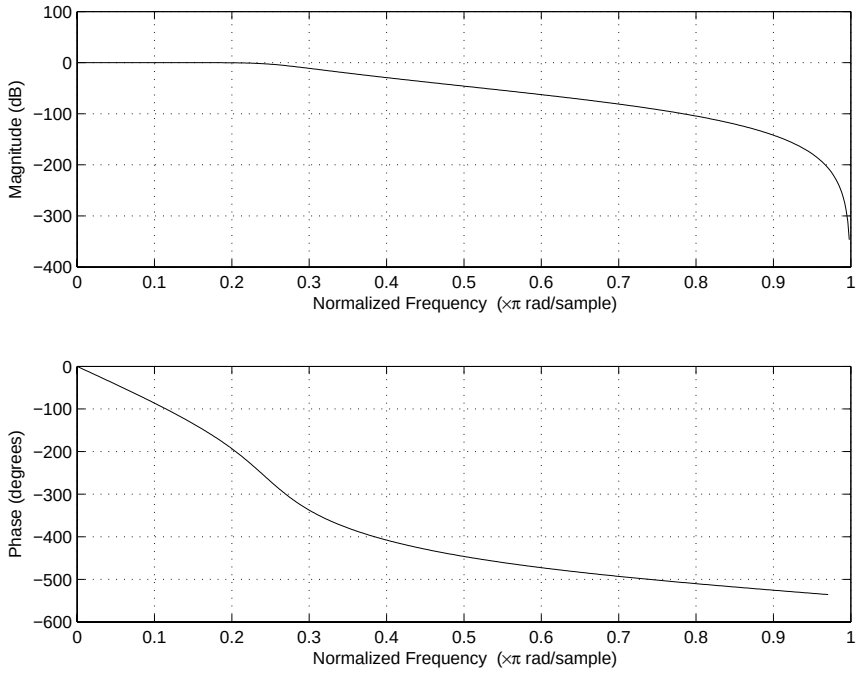

Figure 3.54: Amplitude and Phase response, with normalised frequency, for the sixth-order Butterworth low-pass filter.

The results of the filtering are shown in Figure 3.55 alongside the original frequency domain data for the bending mode only.

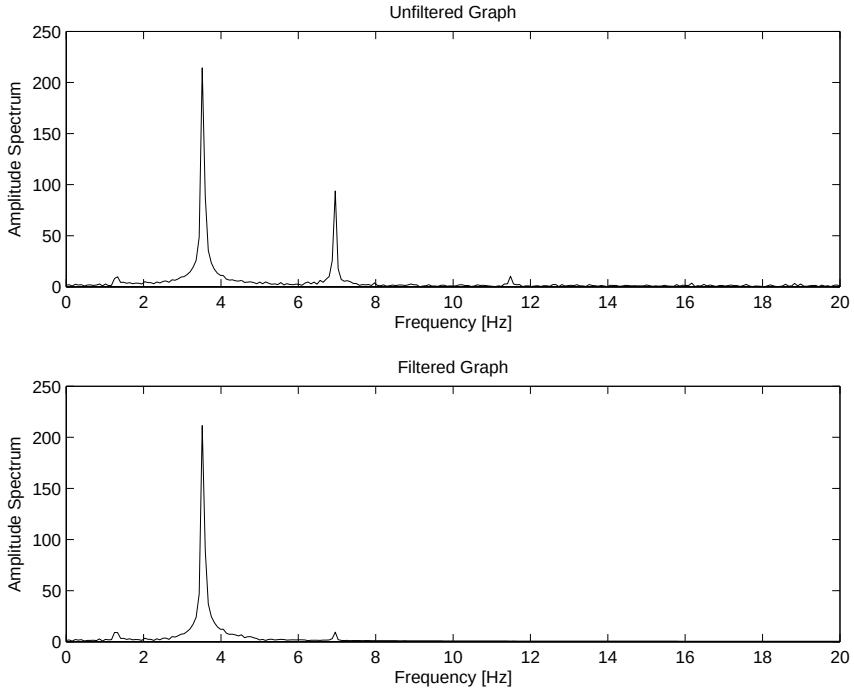

Figure 3.55: The filtered and unfiltered frequency domain data for bending along the main axis of the ship.

As expected, the spikes associated with Mode 3 is almost completely eliminated, whereas the spike for Mode 4 has been removed. Some distortion is introduced by filtering although is it is not particularly obvious in this case, as the Butterworth filter has a fairly flat amplitude response across the pass-band. This is the main reason this type of filter was chosen over other types. Although other filters such as the Chebyshev Type I/Type II or Elliptical filters present a much sharper cutoff, they also incorporate rippling effects into the passband which may lead to some distortion.

The key thing to note however is that for filters to be used, some information about the ship such as the natural frequencies must be known. Otherwise there is no guarantee that the cutoff will not be poorly chosen. If no information is known, logical analysis based on optimal placement of the receivers for all modes must be done. At present, this analysis is done manually, but it could certainly be automated by software in future work.

3.7 Impact of the Galileo Constellation Deployment

In this section, the impact that the deployment of Europe's Galileo will have on a structural monitoring system is briefly considered. Scheduled to become operational sometime around 2012, the Galileo system is supposed to offer some improvements over the use of GPS alone, in particular, the use of an integrity monitoring system [27]. This is particularly important in light of the fact that Galileo will provide safety of life services, for which uncorrupted data is an important requirement. Although the advantages of the deployment of the Galileo constellation are numerous, this document takes particular interest in the advantages gained by having a larger number of visible satellites.

In this section, a description of the Galileo constellation is first made. This is followed by a simulation supported analysis of the practical impact of this deployment. Specifically, this analysis concentrates on the gain in terms of visible satellites versus GPS alone. In addition, a description of an efficient solution to the integer ambiguity problem is provided. Finally, this section concludes with an analysis of Dilution of Precision (DOP) gains due to Galileo deployment.

3.7.1 Constellation Orbits

The information presented in this section is primarily a synthesis of the information available in [4, 11]. The Galileo constellation will consist of thirty satellites in Medium Earth Orbit (MEO) at an altitude of 23,222 km. These satellites will be spaced evenly onto three orbital planes each having an inclination of 56^o. The complete set of orbital parameters used for the determination of these orbits is shown in Table 3.17.

Coordinate Type	**Plane 1**	**Plane 2**	**Plane 3**
Eccentricity (e)	1×10^{-5}	1×10^{-5}	1×10^{-5}
Inclination (i)	56^o	56^o	56^o
Semi-Major Axis (a)	29,994.17 km	29,994.17	29,994.17
Rate of Right Ascension ($\dot{\omega}$)	0	0	0
Argument of Perigee (w)	0^o	12^o	24^o
Longitude of Ascending Node (Ω_0)	0^o	120^o	240^o

Table 3.17: Orbital parameters for the Galileo orbital planes.

Each plane therefore has ten satellites, of which nine are active and one is an active spare. This is a higher number than GPS, which as of late June 2006 had twenty-nine satellites in orbit in six planes. Due to the interoperability of the

Galileo and GPS, users of the Global Navigation Satellite System (GNSS) will be able to utilise a minimum of fifty-one satellites, plus three active spares (this number is quoted using a minimum of twenty-four GPS satellites in orbit).

Additionally, each satellite within the plane has a particular Mean Anomaly (denoted M_0) at a reference time. As the satellites are evenly spaced out on the plane, these values are assumed to be $0^o, 36^o, 72^o, \ldots, 288^o, 324^o$ degrees for each satellite at the reference. Based on this information, we can calculate the approximate position of each satellite at a particular time, t, based on the information from a certain reference time, T_e.

First, it is necessary to calculate the time elapsed since the reference, Δt:

$$\Delta t = t - T_e \tag{3.24}$$

Using this, we can calculate mean motion, n_0:

$$n_0 = \sqrt{\frac{\mu}{a^3}} \tag{3.25}$$

where μ is the Earth's gravitational constant ($3.986005 \times 10^{14} [m^3/s^2]$).

From the value of mean motion, we can then calculate the new value of mean anomaly, M:

$$M = M_0 + n_0 \Delta t \tag{3.26}$$

It is now necessary to solve Kepler's equation for eccentric anomaly, E. Kepler's equation can be rewritten in the form of

$$E = M + e \sin(E) \tag{3.27}$$

By iterating for E using the preceding equation, with $E = M$ as the initial condition, the value of E will quickly converge. From the value of eccentric anomaly, we can calculate the sine and cosine of ν, the true anomaly:

$$\left.\begin{aligned} \cos(\nu) &= \frac{\cos(E) - e}{1 - e\cos(E)} \\ \sin(\nu) &= \frac{\sin(E)\sqrt{1 - e^2}}{1 - e\cos(E)} \end{aligned}\right\} \tag{3.28}$$

From the true anomaly, we can calculate the argument of latitue, φ:

$$\varphi = \nu + \omega \tag{3.29}$$

In addition to the argument of latitude, it is necessary to obtain the corrected orbit radius, r, in order to calculate the position of the satellites in orbit:

$$r = a(1 - e\cos(E)) \tag{3.30}$$

From the corrected radius and and the argument of latitude, we can obtain the XY coordinates of the satellite in its orbit plane, $\bar{x}$ and $\bar{y}$ as follows:

$$\left.\begin{aligned} \bar{x} &= r\cos(\varphi) \\ \bar{y} &= r\sin(\varphi) \end{aligned}\right\} \tag{3.31}$$

The next step is to calculate the position of the satellite in the Earth Centered Earth Fixed (ECEF) coordinate frame. To do that, it is first required to obtain the corrected longitude of the ascending node, Ω_c. This is done as follows:

$$\Omega_c = \Omega_0 + \Delta t(\dot{\omega} - \dot{\omega}_e) - (T_e\dot{\omega}_e) \tag{3.32}$$

where $\dot{\omega}_e$ is the angular velocity of the Earth ($7.2921151467 \times 10^{-5}$ rads/s).

From these past three values, it is possible to calculate the ECEF coordinates, x, y, and z, of any of the satellites:

$$\left.\begin{aligned} x &= \bar{x}\cos(\Omega_c) - \bar{y}\cos(i)\sin(\Omega_c) \\ y &= \bar{x}\sin(\Omega_c) + \bar{y}\cos(i)\cos(\Omega_c) \\ z &= \bar{y}\sin(i) \end{aligned}\right\} \tag{3.33}$$

Figure 3.56 shows a plot of the planned Galileo orbits around the Earth. These were obtained using the above algorithm. As a basis for comparison Figure 3.57 shows both the Galileo and GPS satellite cages. The Galileo orbits are the same as in Figure 3.56. The GPS orbits are calculated using actual almanach data provided by the USCG Navigation Center. In Figure 3.57, the Galileo orbits are in blue with red circles representing the satellites, while the GPS orbits are in green with black circles representing the satellites.

From these figures, it is clearly obvious that the number of visible satellites will increase dramatically once the Galileo constellation is fully deployed. To determine if a particular satellite is visible, the simulator program follows this algorithm, knowing $\vec{\mathbf{n}}$, the user's position vector:

(i) Calculate the user to satellite vector, denoted $\vec{\mathbf{A}}$.

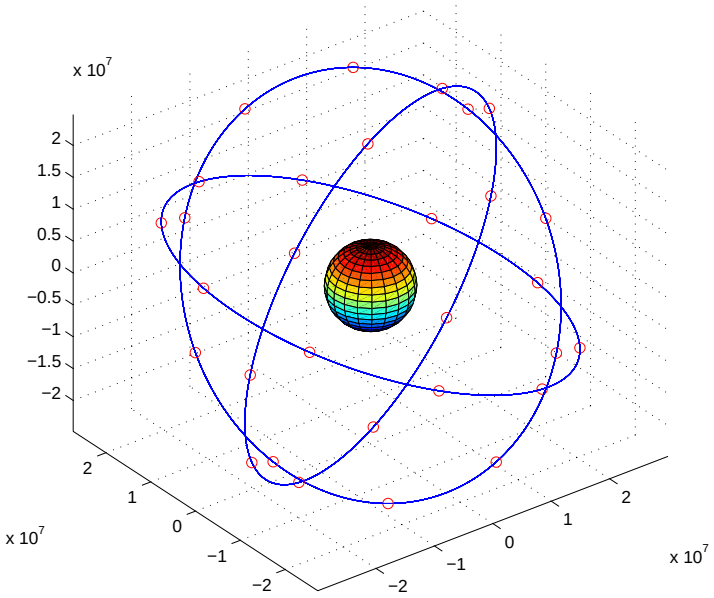

Figure 3.56: Galileo orbit planes. Axis units are in metres.

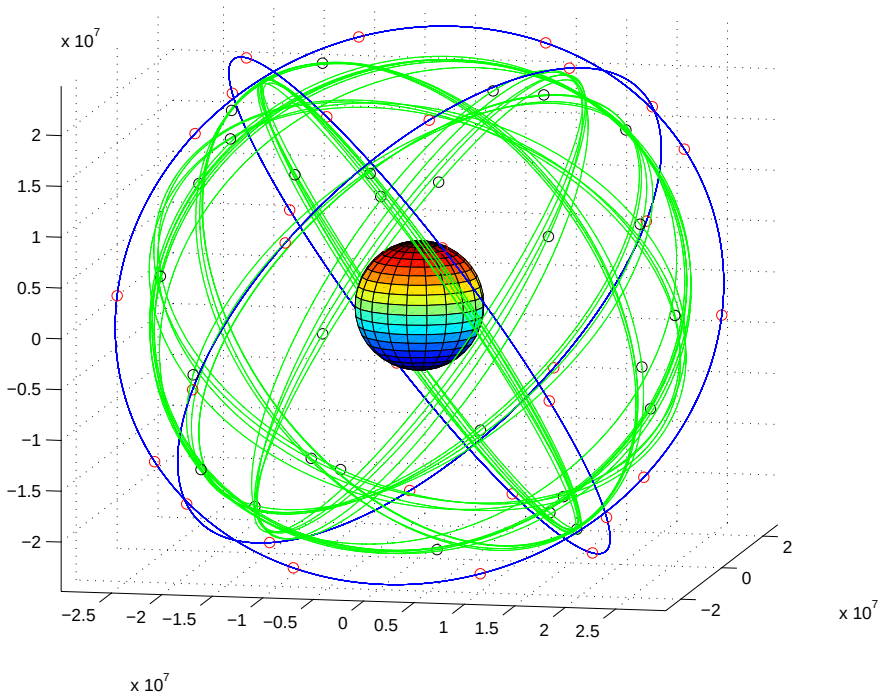

Figure 3.57: Galileo (in blue) and GPS (in green) orbit planes. Axis units are in metres. The GPS orbits were obtained from the US Air Force public almenachs.

(ii) Calculate the cosine of the angle between $\vec{\mathbf{n}}$ and $\vec{\mathbf{A}}$ using:

$$\cos(\theta) = \frac{\vec{\mathbf{n}} \cdot \vec{\mathbf{A}}}{\|\vec{\mathbf{n}}\| \|\vec{\mathbf{A}}\|} \tag{3.34}$$

(iii) Calculate the actual value of θ using the arccos function.

(iv) If 90 - θ is larger than the elevation mask, than the satellite is visible.

The simulator was used to generate a graph of the number of visible satellites in Southampton, using an elevation mask of 15^o. This mask is a reasonable one to use for land based-applications as it deals with most low-lying ground obstacles. However, in the open ocean, a much smaller elevation mask could be used as, in most cases, there are no obstacles in the vicinity. The result, shown in Figure 3.58 confirms the marked increase in total number of visible satellites. The increase in

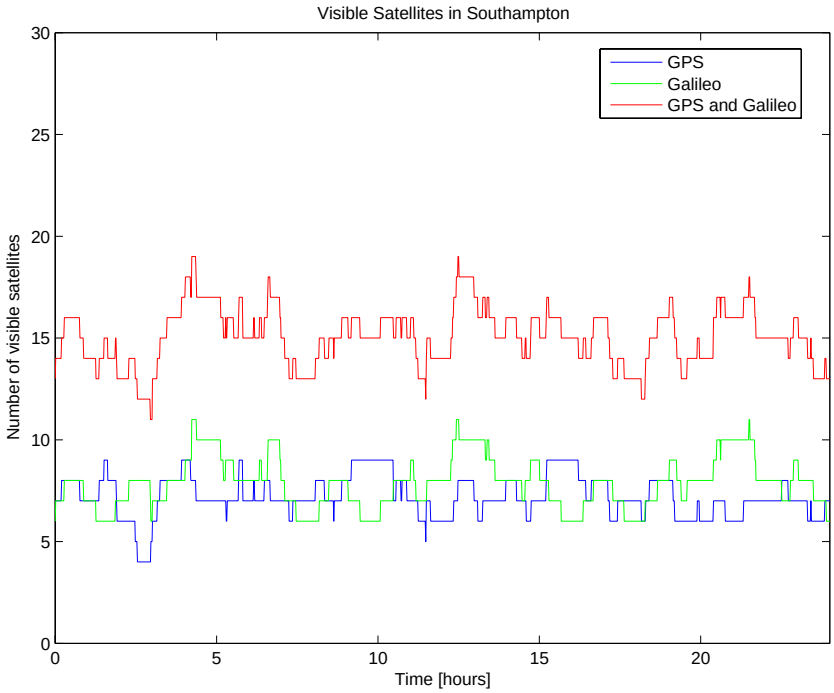

Figure 3.58: Visible GNSS satellites in Southampton (UK).

the number of visible satellites will also have an impact on the DOP. The following section makes a mathematical analysis by comparing the DOP of standalone GPS and Galileo with that of the combined GNSS.

3.7.2 Impact on Dilution of Precision

The position of the satellites has a direct impact on the accuracy of the position solution obtained. This is known as dilution of precision. The literature generally defines five different types of DOP: geometric DOP (GDOP), position DOP (PDOP), time DOP (TDOP), horizontal DOP (HDOP) and vertical DOP (VDOP) [26]. DOP links the statistical accuracy of the solution with the position of the satellites in the sky. A low of value of GDOP is indicative of better geometry, with a DOP of one being the best possible value.

In order to increase accuracy of the position solution, it is desirable to minimise DOP of any type. In general, it is assumed that in the case where one selects four satellites to obtain a position, one minimises GDOP in particular by maximising the volume of the prism formed by the satellites the receiver has locked on to. However, some research [61] has led to the conclusion that maximising satellite constellation volume does not lead to minimal GDOP. In the following analysis, the defintion of GDOP used by Zhu is utilised. For better comprehension, Zhu's algorithm is reproduced here.

First, let $\mathbf{G}$, the geometry matrix, be defined as:

$$\mathbf{G} = \begin{bmatrix} e_{11} & e_{12} & e_{13} & 1 \\ e_{21} & e_{22} & e_{23} & 1 \\ e_{31} & e_{32} & e_{33} & 1 \\ e_{41} & e_{42} & e_{43} & 1 \end{bmatrix} \tag{3.35}$$

where e_{i1}, e_{i2} and e_{i3} are the direction cosines from the satellite to the user.

It is possible to simply the equation to calculate GDOP to:

$$GDOP = \sqrt{\mathrm{tr}(\mathbf{G}\mathbf{G}^T)^{-1}} \tag{3.36}$$

where $\mathbf{G}^T$ and tr($\mathbf{G}$) are the transpose and trace of matrix $\mathbf{G}$.

However, the matrix inversing operation is computationally expensive and thus not very practical for any real-time applications. Therefore, Zhu developed the closed-form solution of Equation (3.36). Let:

$$B_{ij} = e_{i1}e_{j1} + e_{i2}e_{j2} + e_{i3}e_{j3} + 1, \quad 1 \leq i < j \leq 4 \tag{3.37}$$

and

$$a = (B_{12}B_{34} + B_{13}B_{24} - B_{14}B_{23})^2 - 4(B_{12}B_{34}B_{13}B_{24}) \quad (3.38)$$

$$b = 16 - 4(B_{12}^2 + B_{13}^2 + B_{14}^2 + B_{23}^2 + B_{24}^2 + B_{34}^2) \quad (3.39)$$

$$c = 2\left[B_{12}(B_{13}B_{23} + B_{14}B_{24}) + B_{34}(B_{13}B_{14} + B_{23}B_{24})\right] \quad (3.40)$$

It is now possible to calculate GDOP using the following simple expression:

$$GDOP = \sqrt{\frac{16 + b + c}{a + b + 2c}} \quad (3.41)$$

which is far less computationally demanding than the recursive operation of inversing a matrix.

In Southampton, for the same 24 hour period shown in Figure 3.58, the value of GDOP for GPS and Galileo standalones, compared to a combined GNSS network is shown in Figure 3.59. A best four approach was utilised, the four satellites resulting in minimal GDOP were selected for use in this calculation. Clearly, and as

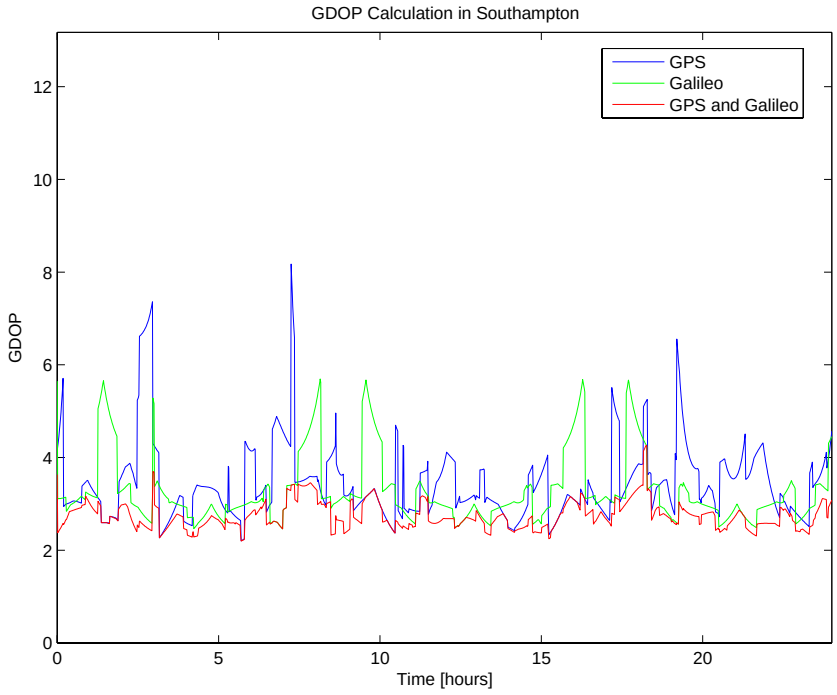

Figure 3.59: GDOP values over 24 hours in Southampton.

expected, the value of GDOP for the combined GNSS network is the lowest of all values. Table 3.18 gives more detail about the results shown in Figure 3.59.

At times where the GDOP spikes occur, the geometry of the satellites is indeed

Value	GPS	Galileo	Combined GNSS
Mean GDOP	3.4462	3.2677	2.7412
Min GDOP	2.2021	2.4597	2.1991
Max GDOP	8.1736	5.6945	4.2642
Standard deviation	0.8253	0.7233	0.2899

Table 3.18: Details of the GDOP results shown in Figure 3.59.

relatively poor as shown in Figure 3.60. In this figure, the geometry of the GPS satellites for the spike near 0700 hours is shown. Likewise, a similar figure for the

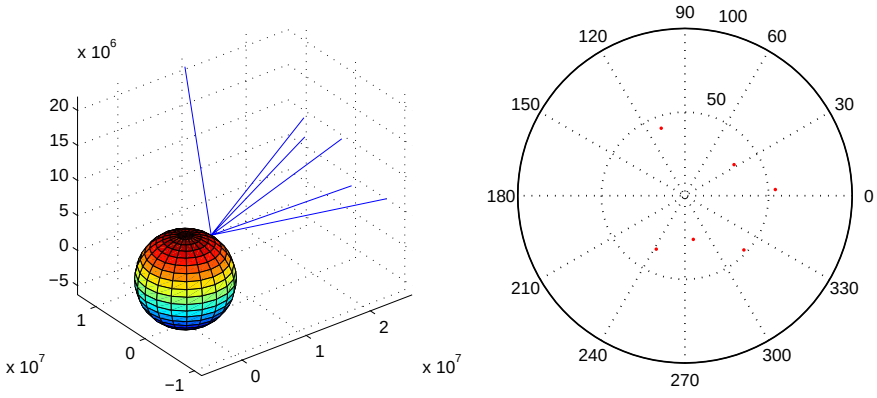

Figure 3.60: GPS satellite geometry at 0700 hours from Figure 3.59.

Galileo geometry is shown in Figure 3.61.

Similar work has already been been performed. In 2003, Wu et al. [59] presented a paper in which the GDOP values and visible satellites were calculated for Seoul, Tokyo and Beijing. In order to compare, the constellation simulator described above was set to work out the numbers for Tokyo. The results are shown in Table 3.19.

As can be noticed, there are a few fairly significant differences between the results by Wu et al. and those obtained by the simulator, especially in terms of DOP. With regards to the number of visible satellites, the difference may be explained by the fact that the simulator uses recent constellation data. The Wu et al. paper was published in September 2003, and since that date, almanach data available from the USCG indicated that three GPS satellites were launched into orbit. Consequently, the number of visible satellites may have been altered by this. It was also believed

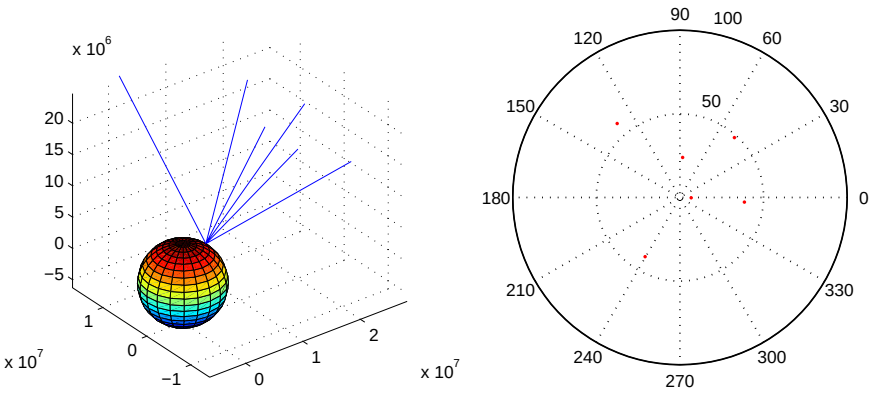

Figure 3.61: Galileo satellite geometry at 0630 hours from Figure 3.59.

Value	Wu et al.		Simulator	
	Minimal	**Maximal**	**Minimal**	**Maximal**
Visible Satellites (GPS)	4	10	5	10
Visible Satellites (Galileo)	6	10	6	10
Visible Satellites (Combined)	11	17	11	20
GDOP (GPS)	1.67	10.00	2.2646	12.9813
GDOP (Galileo)	1.72	3.74	2.5545	5.7391
GDOP (Combined)	1.30	2.94	2.2541	4.5848
Mean GDOP (GPS)	3.00		3.4965	
Mean GDOP (Galileo)	3.04		3.5053	
Mean GDOP (Combined)	1.91		2.7967	

Table 3.19: Comparison of results between Wu et al. and the constellation simulator for Tokyo.

that a different elevation mask is used by Wu et al. as they did not explicitly specify the mask they used, although this value was later deduced as 10 degrees as explained below.

With respect to the DOP values, the difference may be partially caused by the changes in the constellation, however it is more likely that the different algorithm used by Wu et al. is the primary cause. The $\mathbf{G}$ matrix used by Wu et al. is an $m \times 4$ where m is the number of visible satellites. The $\mathbf{G}$ matrix used by the simulator is a 4×4 matrix. In other words, Wu et al. consider all visible satellites in the calculation of GDOP, whereas the simulator only considers the four giving the smallest GDOP. This approach results in a larger value of GDOP than one where all the satellites

are considered.

However, what is key to the comparison is the fact that both set of datum follow the same trend. For example, mean combined GDOP is approximately 60% of mean Galileo GDOP and mean GPS GDOP, and mean Galileo GDOP is approximately 1% superior to mean GPS GDOP. The results from the simulator calculations were later confirmed by publicly available called Trimble Planning [15]. Produced by Trimble, a GPS receiver manufacturer, this software allows the user to select which satellites are to be used for any calculation. The Trimble software also seemed to validate the results by Wu et al. In addition, by observation of the results from the Trimble software, it was possible to deduce that Wu et al. used an elevation mask of 10 degrees.

Using Trimble's software for the GPS constellation as of 3 January 2009 yielded the numbers shown in Table 3.20 for a ten and fifteen degree elevation mask.

Value	**15 degree mask**	**10 degree mask**
Minimal visible satellites	5	7
Maximal visible satellites	11	12
Mean GDOP	2.73	2.24

Table 3.20: Simulation numbers from Trimble software for the current GPS constellation.

However, for proper comparison, it was necessary to reproduce the constellation using the same data that was used to generate the numbers in Table 3.19. This yielded the results shown in Table 3.21.

Value	**15 degree mask**	**10 degree mask**
Minimal visible satellites	4	4
Maximal visible satellites	11	11
Mean GDOP	3.77	2.67

Table 3.21: Simulation numbers from Trimble software using the same data used for Table 3.19.

The similar trend regarding the drop in DOP in both Wu et al. and the simulator, in addition to the confirmation of the simulator numbers by the Trimble software as shown in Table 3.20 and Table 3.21, seem to validate the original simulator results.

3.7.3 Galileo Signal Structure and Frequencies

The Galileo constellation signal structure is separated into five major components, each linked to a particular service area. First amongst these is the Open Service (OS), the free service accessible by any member of the public. Galileo will also provide a Commercial Service (CS), which as its name implies will be for use by industry. Also included in the Galileo specification is the Public Regulated Service (PRS) which will be a restricted service for use by governmental agencies or public safety agencies. Galileo's Safety of Life (SOL) service is similar to the OS, with the addition that it provides a guaranteed level of accuracy, which is monitored. It is intended for use in applications where inaccuracies could lead to fatalities. Finally, Galileo boasts a Search and Rescue (SAR) service.

Galileo will broadcast along a variety of frequency bands. These are the E5a / L5, E5b, E6, E2-L1-E1 and L6 bands [27]. Table 3.22 gives an overview of the services in each frequency band.

Service	E5a/L5	E5b	E6	E2-L1-E1	L6
Open	X	X		X	
Commercial	X	X	X	X	
Safety of Life	X	X		X	
Public Regulated	X	X	X	X	
SAR					X

Table 3.22: Details of Galileo frequency usage.

3.7.4 GPS Interoperability

The use of CDMA is one of the key methods by which Galileo and GPS will be interoperable. By avoiding the repetition of pseudo-random (PR) codes within both constellations (i.e. not having a Galileo satellite use the same PR code as a GPS satellite), both satellites may appear to belong to the same constellation assuming the signal characteristics are similar or identical. This leads to major advantages, as shown in the previous sections.

3.7.5 Conclusions Regarding Galileo Deployment

In this section, the impact of the deployment of the Galileo constellation has been briefly covered. The expected layout of the Galileo constellation itself was detailed and its future signal usage considered.

The advantages gained by the presence of thirty additional satellites has been simulated. Typically, the number of visible satellites in Southampton has been doubled, and this has been accompanied by a drop of approximately 25% in the mean value of GDOP, leading to a proportional reduction in the error associated with DOP. This has also been shown to be true in Tokyo as shown earlier. In addition, the Galileo constellation, due to the use of multiple frequencies for the OS, provides users with an improved way in which to solve the integer ambiguity. For high-precision applications, a rapid and accurate method by which to solve this problem is highly desirable.

3.8 Summary

In this chapter, the results of the theoretical simulation conducted over the course of this project has been detailed. Particular attention was paid to the ship simulators, which were the foundation of the practical work that is presented in the following chapter. It was found that given sufficient accuracy from the receiver networks, it is possible to obtain structural deformation information about a vessel. Additionally, the use of frequency analysis allows for a certain degree of separation of the individual motions.

This chapter also included a section regarding the predicted impact of the upcoming Galileo constellation. It was found that the minimal number of visible satellites was increased, and that a drop in DOP also occurred. This directly translates into an increase of confidence regarding the potential implementation of a GNSS-based ship monitoring system.

Chapter 4

Experimental Results Onboard *Red Jet 4*

4.1 Introduction

Following the obtention of positive simulation results, it was decided to attempt to implement a monitoring system on a small scale. It was clear from the onset of this portion of the project that this would be a difficult endeavour due to the limitations of the quality of the equipment which was available for use. However, as will be shown, some positive results were obtained during the practical work. This section explains the experiments that were conducted over the last year of the project and the results that were obtained. It begins by briefly describing *Red Jet 4*, the ship onboard which the experiments were conducted. The rigs which were used in the experiments are then described. This is followed by a presentation of the results that were obtained, and the difficulties which were encountered over the duration of the work.

4.2 *Red Jet 4* and its characteristics

Red Jet 4 is the newest catamaran-type high-speed vessel purchased by the Red Funnel Group who operate a ferry service between Cowes, located on the Isle of Wight, and Southampton located on the mainland portion of the UK. *Red Jet 4* is a passenger-only craft. She was ordered in 2001 and its keel was laid the same year. Red Funnel took delivery of the ship in 2002.

The vessel's cruising speed varies depending on the state of the sea at the time of sailing, but it is capable of reaching speeds of approximately 40 knots (1 knot is

1 nautical mile per hour) in calm seas. Additional characteristics of the ship can be found in Table 4.1. A picture of the ship itself can be seen in Figure 4.1.

Figure 4.1: *Red Jet 4* — This image is courtesy of the Red Funnel Group.

Parameter	**Value**
Length extreme [m]	39.825
Length at waterline [m]	35.780
Beam (moulded) [m]	10.82
Beam (depth) [m]	1.30
Keel draft at full load [m]	1.30
Passenger capacity	275
Usual number of crew members	3
Estimated deadweight at full load [tons]	29.305
Displacement [kg]	97,000
Engine type	MTU V12 4000
Total power [bkW]	1740

Table 4.1: Characteristics of *Red Jet 4*. [41]

Prior to installing any equipment onboard *Red Jet 4*, the simulator that was presented in the previous chapter was utilised to calculate the ship's natural frequencies. The results are shown in Table 4.2.

However, these results are not completely accurate for a number of reasons, the most important of which being the construction of the ship. Unlike most vessels which are currently sailing, *Red Jet 4* has a dual-structure construction. The passenger cabin is a superstructure which is mounted onto the ship's hull as shown in Figure 4.2. This particular type of constructions alters the natural frequencies, and,

Bending Mode	**Natural Frequency [Hz]**
Transversal Mode 1	19.4431
Radial Mode 1	157.7513
Axial Mode 1	64.43
Torsion Mode 1	45.5589
Radial / Axial Modes	>27.5788

Table 4.2: Natural Frequencies of the different bending modes of *Red Jet 4* as predicted by the MATLAB simulator.

unfortunately, the simulator was not designed to work with twin-structure construction. However, the results shown in Table 4.2 were taken as a starting point.

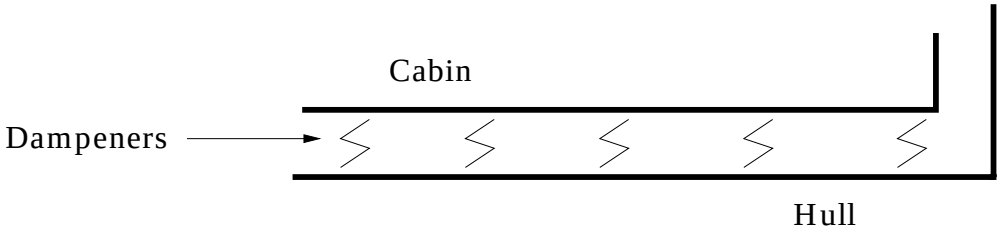

Figure 4.2: Diagram showing the construction of *Red Jet 4*'s passenger cabin. It is mounted upon dampeners which are fixed on the hull.

According to the Red Funnel engineers, this twin-structure construction was selected with passenger comfort in mind, and annecdotal evidence collected from passengers, crew and the company's engineering teams would seem to suggest that the aim was at least partially achieved. However, first-hand experience of heavy seas during the data collection showed unequivocally that passengers can still be subject to very uncomfortable journeys, which could be compared to amusement park "rides".

On most days, *Red Jet 4* sails to and from Southampton or West Cowes every thirty minutes. A typical crossing lasts approximately twenty-three minutes and most of it takes place in the sheltered areas of Southampton Water. However, a portion of the crossing takes place in the Solent, and this is where the ship may be subjected to very heavy seas. The path of a *Red Jet 4* crossing can be seen in Figure 4.3.

A subset of this data can be seen in Figure 4.4. In this figure, the direction of travel is from the North-West to the South-East. At the times shown here, the ship is located in Southampton Water and is just about to enter the Solent. The dataset shown here is unfiltered and uncorrected for RFI.

Figure 4.3: Path of *Red Jet 4* during a typical crossing as measured by the GPS rigs. The smaller of the waterways is Southampton Water whereas the larger one is the Solent.

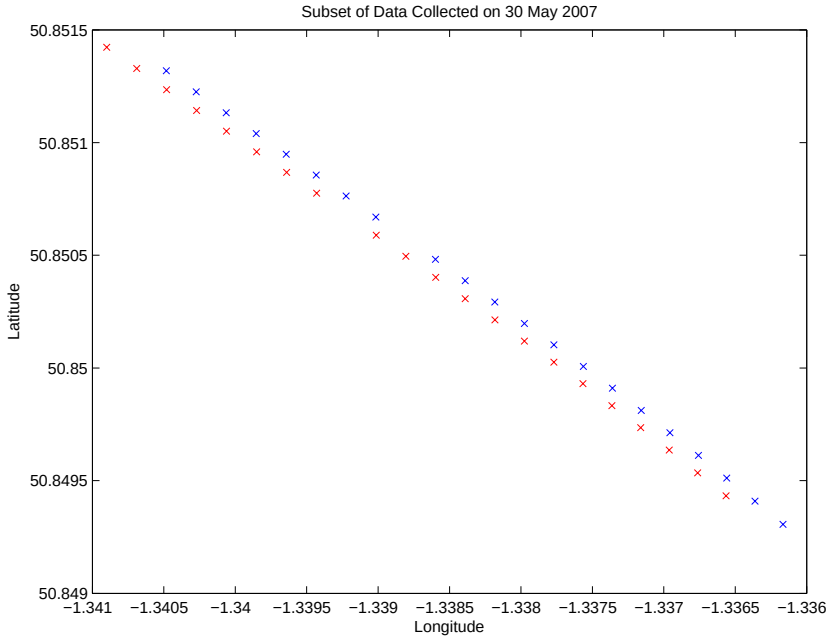

Figure 4.4: Subset of the data collected on 30 May 2007 to test how well the receivers measured the distance separating them. This figure shows the relative positions of the receivers during a single crossing from Southampton to Cowes. The blue and red crosses are the bow and stern receivers respectively.

4.2.1 Consequence of Nyquist's Sampling Theorem

In a number of applications, the sampling rate of the data is of paramount importance. This is as a direct consequence of Nyquist's sampling theorem which, in its simplest form, states that one can only fully recover data containing a range of frequencies from a DC offset to N Hz if it is sampled at a rate higher or equal to $2N$.

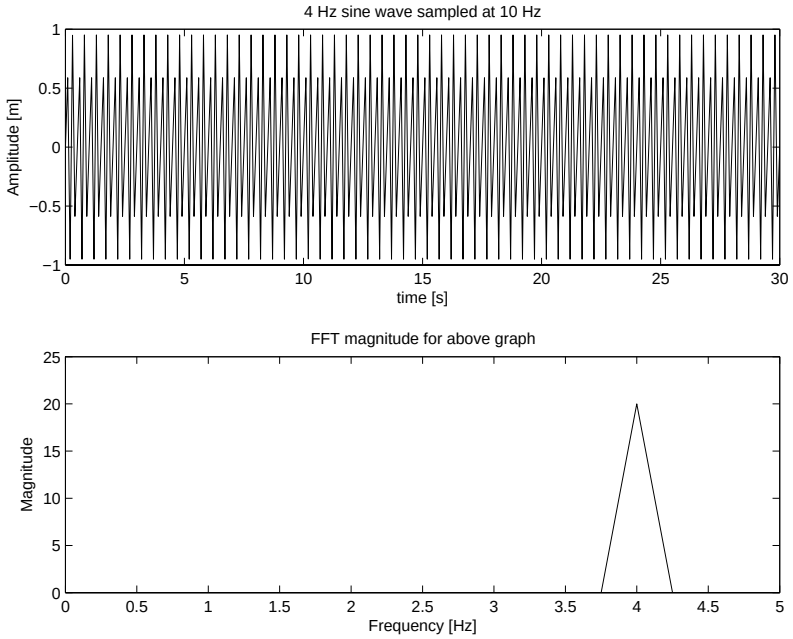

Figure 4.5: Top graph: A 4 Hz sine wave sampled at 10 Hz. Bottom graph: FFT magnitude of the top graph.

The consequence of violating Nyquist's theorem and attempting to sample a high-frequency signal at low-frequencies is a phenomenom known as as aliasing. Consider Figure 4.5. In this figure, the 4 Hz signal is sampled at a rate of 10 Hz, and a twenty point FFT is performed on it. The result is a clean triangular spike centered at 4 Hz. This result would be an impulse at 4 Hz if an infinite sampling frequency and FFT window were used.

Now consider the graphs in Figure 4.6. In the top graph, the 4 Hz signal is sampled at a rate of 3 Hz, in violation of Nyquist's theorem. A twenty point FFT is also performed on this graph, but the result is useless, a consequence of aliasing.

Nyquist's theorem has an important consequence for the practical experiment described. In Table 4.2, the natural frequencies of the flexion movements of *Red Jet 4* are shown. The lowest frequency in this table is approximately 19.4 Hz, a much higher value than would be expected on a large tanker or cargo ship. Thus,

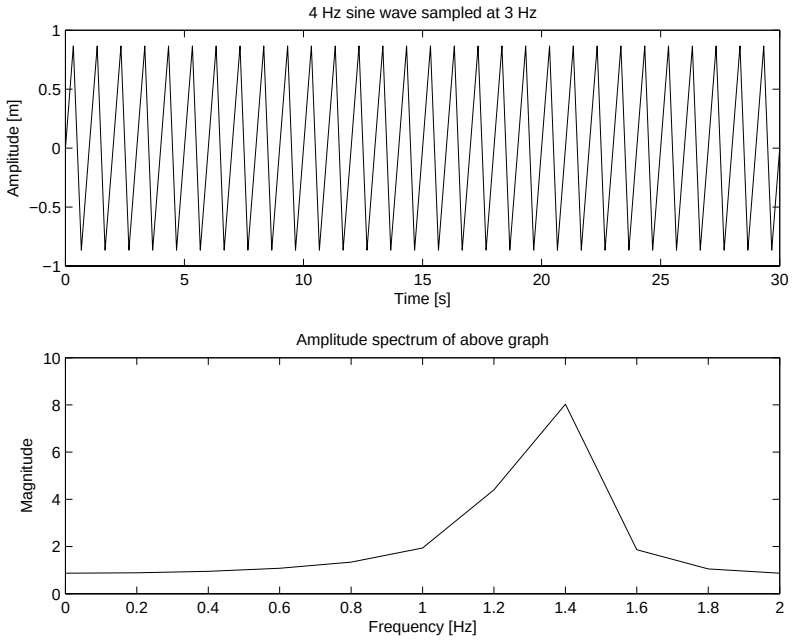

Figure 4.6: Top graph: A 4 Hz sine wave sampled at 3 Hz. Bottom graph: FFT magnitude of the top graph.

according to Nyquist's theorem, it would be necessary to sample at a minimum rate of 38.4 Hz for this motion to be reconstructed. If one wishes to sample the radial motion, it would be necessary to sample at a rate exceeding 300 Hz.

The receivers that were available for use in the practical experiments were limited to sampling rates of 20 Hz. As a consequence, the maximum frequency which could be reconstructed is 10 Hz. This unfortunately limited the scope of the practical experiments to monitoring the ship's rigid body motion.

4.3 The Experimental Rigs

In this section, the experimental rigs, which were designed specifically for this project, and, installed onboard *Red Jet 4* are described. Due to the harsh conditions that might be experienced onboard a passenger craft operating in seawater, extra care had to be taken to protect the electronic equipment. It was thus decided to enclose the rigs into an Immersion Protocol (IP) type-66 box. These boxes are watertight under temporary immersion conditions, and thus protect the equipment from both water and the ship's exhaust in the case of the stern rig.

Each rig was composed of an Ashtech G12 single frequency (L1) carrier-phase GPS receiver, one MaxStream ZigBee radio-modem and a 12 Volt battery. The re-

ceiver was remotely controlled using custom software written for a laptop running the Linux operating system. A block diagram of the setup is shown in Figure 4.7. Figure 4.8 and Figure 4.9 show the rig installed on *Red Jet 4*'s bow and the inside of one of the IP66 boxes respectively.

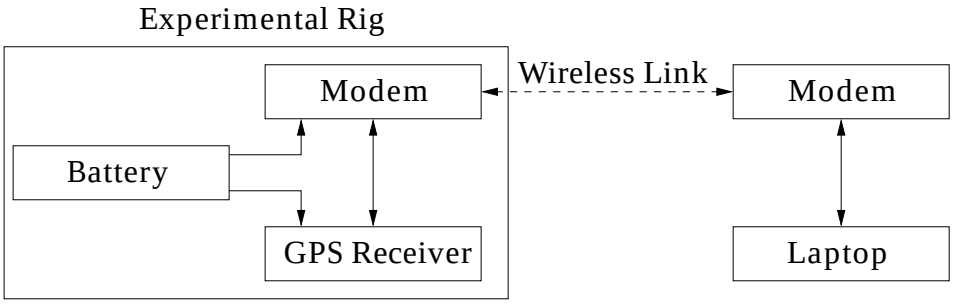

Figure 4.7: Block diagram of the rig and computer setup used onboard *Red Jet 4*.

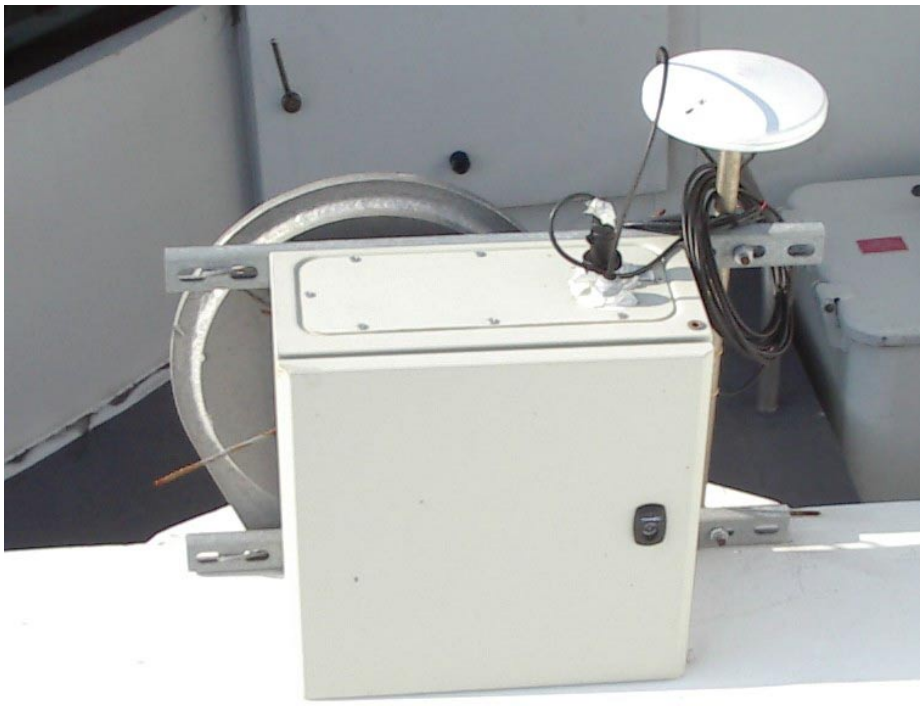

Figure 4.8: The experimental rig installed on the bow, port side, of *Red Jet 4*. The rig is tied down to a lifting crane ring using steel cable.

The radio-modems were a late addition to the setup. The original plan called for the rigs to be physically wired to the portable computer inside the passenger cabin. This plan had to be abandonned due to Maritime and Coastguard Agency (MCA)

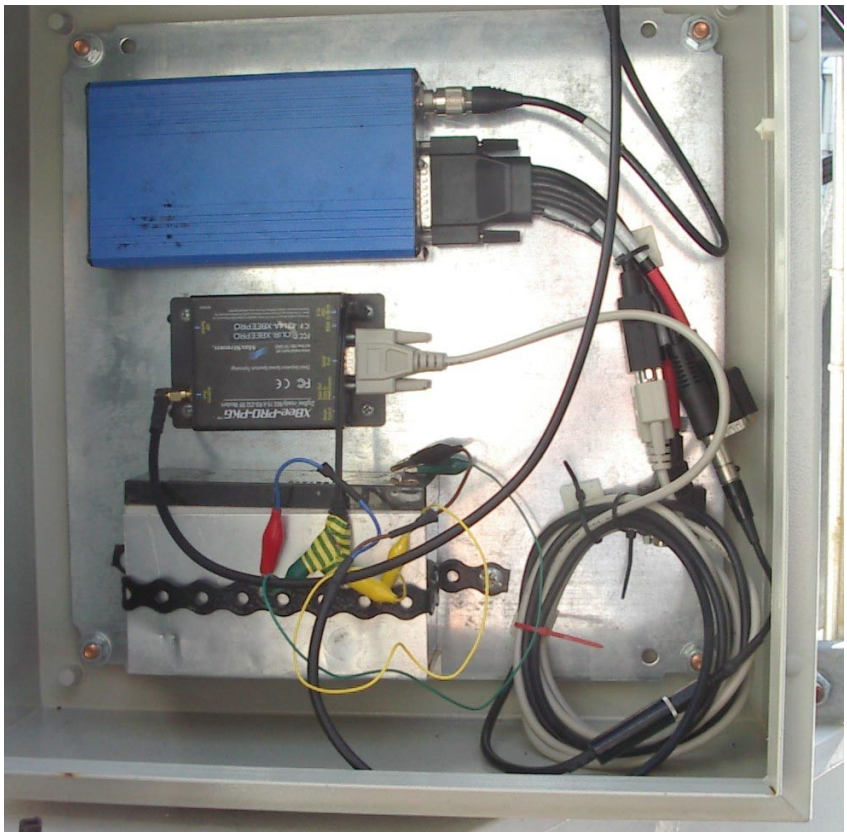

Figure 4.9: Inside the type-IP66 box. From top to bottom on the left side can be seen the G12 GPS Receiver, the ZigBee Radio-Modem and the 12 Volt Battery.

regulations and concerns over passenger safety as data collection took place during actual crossings. Additionally, the Red Funnel engineers voiced some concerns over the feasibility of installing the wiring inside the passenger cabin.

Due to the natural frequencies that were calculated for *Red Jet 4* using the MATLAB simulator presented in the previous chapter (these results are shown in Table 4.2), it was decided to concentrate the practical work on rigid body. In order to be able to make measurements on both pitch and roll, the rigs were placed at the locations shown in Figure 4.10.

4.3.1 Ashtech G12 L1 Carrier-Phase GPS Receiver

The main piece of equipment utilised in this research was the Ashtech G12 single-frequency (L1) carrier-phaser GPS receiver. The particular receivers which were used in the experiments were at least five years old, and, as such, have not benefited from the more recent advances in technology. The earliest versions of the G12 receivers used during this project date back to 1996, prior to the permanent

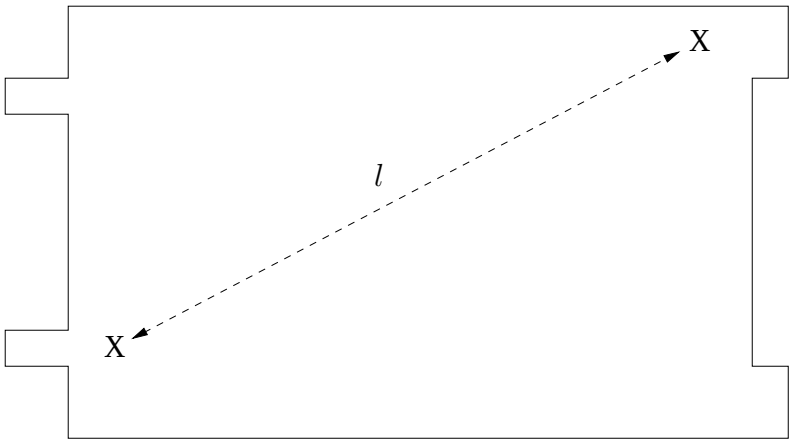

Figure 4.10: Top-view of *Red Jet 4* showing the rig locations. The baseline length, l, is 34.07 metres.

disabling of the Selective Availability (SA) technology[1] ordered by USA President Bill Clinton in May 2000.

According to the G12 user manual [31], this particular receiver is capable of location a user with an accuracy of 16 metres when PDOP is lower or equal to 4. The G12 receiver broadcasts information through one of two serial ports. This information can be broadcast within a variety of messages, using different transmission speeds and a variety of sampling rates, ranging from $\frac{1}{20}$ Hz up to 20 Hz. For the purposes of these experiments, the data from three messages was collected. These are referred to as the MCA, PBN and SNV messages by the receiver [31], and this terminology is used for the remainder of this document.

The first of these, the MCA message, is thirty-seven bytes long and contains information about individual satellites for the specific epoch, including but not limited to pseudo-range and satellite "health" information. One MCA message per satellite that the receiver has a lock on is broadcast every epoch.

The second of these, the PBN message, is fifty-six bytes long and contains general information about the receiver's current location and motion, as calculated internally by the receiver. The PBN message also contains timing information. It is using the information contained within the PBN message that the experimental rigs were synchronised. One PBN message per receiver per epoch is broadcast.

The third message, the SNV message, is one hundred and thirty-two bytes long and contains ephemeris and timing corrections for each individual satellite. A maximum of one SNV message per epoch per receiver is broadcast. As the receiver may

[1]SA technology allows the USA armed forces to severely limit the accuracy of the GPS system. Although no longer in use, the USA retains to ability to re-implement the denial of accuracy at any time.

track up to twelve satellites at a time, it may take up to twelve epochs to be in possession of the full set of ephemeris coordinate information. Additionally, as the satellites receive updates from the ground control station, they broadcast a new set of ephemeris coordinates. The receiver will broadcast a new SNV message for each satellite when this occurs. First-hand experience has shown that a new set of SNV messages is broadcast approximately every fifteen minutes.

4.3.2 MaxStream ZigBee Radio-Modem

The MaxStream ZigBee modems were used as repeater devices due to the fact that it was not practical to wire the receivers directly to the computer. The ZigBee modems came in two varieties: RS-232 and USB. The USB variant was connected to the portable computer, whereas the RS-232 was connected to the experimental rigs. This was done to take advantage of each device's characteristics.

The modems operate on the 2.4 GHz unregulated frequency and utilise Quadrature Phase Shift Keying (QPSK) modulation. The Equivalent Isotropically Radiated Power (EIRP) is capped at 100 mW at full power, giving the modems a line of sight range of one statute mile. However, due to European regulations, the modems had to be operated with reduced EIRP of 10 mW.

The modems are capable of symbol rates of up to 115,200 baud per second and data rates of up to 250,000 bits per second. For simplicity, the modems were configured to operate at a rate of 9,600 baud per second, which is the default symbol rate of the receivers.

4.3.3 Control and Data Acquisition Software

The experimental rigs were remotely controlled using custom software written for the Ubuntu distribution Linux operating system in the C and C++ programming languages. The Linux operating system was chosen due to the ease with which data can be written to and from USB ports when compared with Microsoft's Windows series of operating systems. The computer utilised during the experiments was a Pentium 4 Toshiba Satellite portable computer with 512 MB of active memory.

4.4 Experimental Preparation

In this section the results that were obtained onboard *Red Jet 4* under various conditions are presented. This section first begins by describing the verification ex-

periments that were conducted to ensure proper functioning of the rigs. This is followed by the presentation of results from several runs. These were conducted under various conditions from flat calm seas to heavy seas in gale force winds on the Beaufort scale. In the Beaufort scale, gale force winds are those ranging from Force Seven (51-62 km / h, 28-33 knots) to Force Nine (76-87 km / h, 41-47 knots). However, during the data collection period, *Red Jet 4* never operated at times during which wind speeds were in excess of Force Eight (63-75 km / h, 34-40 knots). In fact, service on both passenger-only craft and vehicle transportation vessels was suspended on two days where sustained Force Nine winds were recorded in the Solent in January 2007.

4.4.1 Rig Verification

The first step of the verification process was to ensure that the radio-modems were operating satisfactorily under reduced power and poor line of sight (LOS) conditions. Multiple locations for the rigs were tested before the final location, shown in Figure 4.10, was determined.

At the locations shown in Figure 4.10, it was found that reception from the bow modem antenna ranged from -40 dBW to -55 dBW as measured by driver software provided by MaxStream. However, due to the poor LOS conditions at the stern, reception was extremely poor and was measured at -90 dBW or worse by the MaxStream software. A change in modem aerial location was necessary in order to improve reception. After this change in position, reception improved to between -50 dBW and -60 dBW. It was further found that a power reading of -60 dBW was the absolute minimum for data reception from the modems to be successful.

Once range testing was completed, the next test was to verify position tracking using the raw information provided by the receiver's PBN message. The results were superimposed onto the satellite image shown in Figure 4.3. This was the path taken by *Red Jet 4* during the 1115 crossing from Southampton to West Cowes on 30 May 2007. It is fairly representative of a typical crossing although the path can vary significantly depending on traffic, weather, and other advisories in force at the time as Southampton is one of the busiest commercial ports in England. In this particular crossing, a wide berth was given near the Foley oil refinery (which is the built-up section on the left side of the satellite image) due to repair work on one of the docks which had been demolished due to an oil tanker colliding with it.

4.4.2 Accuracy of the G12 Receiver

In this section, the result of static runs that were utilised to verify the accuracy of the G12 receiver are presented. Unfortunately, it was found that the data obtained using these receivers was actually quite poor in quality and that the desired accuracy would most likely not be achieved. All the data utilised here was taken while the ship was moored in port on 4 June 2007.

Given the type of experiment that was going to be conducted during actual crossings, the key measure was the accuracy of differential measurements to be taken using the G12s. The simple test of trying to determine the distance is what was conducted here, and it was taken as a reflection of the accuracy of the receiver itself. Figure 4.11 shows a typical graph obtained, including the major distance variations obtained. The error figures for the entire day are shown in Table 4.3.

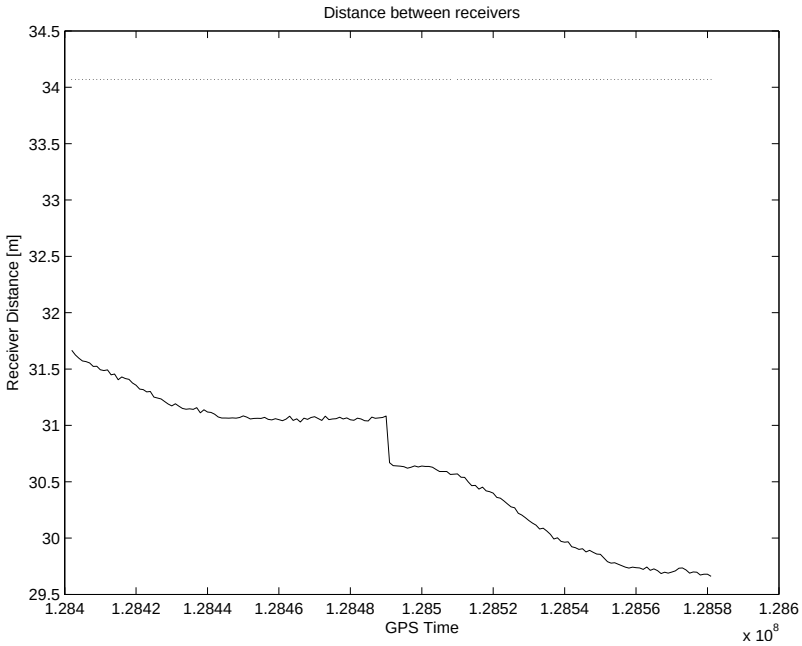

Figure 4.11: Sample distance between receivers on 4 June 2007 while docked. The solid line is the calculated distance and the dotted line is the actual baseline length of 34.07m. The duration of the experiment is three minutes and the units of time are in milliseconds.

Although these results are well within the predicted performance of the G12 receiver, they are insufficient for the purposes of structural deformation. Additionally, it was unlikely that the necessary level of accuracy would be achieved by the use of this particular equipment.

Parameter	Value
Actual Baseline Length	34.07 [m]
Smallest Calculated Baseline	26.37 [m]
Longest Calculated Baseline	34.00 [m]
Mean Calculated Distance	31.19 [m]
Standard Deviation of Calculated Distance	1.366 [m]

Table 4.3: Accuracy data for the 4 June 2007 accuracy tests.

4.4.3 Radio-Frequency Interference

During the verification phase, it was also discovered that the data contained a fair amount of radio-frequency interference (RFI) from onboard systems, specifically the ship's radar. An example of such a figure is shown in Figure 4.12. In this graph, instances of RFI are represented by the cycle count dropping to zero for a very short period of time, usually one epoch.

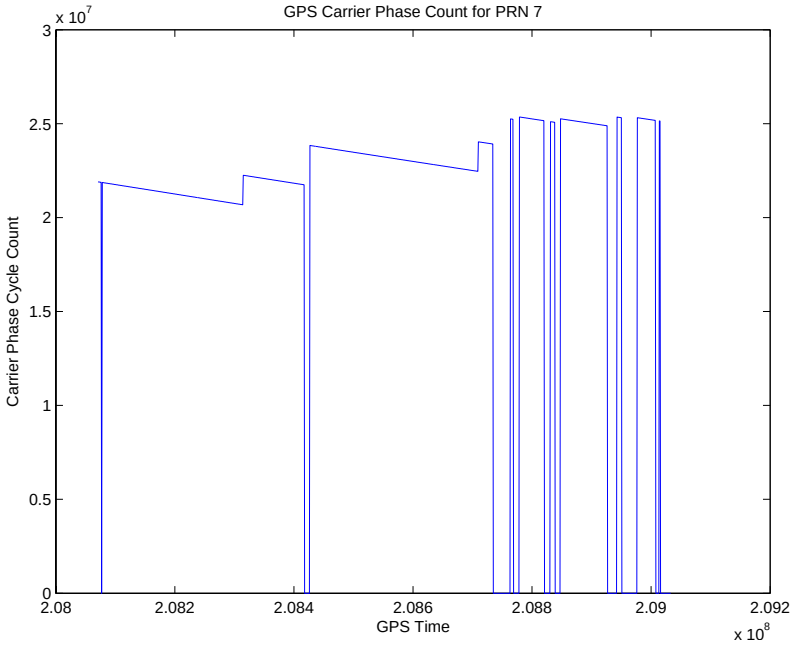

Figure 4.12: Cycle count for PRN 7 satellite during a crossing from West Cowes to Southampton at 1045 on 3 July 2007.

Given the relatively high occurence of such RFI drops, it was decided to attempt to write a correction algorigthm for the RFI occurences. This algorithm only attempted to correct RFI and not cycle slips, the latter of which can also be seen in Figure 4.12. It was noticed that the count curves appear near-linear, as they are in fact very shallow exponential curves, and thus a very simple interpolation algo-

rithm was utilised. The result is shown in Figure 4.13. Cycle slip occurences are also far more obvious in the corrected graph.

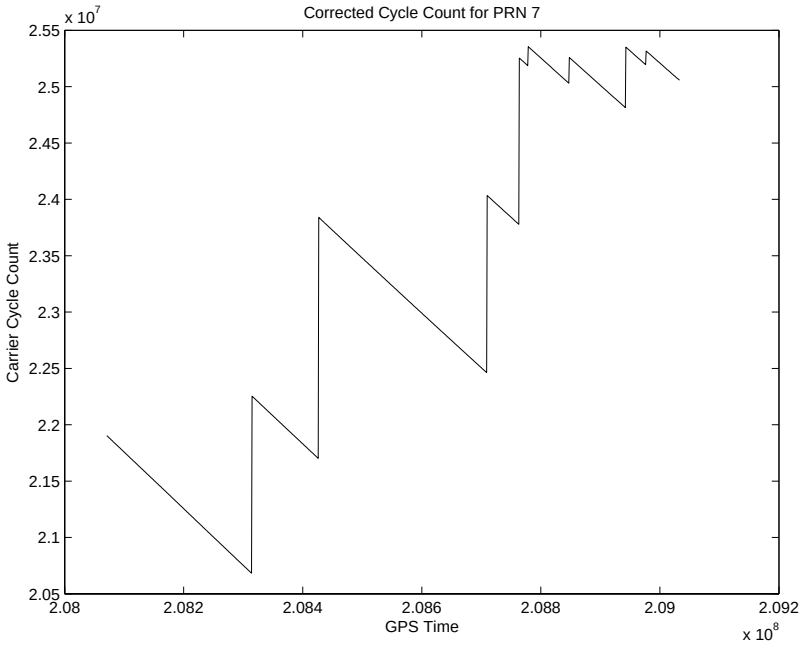

Figure 4.13: The graph of Figure 4.12 with RFI correction algorithm applied.

There is a further additional complication within this data and it is due to the G12's clock. The clock resets when a difference of 1 ms or greater than the satellite clocks is detected. This gives the data a sawtooth appearance as shown in Figure 4.14.

The data from every satellite as measured by a single receiver is affected in the exact same manner at the exact time by the clock reset, making it easy to identify. However, the data from different rigs may not suffer the clock reset at the same time, which could (and did) cause some synchronisation issues.

4.5 Experimental Results

Nonewithstanding the above problems, it was decided to attempt the experiment. The setup described above was used in an attempt to track rigid-body motion of *Red Jet 4* in various sea states. For the purposes of this experiment, this consisted of tracking pitch and roll of the vessel during several crossings. As was the case for the simulation results presented in Chapter 3, a subset of the data was chosen for presentation here as several days worth of data was collected.

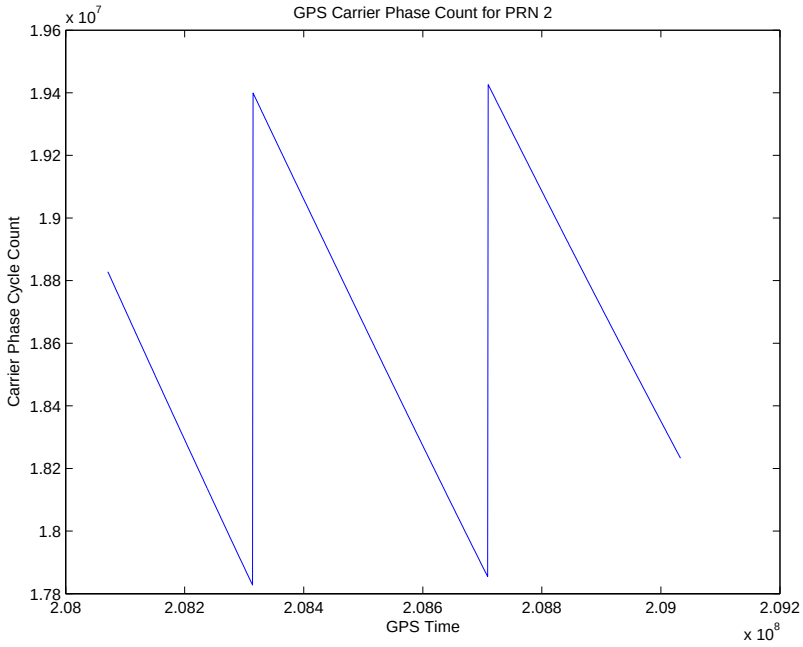

Figure 4.14: Effect on the cycle count of the G12 clock reset.

4.5.1 Data Processing Sequence

All data processing for the experimental was done several days after the experiment was actually conducted on the ship. It took part in a two-step process, the first of which was parsing the binary data files that were generated by the receiver. This step was conducted by using a C++ program under the Linux operating system.

This program accomplished the following steps:

- Extracted the data from the receiver's binary format.
- Created a data file where all SNV data appeared first in the file, followed by the MCA and PBN from each epoch.

This data was then imported into MATLAB which generated the information presented in this section. This MATLAB script ultimately calculated the rigid body motion in the form of pitch and roll. Additional information could be generated by the software, and some of it is included later in this section.

4.5.2 Results from Collected Data

On most days, the crossings were conducted in smooth or very calm water. By definition, very calm or smooth seas are those in which there may be only very

small ripples, these having a height of less than half a metre. For all these sailings, there were no heavy or unexpected movements during any of the crossings. Thus, it would be expected that most of the data would be close to a "flat line" for both pitch and roll. However, it proved to be quite the opposite. A sample result is shown in Figure 4.15. This comes from a crossing where slight to moderate motion was experience in the open portion of the Solent (the southern part of the crossing as seen in Figure 4.3).

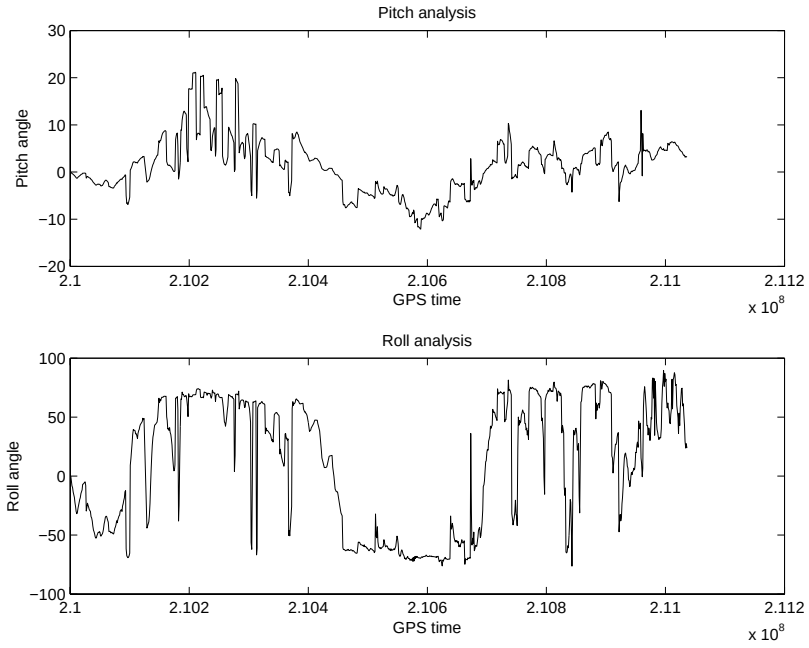

Figure 4.15: Sample result for the pitch and roll of *Red Jet 4* on a typical crossing. Both pitch and roll figures are given in degrees. Negative pitch indicates the bow pointing into the ocean, whereas negative roll indicates the ship is rolled to port.

As can be seen in this figure, the ship is supposedly subjected to extreme motions, but this was not the case. Even in the portion where the ship was exposed, the motions were nowhere as violent as indicated in the roll diagram, which seems to indicate that the ship spent most of the crossing angle by fifty degrees either to port or starboard. However, what is interesting to note is the values of the pitch shown.

Approximately two minutes into the crossing, at the time which the ship would have entered the Solent after leaving Cowes, the ship begins to show a slight pitching motion which lasts for about 300 seconds, or five minutes. However, instead of the system showing that the pitching motion has stabilised or ceased once the ship entered Southampton Water, the GPS receivers seem to continue producing data that indicates a continued motion, although not as heavy as that experienced in the

Solent.

Most of the data that was collected showed that the ship was subjected to heavy motion while in the Solent only, but did not stabilise when the ship was in Southampton Water, countrary to what occurred in reality. More worrying is that in most cases, the data showed that heavy motion occured at all points during the crossing. Some of the motion recorded by the dataset was extreme in nature. Any attempt at filtering was met with failure due to the extreme motions encountered in the data.

It is encouraging that the receiver networked picked up heavy motion at the moment when the ship crossed into the Solent, and was exposed to moderate to heavy winds, usually from the South-West, and the waves that this wind churned up. However, in differential operation, such as what was attempted here, the G12 is supposedly capable of accuracies of the order of 40cm or better [31]. Unfortunately, this accuracy was not achieved during the course of this experimentation. Several causes were considered including the length of the baselines, the receivers themselves and RFI to name but a few.

It was initially believed that the cause for the lack of accuracy could be explained by one of the matrices used to solve for the user's position being singular or nearly so. This was quickly shown not to be the case. Any other attempts at solving this data problem with various types of filters were met with failure, or removed most of the information from the dataset, making the information worthless.

4.6 Conclusion

Regrettably, the lack of accuracy that was obtained in this portion of the work means that it was impossible to validate the simulator results that were shown in Chapter 3. This is a major setback, and another set of field work will need to be undertaken to validate the results obtained in simulation. However, this future set of work should be conducted on a much larger vessel than *Red Jet 4* in order to ensure that the sampling rate of the receivers is sufficiently high to be able to measure the bending modes, which on a larger ship will be at lower frequency.

Chapter 5

Conclusions and Recommendations

5.1 Introduction

In this chapter, the results presented in the previous two chapters are discussed and some further analysis is done. This analysis is specifically aimed at putting the work into context of the objectives of the project which were introduced early in this document. The chapter concludes with recommendations for future work which could come as a result of this project.

5.2 Objective One — The Required Accuracy

The first objective:

"Determine the accuracy required from a GPS system for structural analysis of a vessel"

had to be considered very early in the project in order to determine if it such a system was even theoretically possible. The simulator in Chapter 3 was implemented at first specifically to deal with this question. And it was difficult to answer. This is due to the fact that the requirement on different ships may be drastically different.

For example, the larger ships may have a flexible body motion having an amplitude of several metres [25], whereas a small ship like *Red Jet 4* may have motion in the order of a few centimeteres or less. Additionally, the error on the GPS can dramatically alter the motion that can be detected.

Thus, the simulator from Chapter 3 was reworked slightly in order to do error-analysis as well. This version of the simulator looped repeatedly increasing the amplitude of Mode 1 bending for a specific level of error. For each amplitude, the simulator then calculated the SNR by determining the mean noise level and the

peak caused by the bending mode. This is not the worse case scenario. For this, it would have been necessary to conduct this analysis using maximal error level.

A number of error-analysis runs were conducted, with the amplitude raising in 1cm increments in the range of 1cm to 5m and the SNR calculated at every amplitude for a number of different error ranges with 95% confidence ranging from 1cm to 1m on both the horizontal and vertical. The full set of results is shown in Figure 5.1.

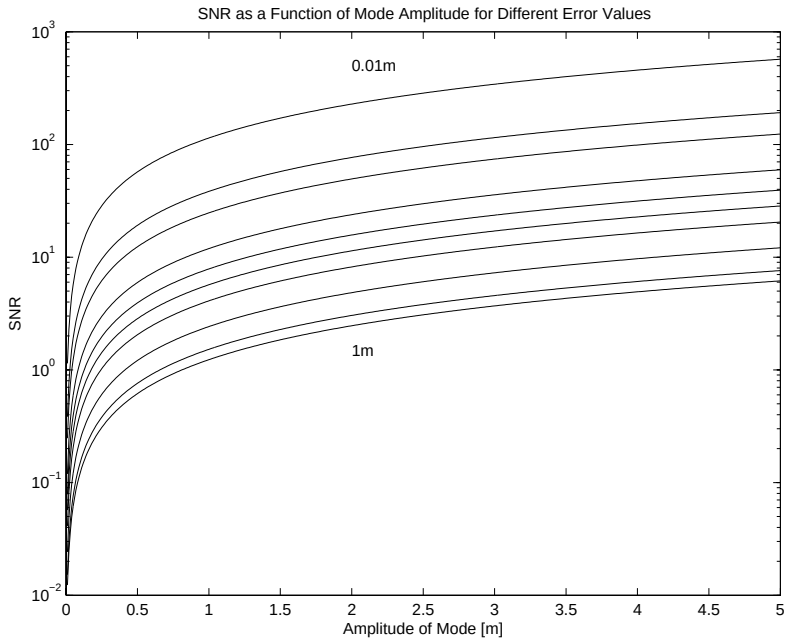

Figure 5.1: SNR for different amplitude levels at varying error rates. GPS error bounds are within 0.01m (highest line), 0.03m, 0.05m, 0.1m, 0.15m, 0.2m, 0.3m, 0.5m, 0.75m and 1m (lowest line) 95% of the time.

The most interesting part of this result is the section where the amplitude of the mode is between 1cm and 15cm. This portion of the graph was expanded upon and is shown in Figure 5.2.

Using this graph, and knowing what SNR is desired, it is but a simple matter to determine the error level that can be tolerated. It would also be possible to interpolate for different error levels that were not included in the simulation runs. A question remains as to what would constitute a “good” SNR level for this application. Currently, it is believed that a minimum 1:1 ratio is required for this operate without resorting to error correction or any other encoding methods. However, should filtering be in use, then it may be possible for the system to operate at a 4:5 SNR. The SNR tolerance levels would need to be verified by future practical work.

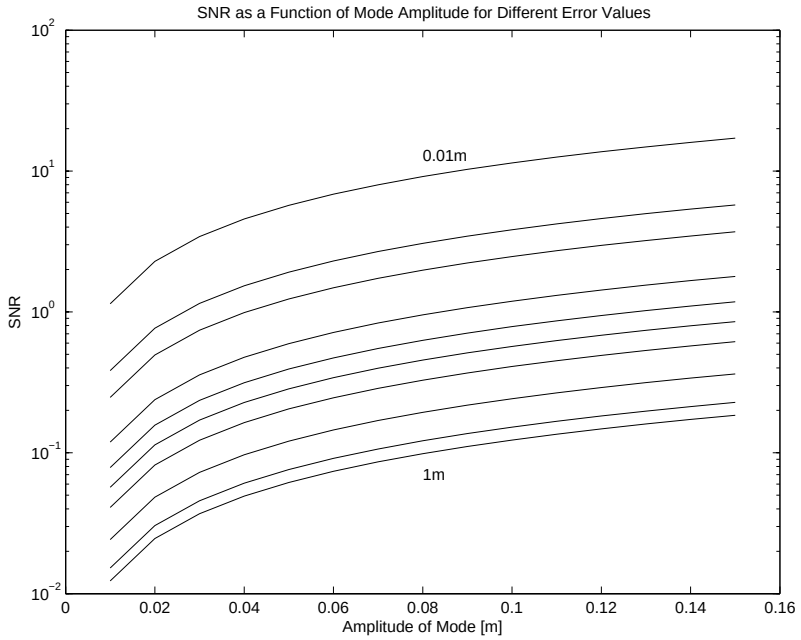

Figure 5.2: Expanded graph of Figure 5.1 where the amplitude of the mode is limited between 1cm and 15cm.

5.3 Objective Two — Determination of Forces

The second objective:

"Develop real-time processing algorithms to analyse dynamic loads applied to a ship using the output of the GPS receivers"

has been partially achieved. The problem with this particular objective does not lie with the calculations involved as these are fairly simple once the position of the GPS receivers has been established with certainty. What has yet to be completed is the real-time portion of the work as currently all the data is post-processed.

According to beam theory, the maximal stress at a point in a pipe as is used in this project, can be determined using:

$$\sigma_{max} = \frac{My}{I_{xx}} \tag{5.1}$$

where M is the bending moment, y the radius of the pipe, and I_{xx} the second moment of area.

Beam theory further provides that:

$$\frac{\sigma}{y} = \frac{E}{R} \tag{5.2}$$

where R is the radius of curvature of the beam and E is Young's modulus, a constant which depends exclusively on the material of which the beam is constructed. This project used steel, which has a Young's modulus of $E = 210GN/m$. The above equation can be rewritten to be:

$$\sigma = \frac{Ey}{R} \tag{5.3}$$

The only unknown variable in the above is the radius of curvature at a point on the beam, but this can be determined using the method of three points on a circle. This is the method of choice for this project.

The simulator from Chapter 3 was modified in order to complete these calculations. Figure 5.3 shows the maximal stress experienced at any point onboard the vessel for the amplitudes shown in Table 5.1. These amplitudes seen in this table were believed to be extreme in nature, and this will be clearly demonstrated by the calculation of forces. The amplitudes represent the maximum vertical distance between any point in the beam.

Movement	**Amplitude [m]**
Bending mode 1	2
Bending mode 2	1
Bending mode 3	0.3
Bending mode 4	0.05

Table 5.1: List of amplitudes used to generate the stresses in Figure 5.3.

In this case, as expected, the stresses experienced by the vessel are extreme and range into the GPa order of magnitude. The yielding strenth, or the maximal stress tolerance of a material is usually much less than 1GPa, but this can depend on the material involved, the grade of the material and other factors. Notwitstanding this, it is clear that under conditions where giga-pascal stresses are experienced, it is likely the ship would be severely damaged or even lost in transit. Modifying the construction of the vessel and doubling the hull thickness from 1cm to 2cm made no impact on the stresses involved as expected from the previous equation due to the fact that the simulator imposes a deformation not a load. There was a change in the natural frequencies caused by the corresponding change in the second moment of area.

However, considerable impact was obvious when the amplitudes of the motions were reduced. Using the amplitude figures shown in Table 5.2, maximum stress experienced dropped below 700MPa. Although this stress range is within the allowable range for some steel alloys, these alloys are not used in ship construc-

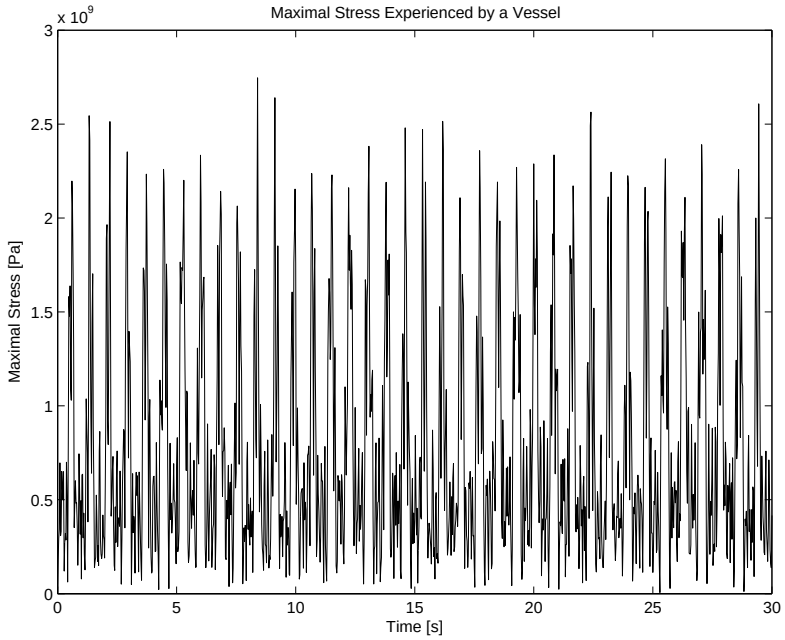

Figure 5.3: Maximum stresses experienced by a vessel during a simulation run.

Movement	Amplitude [m]
Bending mode 1	1
Bending mode 2	0.5
Bending mode 3	0.15
Bending mode 4	0.025

Table 5.2: List of natural frequencies and relative amplitudes used to generate Figure 3.37.

tion due to their high cost. The standard steel used in ship hulls has a much lower stress tolerance. In addition, the size of the receiver network had to be increased significantly for this data to be collected. This was necessary in order to properly track the deflection of the vessel in response to the sea state. Unfortunately, this brings this objective into conflict with the third objective.

Additionally, in this section is seen the difference between reality and the model of the vessel as a pipe that was utilised for this project. In this project, a ship is modelled as a single pipe, several hundred metres long. However, in practice, ships are constructed in divided sections separated by bulkheads. This would have the effect of reducing the stress on each section and allowing for motions that may be far greater than those shown in Table 5.2.

5.4 Objective Three — Determination of Optimal Network Configuration

The third objective:

"Determine the optimal number of GPS receivers required and the preferred location for such sensors to detect structural motion"

has been partially achieved and the analysis that was conducted to complete this objective is shown here. Due to practical limitations on the number of receivers that were available, it was impossible to verify the premise of the project.

5.5 Objective Four — Detection of Damage

The fourth objective:

"Devise means of detecting certain types of stress damages such as plastic deformation"

has been partially achieved. Due to a lack of a equipment, it was impossible to attempt to verify any method that was thought up during this project. This algorithm has been refered to the future work section.

5.6 Objective Five — Data Processing Algorithms

The fifth objective:

"Develop signal processing algorithms to extract additional information, such as heading, pitch, roll and heave, using the output of the GPS receivers"

has been acheived.

The algorithms were used extensively in the simulators detailed in Chapter 3. Unfortunately, as shown in Chapter 4, using them in practice was not as successful, but this had more to do with the GPS receiver, and consequently the dataset, then with the mathematics behind the algorithm.

5.7 Objective Six — Implementation

The sixth objective:

"Attempt to implement a monitoring system on a small scale"

was achieved, however the results did not allow for any significant conclusions.

The idea behind the practical work that was presented in the previous chapter was to support the premise of the project. The difficulties in implementing such a complex system were illustrated, specifically those encountered due to RFI, LOS and health and safety (legal) issues. Although the two latter issues were sorted by careful planning, RFI remained an issue over the entire course of the experiment due to the fact that the ship's radar operated at a frequency that was similar to that of the modems.

5.8 Objective Seven — The Impact of Galileo

The seventh objective:

"Consider the impact of the upcoming Galileo constellation"

has been achieved.

This aspect of the research was limited to theoretical simulation. When the project began in October 2004, it was expected at the time that there would be several Galileo satellites in orbit by late 2007/early 2008 and it had been planned to conduct some trials using these satellites. As of late May 2008, there are only the two testbed satellites, GIOVE-A and GIOVE-B, in orbit and GIOVE-B was only launched on 27 April 2008. The full constellation is not expected to be operational for a minimum of three to four years.

Nonetheless, the theoretical simulation did show that it was possible to achieve some major improvements in satellite geometry when the full constellation is deployed, leading to corresponding gains in accuracy due to the drop in DOP. Additionally, it was found that the results obtained in this portion of the research followed the same trends as those which had been previously published, or were published over the duration of the project.

5.9 Further Recommendations for Future Work

As mentioned previously, the key piece of future work that needs to conducted is validation of the project premise on a medium to large scale. In order for this to be accomplished, a fairly large network of receivers would need to be installed on a large cargo or tanker. It would be advantageous for this network to be comprised of high-end mutli-frequency GNSS receivers to take advantage of the wide-lane

techniques and possibly to take advantage of the multiple frequencies that are (or will be) offered by a rejuvenated GLONASS and the upcoming Galileo.

Returning once again to the list of objectives listed in the first chapter of this thesis, some additional items of future work that were not discussed earlier are listed here. Although it was possible to theoretically calculate the required error levels for a specific SNR in the frequency domain, this was done for a worst case analysis using a fairly simple normal distribution. It is clear that this error model may not be totally accurate or suffer from regional variances, and furthermore may depend on the equipment that is in use for the setup. Variance on the errors are likely to be introduced as the GNSS system expands, and error models will need to be altered to take into account those changes. This may lead to a revision of the graph shown in Figure 5.1.

Following-up on the second objective, although the real-time portion of the work has yet to be completed, it is known that it is possible as shown by Wang et al. [58] in their 2001 paper. Wang et al. implemented a fibre-optics based real-time ship structure monitoring system. Given some of the limitations of the GNSS in terms of line of sight, it would be necessary to model the effect of different constructions on the calculations of strain as it would not be possible to place such a GNSS system directly inside the hull of the ship. Consideration should be given to coupling up a GNSS-based system with a strain gauge or fibre-optic system.

Additionally, solving the conflicting nature of the second and third objective, or at the very least reconciliating them should be considered an important objective of any future work. The conflict ensues from the fact that the third objective aims to have an optimal network configuration, specifically minimising the number of receivers that need to be placed onboard the ship to track motion. However, monitoring deflection over the length of the ship requires the addition of several receivers, thereby causing the conflict. As with most engineering problems, a trade-off will need to be made.

Regarding the third objective, the main piece of future work that needs to be conducted here is verification of the model and of the use of the optimisation function as a means of determining the best possible receiver placements. Should any field trials be conducted, this function should be reviewed and improvements to it made in order to increase the positioning of the network. There is also the question of automating the identification of modes and motions, an analysis which at the present time is being conducted manually.

It will also be necessary to verify the simulation results for the impact of Galileo and update the simulator based on the actual orbits of the satellites once these are

launched over the next few years. Using receivers which are capable of reading signals from Russia's rejuvenated GLONASS and any possible advantages of using FDMA should also be considered. Although all of the above are valid avenues for future research, the key component must remain validating the usefulness of the system.

5.9.1 Proposed Algorithm for Damage Detection

This thesis proposes that the following experiment should be attempted first in any future work endeavour dealing with damage detection:

- Take differential measurements onboard the vessel prior to it being loaded. These would act as reference values.
- Repeat the above process during loading of the ship's cargo. The measurements obtained once the ship is fully loaded would serve as the references values during the particular journey.
- If at any point during the journey, the average measurements made over a period of time, λ, differ by more than a certain tolerance value, κ, then an inspection for damage in the affected areas should be made at the next port of call.
- Should at any point during the journey, the average measurements made over the period of time λ differ by more than a certain critical tolerance value, τ, then an immediate safety check should be carried-out.
- Measurements should be taken while the ship is docked, and during unloading. During unloading the reference should be taken to be as the journey reference until the ship is partially unloaded, at which point the unloaded reference should be taken.
- Once the ship is unloaded, should averaged measurements exceed κ or τ safety inspections should be carried out.

Additional items for future work should include:

- Determining the tolerance values κ and τ. Additionally, determining whether or not these tolerance values should be changed depending on the loading conditions.

- Determining the length of time, λ, over which the measurements are averaged and if the length should be changed depending on the loading conditions. It will also be necessary to consider which measurements will be averaged.

- Validating the method and comparing to models of still-water loading similar to those discussed in [51].

The use of weighing methods to deal with the differences between the loaded and unloaded reference measurements could also be considered if the change in loading impacts the measurements drastically.

5.10 Conclusions

This project aimed to verify the usefulness of a GNSS receiver network at monitoring the structure of a vessel. Previously, the use of the GPS to monitor structures had only been conducted on land using fixed base stations, an option that is clearly not available at sea. Due to the novelty of this project, work had to be conducted on two fronts: Theoretical and Practical.

Most of the theoretical objectives which had been set at the start of the project were achieved. The first piece of simulation seemed to indicated that given sufficient accuracy, a GPS system receiver network system is capable of tracking rigid-body motion of a vessel. Even in a worst-case scenario of uncorrelated error and the receivers locating the user within 25cm horizontaly and verticaly of actual postion 95% of the time, pitch tracking error was no more than 5 degrees at any time whereas roll tracking error did not exceed 10 degrees for the same ship as was used in Chapter 3. However, given the shorter baseline for roll calculation, this was not unexpected.

Extending the simulation to include bending modes yielded positive results as well. For this type of work, it was found that frequency-domain analysis provided much better results due to the ability of being able to distinguish between the different components of the motion. However, there remains some issues with the model due to the simple nature of it. More complex models will need to be considered in any future work in order to gauge more information about the ship prior to setting up the network, otherwise, the receivers may not be positioned correctly onboard.

Simulation results showed some very clear and distinct spikes at frequency where motion should occur, specifically the mode natural frequencies. SNR re-

sults vary depending on the error level of the simulation, but as shown earlier in this chapter, SNR in the frequency domain will be 2:1 or greater for error settings of 1m or less (with 95% confidence) once the amplitude of the mode exceeds 1.75m.

In order for this to be possible, it is necessary that the receivers be positioned correctly. An optimisation function has been proposed for this use. Using the function, several different scenarios were considered, leading to different placements of the network for different purposes. Additionally, simulation work has shown that it is possible to calculate the stress that is exerted on the ship.

The impact of the upcoming Galileo constellation was also considered in the simulation work. For example, the use of the combined constellation leads to an increase of 120% in the number of visible satellites over the city of Tokyo. In Southampton, the GDOP values drop by approximately 20.4%, leading to a corresponding increase in statistical accuracy of the system. In Tokyo, the GDOP drop was 20.0%. Drops of approximately 20% can be found globally in the areas of coverage of the upcoming constellation. As DOP links the statistical accuracy of the solution with the position of the satellites in the sky, such a drop therefore indicates a much higher statistical certainty on the position fix obtained.

Practical work was attempted onboard a local ferry, *Red Jet 4*, but these experiments were not as successful due to limitations of the available equipment. Further practical trials will be necessary before the usefulness of a GNSS network can be ascertained for the purpose of monitoring ship structures.

The novel work conducted over the past three and a half years, particularly regarding the simulation of a receiver network onboard a vessel, has led to the belief that a GNSS-based ship structure monitoring system could eventually be developed. Several difficult questions remain to be answered, but it is hoped that disasters such as those that befell the *SS Edmund Fitzgerald* and the *MV Derbyshire* could eventually be prevented.

Appendix A

History of Navigation and Basics of the GPS

A.1 Introduction

This appendix contains a few sections of information that were originally included in Chapter 2, but removed for the final version of the thesis. Specifically, in this section can be found a brief overview of the history of navigation, from early days to modern systems and additional information regarding the GPS.

A.2 Brief History of Navigation

Ever since humans began to wander outside a small area, they have desired to know where they are in relation to their point of departure. Hence, navigation was born. Although this science, which many consider an art, has greatly evolved since its inception, the basic premises on which it was founded have not changed.

Clearly, land navigation was the first type of navigation developed. Available evidence has led historians to believe that early voyages were restricted to coastal or river areas, as such journeys were generally safer than overland travels [34]. Hence, it is probably accurate to conclude that recognition of landmarks was the primary method of orientation. Although there is some evidence that celestial navigation was used thousands of years ago for land navigation, it is probably not until the invention of the astrolabe or the magnetic compass that major improvements in the accuracy of land navigation were made.

Maritime navigation also had modest origins. Evidence suggests that the first maritime voyages consisted of hugging, i.e. closely following, the coastline [13].

Such voyages were likely to be hazardous as ancient mariners had no way of knowing, except from experience, about local conditions such as depth and tides. Depth sounding poles could have been used, but again, this entailed taking great risks. Major improvements in maritime navigation accuracy were made after the invention of the compass, sextant and the chronometer.

Aerial navigation is a more recent science. Due to the fact that modern aircraft were only invented a little over one hundred years ago, the first flights occurred after major developments in navigation had occurred. However, the particular conditions related to flight bring about sets of problems unseen on land or sea. These have required a great deal of innovation to solve.

The compass is the instrument that brought navigation out of the "dark ages". Different authors attribute the discovery of magnetism and the compass to different time periods between 2400 B.C. and 400 B.C., but most are in agreement that the Chinese were the first to notice the properties of lodestone, a magnetic material, which they used as a fortune-teller [13]. Eventually, it was realised that the property of magnetism could be used to indicate direction, and it is believed that before the end of the XIVth century, the use of the magnetic compass was starting to become widespread. Magnetic compasses were eventually replaced in the XXth century by gyroscopic compasses, which are by far more precise.

Although the compass was, and still is, an excellent instrument to discover orientation, it is impossible to use it exclusively to determine position. For this purpose, the astrolabe, the nocturnal, the cross-staff and the sextant were developed.

The astrolabe is a circular device used to calculate local solar time based on the elevation of stars, or the elevation of the sun at zenith [35]. The nocturnal is a similar device, however it is used for Pole Star observations [13]. These two devices, developed in the second century B.C. and the XVIIIth century respectively, allow for crude measurements of longitude.

The cross-staff, a device developed in the XVIth century, could be used by a single person to determine latitude by measuring the elevation of the sun, or another celestial body, and then using a series of tables [36]. Finally, an instrument that has not entirely disappeared today, the sextant, which replaced the cross-staff, is used to measure an angle between a plane and a celestial body, and hence determine latitude [29].

Although all of the above instruments can be considered great achievements, perhaps the greatest achievement in the history of navigation was the development of a precise chronometer by John Harrison in the middle of the XVIIIth century. Harrison's chronometers were able to keep time, while at sea, to a precision

of about three seconds a day, an unmatched achievement for the time, and one for which he eventually received the sum of approximately £20,000 from the British Board of Longitude in 1765 [13]. As this implies, this device was far more precise in the determination of longitude than either the astrolabe or the nocturnal. This desire to precisely determine time remains of great importance today as this information can be used to accurately determine one's position on the surface of the Earth.

Other navigational instruments or techniques have been developed over the course of centuries and researching them all would lend itself well to a full thesis. For the sake of completeness a few of them such as Davies' back staff, the Sumner line and the Mercantor projection, are mentioned here. The interested reader can find detailed information about these techniques or devices within the references cited in this section.

A.3 History of Satellite Navigation

This section is concerned with providing the reader a background into the development of satellite navigation and a few of the systems that preceded this "ultimate" navigational tool. It begins by providing a brief introduction to the Decca Navigator, the Long Range Navigation (LORAN) and Omega ground-based systems. This section then presents a brief history of the Navy Navigation Satellite System (NNSS), Navigation System with Timing And Ranging (NAVSTAR) GPS, the Global Navigation Satellite System (GLONASS) and the Galileo Satellite Navigation System, the latter hencforth referred to as Galileo.

The Decca Navigator was developed during World War II (WWII). It was a hyperbolic, ground-based navigation system usually consisting of four transmitter stations arranged in master-slave architectures. Each station would transmit on a different frequency, but each in phase with the master. At the receiver level, signal processing was utilised to bring the received signal from each station to the same frequency. This would allow the receiver to determine the phase difference between the signals received from the master and each slave. Using each pair of signals would allow determination of a possible position along a hyperbola having as foci the master station and the particular slave considered. This was repeated for each slave station, giving a potential position along three hyperbolae. The intersection of these hyperbolae gave the final position of the receiver. Range was the limiting factor for the Decca navigation system, and this was usually limited to 800km. The interested reader should refer to Chapter 3 of reference [54] for a

greater discussion of the technical aspects of the Decca Navigator. The last remaining Decca system stations were shut down in 2000.

The LORAN category of systems is another development of WWII. The original system was known as LORAN-A, but more recent versions are LORAN-C and LORAN-D, which have civilian and military applications respectively. The LORAN systems are also hyperbolic navigation systems, but operate in a somewhat different manner than Decca. To prevent ambiguity, the master LORAN station emits a pulse, which is received by both the receiver and the slave station. Upon receiving the pulse, the slave station emits its own pulse, which is also received by the receiver. Using the time difference between the reception of the first and second pulses allows for potential determination of position along a hyperbola having both LORAN stations as foci. Using a second pair of stations, another hyperbola is obtained, allowing for determination of the receiver using the intersection of the pair of hyperbolae obtained. The technical aspects of the LORAN system are discussed in detail in Chapter 4 of reference [54] and briefly in Chapter 3 of reference [39]. LORAN stations are still in operation in various regions around the globe.

The Omega system is also a hyperbolic navigation system, which was developed in the late 1940s. Like Decca, it uses phase difference techniques to determine position. However, unlike Decca it provided almost global coverage using eight Very Low Frequency (VLF) transmitters, which bounce signals off the ionosphere. Furthermore, only a single station is transmitting at any one time. This latter technique is known as time multiplexing, whereas the technique used by Decca is frequency multiplexing. Determination of position is made using the same technique as Decca. The Omega system was shutdown in 1997. The interested reader can find out more about this system by referring to Chapter 5 of reference [54]. A brief description of Omega can also be found in Chapter 3 of reference [39].

The NNSS, sometimes referred to as the Transit System, was the first space-based navigation system. Developed by the United States of America's Department of Defense (DOD), its history stems back to the launch of Sputnik I by the Union of Soviet Socialist Republics (USSR) in 1957. NNSS uses the same principle used to track Sputnik, the Doppler shift, to determine position. The first NNSS satellites were launched into a polar orbit in 1967 and the system remained in operation until 1996. For additional information on NNSS, the interested reader should refer to Chapter 6 of reference [54] and Chapter 3 of reference [39].

In order to improve on positioning accuracy, the DOD decided in 1973 to fund the GPS project. The first GPS satellites were launched in 1978 and the system became fully operational in 1993. Today, there are more than 30 active satellites

in orbit around the Earth which provide global coverage in order to determine a user's position [57], although the original system was designed to work with only 24 satellites. The operating principles behind GPS are presented in greater detail in Section 2.2.

GLONASS was the USSR's response to GPS. It also was supposed to consist of 24 satellites in orbit around the Earth in order to provide global positioning determination [26]. Not as popular as GPS, and probably not as well funded either, the GLONASS system had sunk into obscurity, and as of November 2004, only 10 satellites remained in orbit. Out of those, only 7 were operational [3]. However, as of October 2007, there were now 17 satellites in orbit, but of those, only 9 were usuable [6]. The Russian Space Agency's (RSA) update also showed that some satellites were launched in 2005 and 2006, indicating a renewal program was now in progress. The principles of operation of GLONASS are similar to those of GPS.

Galileo, will be the newest system to enter the foray of satellite navigation. Originally scheduled to be fully operation in 2008 [2], but now scheduled to become fully operational in 2012 due to a number of delays linked to project funding, Galileo will be the only SNS under full civilian control. The principles of operation of Galileo are also similar to those of GPS, however, Galileo will offer several services which are unavailable to users of GPS. More information about these services can be found in Section 3.7.3

A.4 Additional Information About the Operation of the NAVSTAR GPS

In this section, some of the information that was ommitted from Chapter 2 is included here for completeness. It begins with a basic mathematical explanation of the concept of Ground Coverage and finishes with an explanation of how the C/A code is used to determine a user's position.

A.4.1 Ground Coverage

Given the knowledge of an object's position in orbit, it is possible to calculate the ground coverage for any satellite. Although this concept is most critical in the case of communications missions, it also has great importance for GPS.

As will be seen in Section A.4.2, GPS requires a minimum of four satellites to be visible to the user in order to obtain a three-dimensional position. The term multiple coverage is used to refer to cases where more than one satellite is visible

whereas the term single coverage is used to refer to cases where only one satellite is visible.

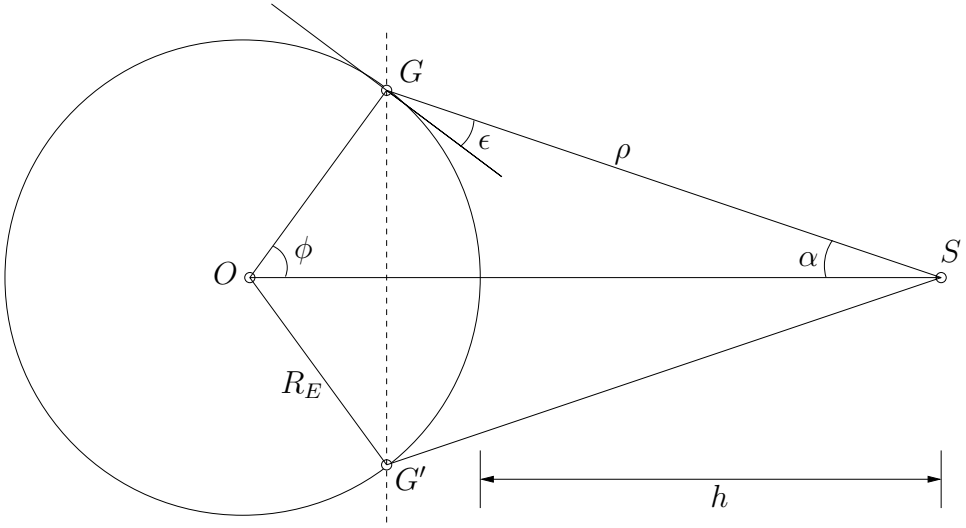

Figure A.1: Satellite ground coverage geometry

Consider Figure A.1. This figure can be used to approximate the ground coverage of any particular satellite in orbit. Assume that a satellite's antenna (or payload) can "see" objects in the conical section with angle 2α, and that the satellite is orbiting at an altitude of h above the surface of the Earth.

From this, figure it can be seen that:

$$\epsilon = \frac{\pi}{2} - \alpha - \phi \tag{A.1}$$

where ϕ is the geodetic semi-angle. Reference [52] defines ϕ as follows:

$$\phi = -\epsilon + \arccos\left(\frac{R_E}{R_E + h}\cos(\epsilon)\right) \tag{A.2}$$

where R_E is the radius of the Earth, and where ϕ is in radians. From simple trigonomotry, the diameter of coverage in 3D space, the distance GG', is:

$$\|GG'\| = 2R_E \sin(\phi) \tag{A.3}$$

Note that this defers from the distance that must be covered on the surface to travel from G to G'. This value would be:

$$D = 2R_E\phi \tag{A.4}$$

Finally, from this information, the slant range ρ, can be defined. Using the sine law:

$$\rho = \frac{(R_E + h)\sin(\phi)}{\sin\left(\frac{\pi}{2} + \epsilon\right)} \tag{A.5}$$

Applying the same analysis for every GPS satellite would allow for the determination of how many satellites are visible in any region of the world.

A.4.2 Theory Behind Using Satellites to Determine Location

Using satellites, it is theoretically possible to determine a user's exact location at any point on the surface of the Earth. However, much as the knowledge of time was critical in calculating longitude, the precise knowledge of time differences is crucial. To this end, the GPS satellites carry on board atomic clocks (Rubidium or Caesium), accurate to 10^{-9} seconds at the minimum. From elementary physics:

$$d = vt \tag{A.6}$$

where d is the total distance travelled, v the velocity and t the time of travel.

Hence the distance from any GPS satellite can be determined in the following manner:

$$d_{sat} = v(t_2 - t_1) = c(t_2 - t_1) \approx c_0(t_2 - t_1) \tag{A.7}$$

where t_2 is the time at which the signal is received from the satellite, t_1 the time at which the signal was sent from the satellite, c the speed of light and c_0 the speed of light in vacuum ($c_0 = 2.997\ 924\ 58 \times 10^8\ m/s$). Thus, $t_2 - t_1$ is the GPS signal's time of travel. In the following discussion, two critical assumptions will be made:

1. The signal's time of travel can be measured very accurately, and;
2. The position of the satellite(s) is(are) known at all times.

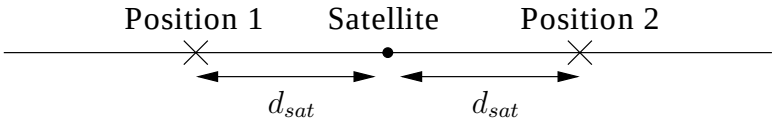

Figure A.2: GPS in one dimension with ambiguity on the user's position

Consider the one dimensional GPS example shown in Figure A.2. Here, one satellite is shown and the time of travel of the signal allows the distance to the satellite d_{sat} to be precisely determined. However, an ambiguity remains in this

case as the user can be at one of the two positions shown. There is no way to precisely determine at which position the user is located using a single satellite.

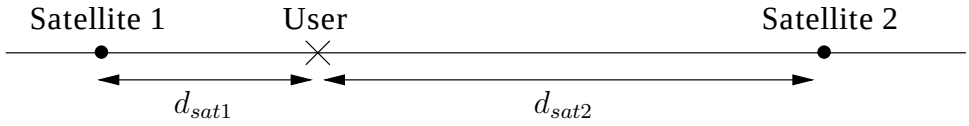

Figure A.3: GPS in one dimension with no ambiguity on the user's position

The solution to the problem is shown in Figure A.3. Here, utilising a second satellite leaves no ambiguity as there is only one point at which the user can be located which is at distance d_{sat1} from the first satellite, and at distance d_{sat2} from the second.

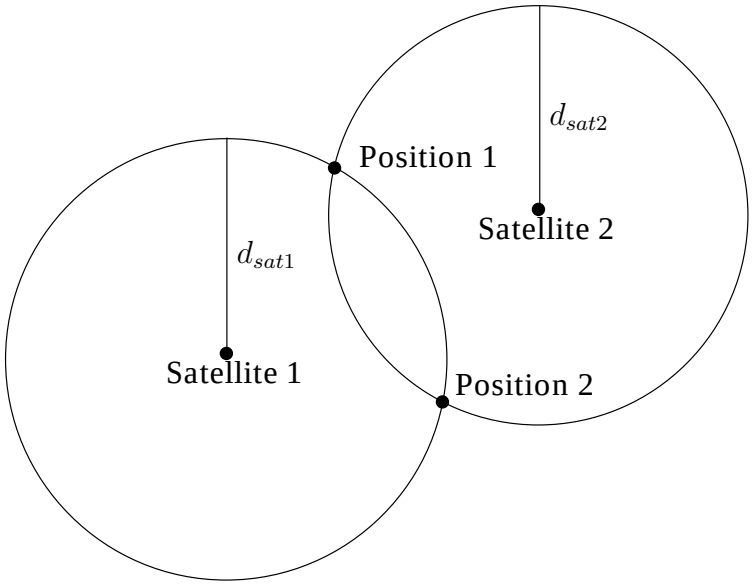

Figure A.4: GPS in two dimensions with ambiguity on the user's position

Consider now the example of GPS in two dimensions shown in Figure A.4. In this case, the user's distance from two satellites is known, but that is still not sufficient to obtain a definitive fix on the user's position. This is because in the general case depicted, the user can be at any of two positions where the circles of radii d_{satX} intersect. The solution to this ambiguity is analogous to the one in one dimension and is shown in Figure A.5.

The addition of a third satellite reading removes the ambiguity as there is only one point where all three circles intersect. Let us consider now the case in three dimensions shown in Figure A.6. As with all the one dimensional and two dimensional cases shown earlier, there are also two possible positions at which the user

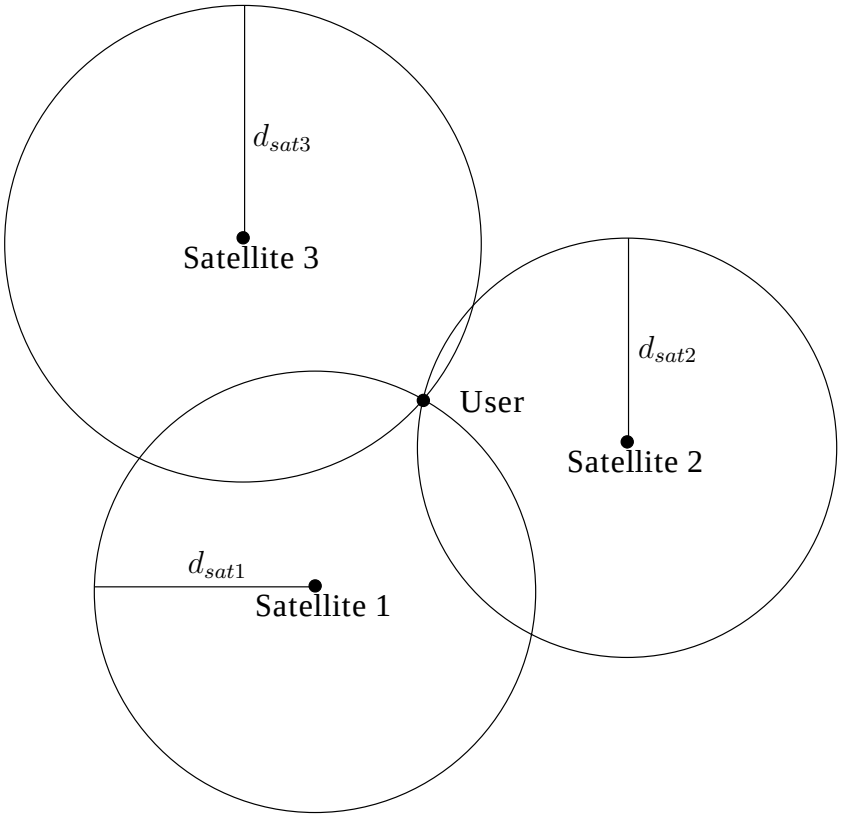

Figure A.5: GPS in two dimensions with no ambiguity on the user's position

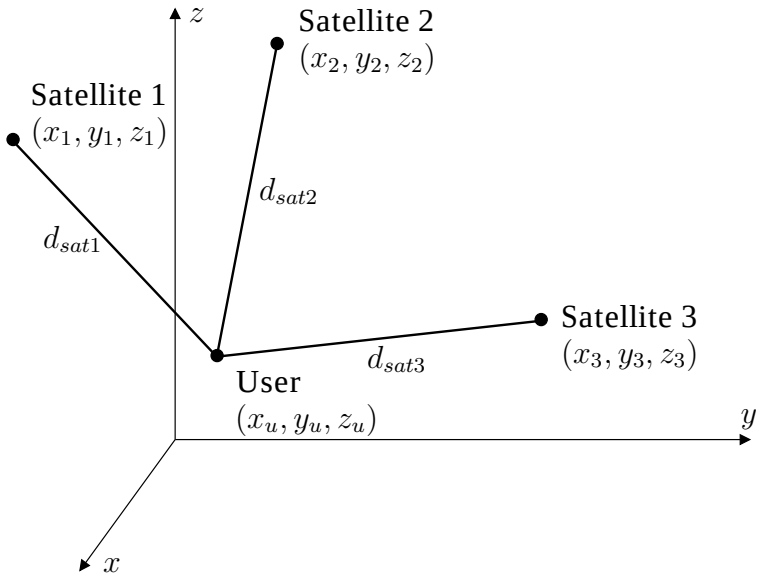

Figure A.6: Position of a user and three satellites in three dimensions

can be located if only three satellites are used to make a three dimensional position fix. However, it can be shown that one of the solutions is on the Earth's surface, while the other is located in space [57]. For most applications, it is obvious that the low-altitude solution is the correct one and thus a three dimensional position can be determined by iteratively solving for (x_u, y_u, z_u) the set of equations shown in (A.8).

$$\left.\begin{aligned} d_{sat1} &= \sqrt{(x_1 - x_u)^2 + (y_1 - y_u)^2 + (z_1 - z_u)^2} \\ d_{sat2} &= \sqrt{(x_2 - x_u)^2 + (y_2 - y_u)^2 + (z_2 - z_u)^2} \\ d_{sat3} &= \sqrt{(x_3 - x_u)^2 + (y_3 - y_u)^2 + (z_3 - z_u)^2} \end{aligned}\right\} \tag{A.8}$$

Up to this point, the entire discussion assumed that the signal's time of travel could be precisely determined and that the satellites positions are precisely known. In practice, the latter can be assumed to be true as the GPS satellites transmit their ephemeris coordinates (i.e. their position in the celestial sphere) in their signal allowing the receiver to determine their position in orbit [39]. Ground stations monitor the GPS satellites and send corrections to their ephemeris coordinates on a regular basis, thereby ensuring that the information they transmit remains correct.

On the other hand, it is not correct to assume that the signal's time of travel can be known with great precision. For this reason, the ranges between the receiver and the visible satellites are referred to as *pseudoranges*.

The GPS satellites are equipped with highly accurate atomic clocks whereas most GPS receivers are not, and are only equipped with crystal oscillator clocks. This is due to the fact that atomic clocks are bulky and quite expensive. This lack of a precise clock will introduce a timing error and thus offset the range the user measures to each satellite. This range offset is known as the *clock bias error*, which is denoted C_b. However, as the atomic clocks on board the satellites are synchronised, the bias error will be the same for every satellite as shown in Figure A.7.

In Figure A.7, the user is actually located at point U, but the receiver believes that the actual distance from any one satellite to the user is $(d_{satX} + C_b)$. Thus, unless modifications are made to the equations, there is no solution to the two-dimension system.

For the system to become solvable in three dimensions, another distance measurement must be taken, bringing the total number of measurements to four. This

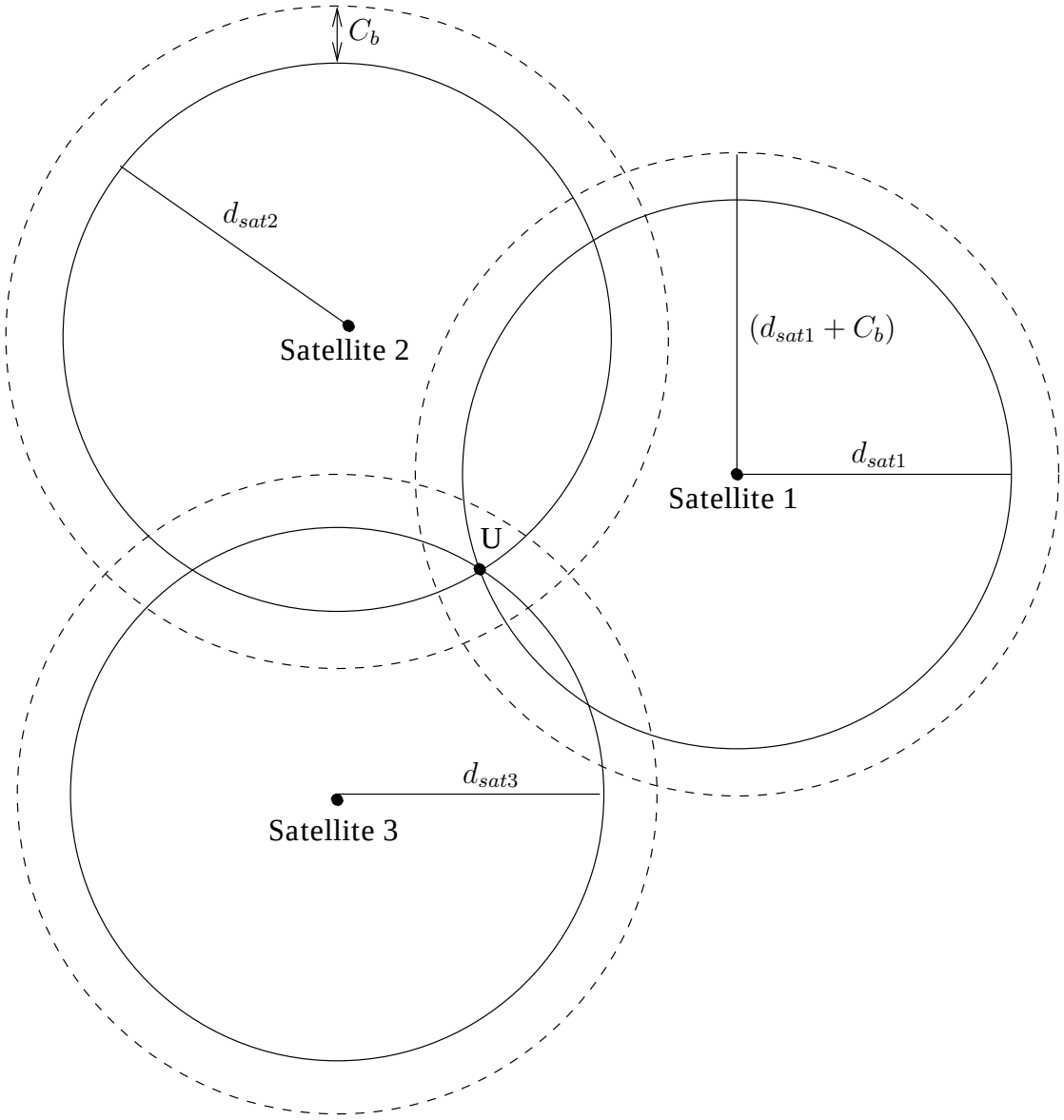

Figure A.7: Graphical representation of the clock bias error in two dimensions.

allows for the addition of the C_b variable to the system of (A.8) as shown below:

$$\left.\begin{aligned} d_{sat1} + C_b &= \sqrt{(x_1 - x_u)^2 + (y_1 - y_u)^2 + (z_1 - z_u)^2} \\ d_{sat2} + C_b &= \sqrt{(x_2 - x_u)^2 + (y_2 - y_u)^2 + (z_2 - z_u)^2} \\ d_{sat3} + C_b &= \sqrt{(x_3 - x_u)^2 + (y_3 - y_u)^2 + (z_3 - z_u)^2} \\ d_{sat4} + C_b &= \sqrt{(x_4 - x_u)^2 + (y_4 - y_u)^2 + (z_4 - z_u)^2} \end{aligned}\right\} \quad \text{(A.9)}$$

A solution can then be iteratively obtained for (x_u, y_u, z_u, C_b). This solution will still be slightly inaccurate for reasons such as atmospheric delays of the signal, inaccuracy of the clocks and inaccuracy of the ephemeris coordinates. However, it

will still be accurate to 50.25 metres (165 feet) 95% of the time [39].

A.4.3 Solving the System of (A.9) to Determine a User's Position

As mentioned in Section A.4.2, it is necessary to utilise an iterative approach to solve the system of (A.9). This is due to the fact that the system is a non-linear simultaneous system. Consider the range to a single satellite:

$$d_i = \sqrt{(x_i - x_u)^2 + (y_i - y_u)^2 + (z_i - z_u)^2} + C_b \tag{A.10}$$

where d_i is the distance to the i-th satellite, (x_i, y_i, z_i) the position of the satellite in 3D space, (x_u, y_u, z_u) the user's position in 3D space and C_b the clock bias.

To simplify the solution, it is possible to linearise the system of (A.9). To do so, it is first necessary to differentiate Equation (A.10). The following is then obtained:

$$\delta d_i = \frac{(x_i - x_u)\delta x_u + (y_i - y_u)\delta y_u + (z_i - z_u)\delta z_u}{\sqrt{(x_i - x_u)^2 + (y_i - y_u)^2 + (z_i - z_u)^2}} + \delta C_b \tag{A.11}$$

It is possible to rewrite Equation (A.11) as:

$$\delta d_i = \frac{(x_i - x_u)\delta x_u + (y_i - y_u)\delta y_u + (z_i - z_u)\delta z_u}{d_i - C_b} + \delta C_b \tag{A.12}$$

It is now possible to rewrite the system of (A.9) as a linearised system in the following form:

$$\begin{bmatrix} \delta d_1 \\ \delta d_2 \\ \delta d_3 \\ \delta d_4 \end{bmatrix} = \begin{bmatrix} \alpha_{1,1} & \alpha_{1,2} & \alpha_{1,3} & 1 \\ \alpha_{2,1} & \alpha_{2,2} & \alpha_{2,3} & 1 \\ \alpha_{3,1} & \alpha_{3,2} & \alpha_{3,3} & 1 \\ \alpha_{4,1} & \alpha_{4,2} & \alpha_{4,3} & 1 \end{bmatrix} \begin{bmatrix} \delta x_u \\ \delta y_u \\ \delta z_u \\ \delta C_b \end{bmatrix} \tag{A.13}$$

where

$$\alpha_{i,1} = \frac{x_i - x_u}{d_i - C_b} \qquad \alpha_{i,2} = \frac{y_i - y_u}{d_i - C_b} \qquad \alpha_{i,3} = \frac{z_i - z_u}{d_i - C_b} \tag{A.14}$$

Using simple matrix algebra, it is clear that the solution to the system shown in (A.13) is:

$$\begin{bmatrix} \delta x_u \\ \delta y_u \\ \delta z_u \\ \delta C_b \end{bmatrix} = \begin{bmatrix} \alpha_{1,1} & \alpha_{1,2} & \alpha_{1,3} & 1 \\ \alpha_{2,1} & \alpha_{2,2} & \alpha_{2,3} & 1 \\ \alpha_{3,1} & \alpha_{3,2} & \alpha_{3,3} & 1 \\ \alpha_{4,1} & \alpha_{4,2} & \alpha_{4,3} & 1 \end{bmatrix}^{-1} \begin{bmatrix} \delta d_1 \\ \delta d_2 \\ \delta d_3 \\ \delta d_4 \end{bmatrix} \tag{A.15}$$

However, the above is not the solution to the system shown in (A.9). To obtain

the solution to system (A.9), it is necessary to use an iterative algorithm, such as the following least-squares method which is described in Chapter 2 of Reference [57].

(i) Set the initial conditions $(x_{u_0}, y_{u_0}, z_{u_0}, C_{b_0})$. These can be any value the users wishes, but are usually set to zero for simplicity.

(ii) Calculate d_i for each satellite using the current values of (x_u, y_u, z_u, C_b).

(iii) Calculate $\alpha_{i,1}$, $\alpha_{i,2}$ and $\alpha_{i,3}$ using current values of d_i and (x_u, y_u, z_u, C_b).

(iv) Calculate δx_u, δy_u, δz_u and δC_b.

(v) Calculate δv.

(vi) If δv is smaller than a user-set threshold (the tolerance level), then the current values of (x_u, y_u, z_u, C_b) are returned. Otherwise proceed to the following steps:

  (a) Add the current values for $(\delta x_u, \delta y_u, \delta z_u, \delta C_b)$ to the initial conditions. This set of values referred to as $(x_{u_1}, y_{u_1}, z_{u_1}, C_{b_1})$ should be used as the new initial conditions.

  (b) Repeat the algorithm from step (i) until the value of δv reaches the specified tolerance level.

Note that in the above, the value of δv is:

$$\delta v = \sqrt{\delta x_u^2 + \delta y_u^2 + \delta z_u^2 + \delta C_b^2} \tag{A.16}$$

The inclusion of the term δC_b^2 is not necessarily required and it can be omitted if the user does not require that the tolerance level take into account the current value of the clock bias.

Appendix B

Anectodes and Stories from the Practical Work

Although completely unscientific, and not contributing anything novel to the field of research, I've decided to include a small section noting some of the anectodes that were picked up over the course of the practical experimentation.

B.1 The Accidently Illegal Rig

Early in the experimentation, on one of the first crossings during which data collection was being taken, the ship suddenly lost all GPS and radar functions. Additionally, the ship's AIS systems were disabled by the loss of the GPS, thus causing it to be illegally operating. Upon getting to port, I shut down the rig and changed the batteries, and the ship's GPS and radar systems returned to normal. But immediately upon my activating the rig again after leaving Southampton port, havoc returned. It was thus quickly established that my rig was the culprit and I had to manually shut it off.

To do that, I had to climb onto the bow of the ship while it was travelling in Southampton Water at about 35 knots, while being watched by some very shocked, or perhaps concerned, passengers as I wasn't harnassed in any way to the ship.

B.2 "What are those black boxes with wires?"

I was onboard *Red Jet 4* two days after they discovered the potential shrapnel car bombs in London in late June 2007. I had just set up the computer inside the passenger cabin and climbed up to the bridge when I was followed by a passenger

who asked the above question word for word.... The black boxes in question were the USB Radio-Modems which were connected to the Toshiba laptop and used to receive information from the rigs.

B.3 What to do in Rough Seas

On one of the days, crossings were extremely rough, and it was necessary to tie down the equipment. I did manage to impress the crews with my knowledge of some knots. On the same day I also managed to get thrown off my seat a number of times. Luckily, I managed to get a fair amount of data on this day.

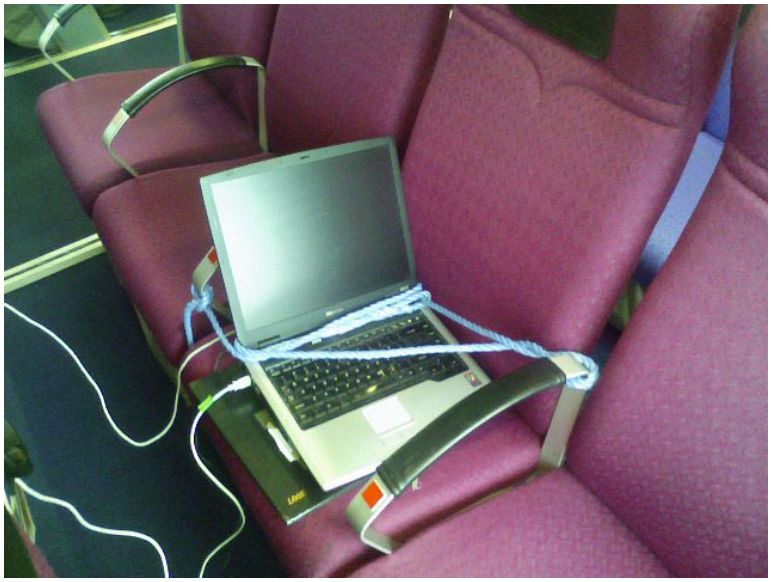

Figure B.1: How to tie a laptop to a ferry seat.

B.4 On Appreciation for Volunteers

Having spent a fair amount of time on the bridge of the craft, I've come to have an appreciation for the Coast Guard and the volunteers who work in SAR. On a quiet day, I would hear none, but on some other days, I heard several calls on the radio regarding lost vessels or people who had gone overboard.

B.5 Emergency Drills

On the first day I was to do data collection, the service had been suspended due to rough weather. Thus, the crews ran emergency drills and I was "volunteered" to be an additional passenger who was the crew's main helper. I was given the responsibility of helping a "drunken Lithuanian tourist" (one of the stewards, originally from Lithuania). About the only thing he would say is "beer". I managed to coax this incredibly good actor into putting on his life vest, but I had to promise to give him more alcohol once he got in the raft before he would cooperate.

B.6 The Dangerous Debris

Perhaps the oddest story I picked up while working onboard *Red Jet 4* was the fact that some seemingly harmless items can actually be quite dangerous to smaller vessels. A call on the radio from the port authorities indicated that a small house refrigerator had been spotted floating in the Solent. The call also indicated that only an inch or two of it was visible above the surface, making it extremely hazardous for smaller craft. As a result, I was drafted into the post of Watchman by the Captain and First Mate. We never saw the fridge, nor did any further calls about it come on the radio. Interestingly enough, the "main" concern of one steward was not the ability of the fridge to destroy the craft's engines, but rather its contents.

References

[1] Safer harbour operations with EGNOS. Online Publication. http://www.esa.int/esaNA/ESA8KS7708D_galileo_0.html.

[2] Galileo: The european programme for global navigation. European Space Agency Document, Netherlands, 2002.

[3] GLONASS history. Russian Federation Ministry of Defence Internet Status Update, November 2004. http://www.glonass-center.ru/hist_e.html.

[4] Galileo: The european programme for global navigation, 2nd edition. European Space Agency Document, Netherlands, 2005.

[5] QA1400 datasheet, August 2005. http://www.inertialsensor.com/qa1400.shtml.

[6] GLONASS constellation status. Russian Space Agency GLONASS Constellation Status, October 2007. http://www.glonass-ianc.rsa.ru/pls/htmldb/f?p=202:3:5815705317518805875::NO:::.

[7] GPS status. United States Naval Observatory, October 2007. ftp://tycho.usno.navy.mil/pub/gps/gpstd.txt.

[8] R. Ahmed, A.R.L. Tatnall, and S.P. Balaji. A comparison of spacecraft formation flying models used in real time hardware in the loop simulations. In *Proceedings of the 4th Workshop on Satellite Constellations and Formation Flying*, 2005.

[9] F.M. Bélanger and A.R.L. Tatnall. Monitoring of vessels using a GNSS receiver network. In *Proceedings of the 19th International Technical Meeting of the Satellite Division of The Institute of Navigation*, pages 1954–1964, 2006.

[10] F.M. Bélanger and A.R.L. Tatnall. An investigation of the flexible and rigid body response of a ship using a GNSS receiver network. In *Proceedings of*

the 20th International Technical Meeting of the Satellite Division of The Institute of Navigation, pages 1957–1963, 2007.

[11] J. Benedicto, S.E. Dinwiddy, G. Gatti, R. Lucas, and M. Lugert. Galileo: Satellite system design and technology developments. European Space Agency Document, Netherlands, 2000.

[12] R.D. Blevins. *Formulas for Natural Frequency and Mode Shape*. Robert E. Krieger Publishing Company, Malabar, 1984.

[13] W.J.V. Branch and E. Brook-Williams. *A Short History of Navigation*. Brown, Son & Ferguson, Ltd., Annapolis, 1942.

[14] J.R. Calvert and R.A. Farrar, editors. *An Engineering Data Book*. Calvert Technical Press, Southampton, 1998.

[15] Trimble Corporation. Trimble planning. Publicly available software. `http://www.trimble.com/planningsoftware.shtml`.

[16] L.W. Couch. *Digital and Analog Communication Systems*. Prentice Hall, fifth edition, 1997.

[17] R. DiEsposti, H. Bazak, and M. Whelan. WAAS geostationary communications segment (GCS) requirements analysis. In *PLANS - Position Location and Navigation Symposium 2002*, pages 283–290, 2002.

[18] K. Duff, M. Hyzak, and D. Tucker. Real-time deformation monitoring with GPS: Capabilities and limitations. *Proceedings of SPIE*, 3330:387–395, July 1998.

[19] K. Duff, M. Hyzak, and D. Tucker. Structural monitoring with GPS: Operational issues. *Proceedings of SPIE*, 3400:422–432, July 1998.

[20] J.A. Farrell, T.D. Givargis, and M.J. Barth. Real-time differential carrier phase GPS-aided INS. *IEEE Transactions on Control Systems Technology*, 8(4):709–721, July 2000.

[21] J. Guo, L. Xu, L. Dai, M. McDonald, J. Wu, and Y. Li. Application of the real-time kinematic global positioning system in bridge safety monitoring. *Journal of Bridge Engineering*, 10(2):163–168, March & April 2005.

[22] G.W. Hall. USCG differential GPS navigation service. Online Publication. `http://www.navcen.uscg.gov/pubs/dgps/dgpsdoc.pdf`.

[23] J.E. Heffernan and J.E. Tawn. An extreme value analysis for the investigation into the sinking of the m. v. derbyshire. *Journal of the Royal Statistical Society: Series C (Applied Statistics)*, 52(3):337–354, July 2003.

[24] J.E. Heffernan and J.E. Tawn. Extreme values in the dock. *Significance*, 1(1): 13–17, March 2004.

[25] S.E. Hirdaris, W.G. Price, and P. Temarel. Two and three-dimensional hydroelastic modelling of a bulker in regular waves. *Marine Structures*, 16(8): 627–658, November & December 2003.

[26] B. Hoffmann-Wellenhof, H. Lichtenegger, and J. Collins. *GPS: Theory and Practice*. Springer-Verlag, Wien, second edition, 1993.

[27] M. Hollreiser, P. Erhard, P. Lorenzi, and C.S. Dixon. Galileo user segment overview. In *16th International Technical Meeting of the Satellite Division of the United States Institute of Navigation*, pages 1914–1928, 2003.

[28] V.A. Hoyle, G. Lachapelle, M.E. Cannon, and C. Wang. Low-cost gps receivers and their feasibility for attitude determination. In *Proceedings of the 2002 National Technical Meeting of the Institute of Navigation*, pages 226–234, 2002.

[29] A.J. Hughes. *History of Air Navigation*. Unwin Brothers Limited, London, 1946.

[30] S.U Hwu, B.P. Lu, R.J. Panneton, and B.A. Bourgeois. Space station GPS antenna multipath analysis. In *IEEE Antennas and Propagation Society International Symposium 1995 Digest*, pages 662–665, 1995.

[31] Ashtech Incorporated. G12 OEM board and sensor reference manual, January 1997. United States of America.

[32] K. Kageyama, I. Kimpara, T. Suzuki, I. Ohsawa, H. Muyarama, and K. Ito. Smart marine structures: an approach to the monitoring of ship structures with fibre-optic sensors. *Smart Materials and Structures*, 7(4):472–478, August 1998.

[33] Z. Kang, B. Tapley, S. Bettadpur, J. Ries, P. Nagel, and R. Pastor. Precise orbit determination for the GRACE mission using only GPS data. *Journal of Geodesy*, 80(6):322–331, September 2006.

[34] M. Kayton. *Navigation: Land, Sea, Air & Space*, chapter Introduction to Land Navigation, pages 65–72. IEEE Press, New York, 1990.

[35] M. Kayton. *Navigation: Land, Sea, Air & Space*, chapter Introduction to Cartography, pages 5–14. IEEE Press, New York, 1990.

[36] M. Kayton. *Navigation: Land, Sea, Air & Space*, chapter Introduction to Ship Navigation, pages 147–160. IEEE Press, New York, 1990.

[37] I. Lee, M. Kim, and A.R. Robinson. Determination of the natural frequencies and mode shapes for large structures by accelerated newton-raphson method. *Computers and Structures*, 63(1):61–68, 1997.

[38] A. Leick. *GPS Surveying 3rd Edition*. John Wiley & Sons Ltd., New York, 2004.

[39] T. Logsdon. *The NAVSTAR Global Positioning System*. Van Nostrand Reinhold, New York, 1992.

[40] J.W. Lovse, W.F. Teskey, G. Lachapelle, and M.E. Cannon. Dynamic deformation monitoring of tall structure using GPS technology. *Journal of Surveying Engineering*, 121(1):35–40, February 1995.

[41] North West Bay Ships PTY Ltd. Red funnel 39m catamaran ferry general arrangement revision r. Technical Drawings, October 2002. Australia.

[42] J. Lygeros and N. Lynch. On the formal verification of the TCAS conflict resolution algorithms. In *Proceedings of the 36th IEEE Conference on Decision and Control*, pages 1829–1834, 1997.

[43] O. Montenbruck, T. Ebinuma, E.G. Lightsey, and S. Leung. A real-time kinematic GPS sensor for spacecraft relative navigation. *Aerospace Science and Technology*, 6(6):435–449, October 2002.

[44] S. Nakamura. GPS measurement of wind-induced suspension bridge girder displacement. *Journal of Structural Engineering*, 126(12):1413–1419, December 2000.

[45] A.V. Oppenheim, A.S. Willsky, S. Hamid, and S.H. Nawab. *Signals and Systems*. Prentice-Hall, New York, 2nd edition, 1996.

[46] M.G. Petovello, K. O'Keefe, G. Lachapelle, and M.E. Cannon. Field results of a GPS/INS-based approach to measuring ship flexure onboard an aircraft carrier. In *Proceedings of the 18th International Technical Meeting of the Satellite Division of The Institute of Navigation*, pages 2039–2048, 2005.

[47] J.G. Proakis and D.K. Manolakis. *Digital Signal Processing: Principles, Algorithms and Applications*. Prentice-Hall, New York, 3rd edition, 1996.

[48] J.G. Proakis and M. Salehi. *Communications System Engineering*. Prentice-Hall, New York, 2nd edition, 2001.

[49] T.S. Rappaport. *Wireless Communications: Principles and Practice*. Prentice Hall PTR, 1999.

[50] G.W. Roberts, X. Meng, and A.H. Dodson. Integrating a global positioning system and accelerometers to monitor the deflection of bridges. *Journal of Surveying Engineering*, 130(2):65–72, May 2004.

[51] C. Guedes Soares and S. Dias. Probabilistic models of still-water load effects in containers. *Marine Structures*, 9(3-4):287–312, 1996.

[52] J.P.W. Stark and G.G. Swinerd. *Spacecraft Systems Engineering*, chapter Mission Analysis, pages 111–167. John Wiley & Sons Ltd., Chichester, third edition, 2003.

[53] B.D. Tapley, S. Bettadpur, M. Watkins, and C. Reigber. The gravity recovery and climate experiment: Mission overview and early results. *Geophysical Research Letters*, 31(9):1–4, May 2004.

[54] L. Tetley and D. Calcutt. *Electronic Aids to Navigation*. Edward Arnold Ltd., London, 1986.

[55] F. Toran-Marti and J. Ventura-Traveset. The ESA EGNOS project: The first step of the european contribution to the global navigation satellite system (GNSS). In *NAVIGARE Conference 2004*, 2004.

[56] National Transport and Safety Board. Marine Accident Report *SS Edmund Fitzgerald* Sinking in Lake Superior on November 10, 1975. Report Number: NTSB-MAR-78-3, May 1978. `http://www.uscg.mil/history/webshipwrecks/edmundfitzgeraldntsbreport.html`.

[57] J.B.-Y. Tsui. *Fundamentals of Global Positioning System Receivers: A Software Approach*. John Wiley & Sons Ltd., New York, 2000.

[58] G. Wang, K. Pran, G. Sagvolden, G.B. Havsgård, A.E. Jensen, G.A. Johnson, and S.T. Vohra. Ship hull structure monitoring using fibre optic sensors. *Smart Materials and Structures*, 10(3):472–478, June 2001.

[59] F. Wu, N. Kubo, and A. Yasuda. Precise positioning using modernized GPS and galileo in asia. In *Proceedings of Asia Navigation Conference 2003*, September 2003.

[60] S. Yoon and J.B. Lundberg. An integer ambiguity resolution algorithm for real-time GPS attitude determination. *Applied Mathematics and Computation*, 129(1):21–41, June 2002.

[61] J. Zhu. Calculation of geometric dilution of precision. *IEEE Transactions on Aerospace and Electronic Systems*, 28(3):893–895, July 1992.